The important thing is not to stop questioning.
Curiosity has its own reason for existing.

Albert Einstein

Abstract (English)

The development of engineered muscle constructs for regenerative medicine and *in-vitro* models for pharmacological testing and musculoskeletal disease research has received significant attention in recent years. Achieving these goals requires replicating the 3D structure of muscle tissue and applying external stimuli to enhance muscle cell differentiation facing the challenges presented by the complexity of muscle tissue *in-vivo*. While Bioprinting (BioP) shows promise in producing 3D tissue structures, there is a lack of research on the mechanical stimulation of these 3D bioprinted constructs. Novel approaches are required to address this knowledge gap, including 1) applying mechanical stimulation to the 3D bioprinted construct and 2) integrating the BioP phase into the stimulation device.
For this reason, the present work proposes the design, manufacturing, and benchmarking of a BioP-integrated mechanical platform that can mechanically stimulate a 3D muscle model directly printed within the bioreactor.
The study involves three primary phases.

The first phase includes the design and development of elastic supports suitable for BioP and long-term cell culture. To this end, two different manufacturing strategies were investigated: i) 3D co-printing of polycaprolactone (PCL) supports on which the hydrogel is deposited and ii) molding technique of polydimethylsiloxane (PDMS) supports on which the hydrogel is bioprinted. Regarding co-printing, the biological effect of the technique was first evaluated and subsequently the effect of the substrate geometry on cell differentiation was analyzed. To this end, three different geometries - linear, circular, and hybrid (linear and circular features combined) - were co-printed and compared. All structures exhibit optimal cell viability (>94%), but the linear pattern highlighted the best level of *in-vitro* cell differentiation, in particular after 14 days of culture. However, PCL supports were particu-

larly stiff for cyclic traction mechanical stimulation. Therefore, starting from these results, other linear supports were created using PDMS and the second proposed manufacturing technology which allowed to obtain structures with greater elasticity. The elasticity of the PDMS and supports has been demonstrated performing experimental mechanical tensile tests. Experimental results showed that to generate a support elongation of 4 mm the force to be applied is approximately 1.68 ± 0.36 N. Furthermore, the experimental data allowed the extraction of the specific material constitutive parameters used in the next step as material properties in the numerical model.

In the second phase, numerical tools will be used to design a Smart Petri Dish (SPD) containing the stimulation mechanism as well as the final cyclic mechanical platform. To this end, as a starting numerical model, the tensile test of the extensible supports was numerically simulated and calibrated using the experimentally extracted material parameters. The comparison between the results of the *in-silico* study with the experimental ones showed a good correspondence, in particular in the case of the Ogden constitutive model (1.71 vs. 1.68 ± 0.36 N).
After this calibration phase, two SPD configurations capable of stimulating at least three cellular supports simultaneously in a high-throughput manner have been numerically studied. Specifically, their behavior during the application of stimulation and the homogeneous transmission of traction to all constructs was evaluated. In order to validate the numerical results, the two SPD configurations were 3D printed and the experimentally observed behavior confirmed the results of the *in-silico* study.

Finally, the third phase of the study will involve the *in-vitro* validation of the proposed platform in terms of transmission of the mechanical stimulation to the 3D construct, integration of the BioP step, and the biological effect of dynamic culture on muscle cells. Due to the different nature, hydrophobic and hydrophilic respectively, of the PDMS, supports manufacturing material, and of the hydrogel deposited on top of them, their interaction, i.e., the transmission of stimulation to the hydrogel, was studied. The results demonstrated that soft-textured hydrogels are able to stretch coherently with the underlying support (strain ε [%]: CELLINK START 23.43 ± 3.72, chemically cross-linked hydrogel 18.72 ± 6.42, cross-linked alginate with calcium chloride diluted (1:2) 19.39 ± 3.36) while stiff hydrogels such as purely cross-linked alginate are unable to interact and therefore stretch (strain ε [%]: 5.29 ± 3.36). This trend does not occur in the case of compression stimulation, where even totally cross-linked alginate is capable of deforming. The *in-silico* study confirmed the experimental trend (strain ε [%] with tie condition

20.95 and non-tie condition 2.11). Furthermore, *in-vitro* biological characterization was performed to investigate the myogenic induction potential of the dynamic culture on the 3D bioprinted constructs. For this purpose, the bioprinted samples were cyclically stimulated (12%, 1 Hz, 15 minutes stretch + 15 minutes rest, for 5 hours per day for 2 days). The results highlighted excellent viability (approximately equal to 90% for all time points) and demonstrated that the application of the external stimulus markedly influences the gene expression of murine myoblasts already after 7 days of culture. Furthermore, sterility is very important for a product intended for future applications related to the development of preclinical platforms for drug screening and disease modeling. To this end, it was demonstrated that the developed technological process can be performed under sterile conditions.

In conclusion, prototypes are now available of a cutting-edge mechanical platform that integrates the 3D BioP phase and is capable of stimulating 3D biological constructs for applications in the field of muscle tissue engineering.

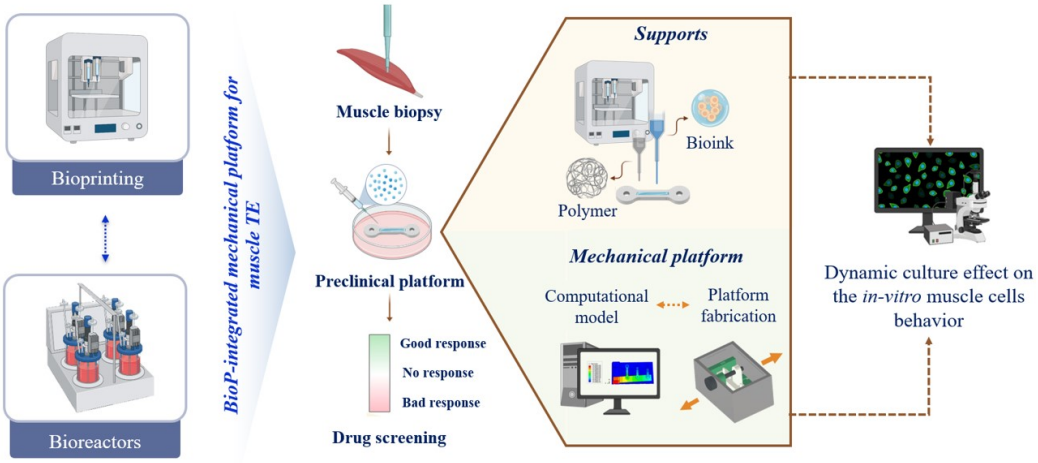

Figure 1: Graphical abstract of PhD project presented in this thesis. Design, manufacturing, and benchmarking of 3D BioP integrated-mechanical platform for promoting muscle regeneration for future preclinical applications in drug screening and/or disease modeling.

Abstract (Italian)

Lo sviluppo di costrutti muscolari ingegnerizzati per la medicina rigenerativa e modelli *in-vitro* per test farmacologici e ricerca sulle malattie muscoloscheletriche ha ricevuto notevole attenzione negli ultimi anni. Per raggiungere questi obiettivi è necessario replicare la struttura 3D del tessuto muscolare e applicare stimoli esterni per migliorare il differenziamento delle cellule muscolari affrontando le sfide presentate dalla complessità del tessuto muscolare *in-vivo*. In questo scenario, la biostampa rappresenta una tecnica promettente per la produzione di strutture tissutali 3D; tuttavia, la stimolazione meccanica di questi costrutti biostampati risulta scarsamente studiata. Per colmare questa lacuna, sono necessari nuovi approcci, come 1) stimolare meccanicamente il costrutto 3D biostampato e 2) integrare la fase BioP nel dispositivo di stimolazione.
Per questo motivo, il presente lavoro propone la progettazione, la produzione e la validazione di una piattaforma meccanica con biostampa integrata in grado di stimolare meccanicamente un modello muscolare 3D stampato direttamente all'interno del bioreattore.
Lo studio comprende tre fasi principali.

La prima fase prevede la progettazione e lo sviluppo di supporti elastici adatti alla biostampa e alla coltura cellulare a lungo termine. A tal fine, due diverse strategie di manifattura sono state investigate: i) co-stampa 3D di supporti in policaprolattone (PCL) su cui è depositato l'idrogel e ii) tecnica di stampaggio di supporti in polidimetilsilossano (PDMS) su cui è biostampato l'idrogel. Per quanto riguarda la co-stampa, è stato innanzitutto valutato l'effetto biologico della tecnica e successivamente è stato analizzato l'effetto della geometria del substrato sul differenziamento delle cellule. A tal fine, tre diverse geometrie - lineare, circolare e ibrida (caratteristiche lineari e circolari combinate) - sono state co-stampate e confrontate. Tutte le strutture

hanno mostrato una vitalità cellulare ottimale (>94%), ma il modello lineare ha evidenziato il miglior livello di differenziamento cellulare *in-vitro*, in particolare dopo 14 giorni di coltura. Tuttavia, i supporti in PCL risultavano particolarmente rigidi per la stimolazione meccanica a trazione ciclica. Pertanto, partendo da questi risultati, sono stati realizzati altri supporti lineari utilizzando il PDMS e la seconda tecnologia di fabbricazione proposta che ha permesso di ottenere strutture con maggiore elasticità. L'elasticità dei supporti è stata dimostrata eseguendo prove sperimentali di trazione meccanica. I risultati sperimentali hanno mostrato che per generare un allungamento di 4 mm la forza da applicare è di circa 1.68 ± 0.36 N. Inoltre, i dati sperimentali hanno consentito l'estrazione degli specifici parametri costitutivi del materiale utilizzati nella fase successiva come proprietà del materiale nel modello numerico.

Nella seconda fase, sono stati utilizzati strumenti numerici per progettare e sviluppare una *Smart Petri Dish* (SPD) contenente il meccanismo di stimolazione e la piattaforma meccanica ciclica finale. A tal fine, come modello numerico di partenza, è stata simulata numericamente e calibrata la prova di trazione dei supporti estensibili utilizzando i parametri del materiale estratti sperimentalmente. Il confronto tra i risultati dello studio *in-silico* con quelli sperimentali ha mostrato una buona corrispondenza, in particolare nel caso del modello costitutivo di Ogden (1.71 N contro 1.68 ± 0.36 N).
Dopo questa fase di calibrazione, sono state studiate numericamente due configurazioni di SPD in grado di stimolare almeno tre supporti cellulari contemporaneamente in modo *high-throughput*. Nello specifico è stato valutato il comportamento della SPD durante l'applicazione della stimolazione e la trasmissione omogenea della trazione a tutti i costrutti. Per convalidare i risultati numerici, le due configurazioni di SPD sono state stampate in 3D e il comportamento osservato sperimentalmente ha confermato i risultati dello studio *in-silico*.

Infine, la terza fase del lavoro ha riguardato la validazione *in-vitro* della piattaforma proposta in termini di trasmissione della stimolazione meccanica al costrutto 3D, integrazione della fase BioP ed effetto biologico della coltura dinamica sulle cellule muscolari. A causa della diversa natura, rispettivamente idrofobica e idrofila, del PDMS, materiale di fabbricazione dei supporti, e dell'idrogel depositato sopra di essi, è stata studiata la loro interazione e la trasmissione della stimolazione all'idrogel. I risultati hanno dimostrato che gli idrogel a consistenza morbida sono in grado di allungarsi in modo coerente con il supporto sottostante (deformazione ε [%]: CELLINK START 23.43 ± 3.72, idrogel cross-linkato chimicamente 18.72 ± 6.42, algi-

nato cross-linkato con calcio cloruro diluito (1:2) 19.39 ± 3.36) mentre gli idrogel rigidi come l'alginato puramente reticolato non sono in grado di interagire e quindi allungarsi (deformazione ε [%]: 5.29 ± 3.36). Questa tendenza non si osserva nel caso della stimolazione a compressione, dove anche l'alginato totalmente reticolato è in grado di deformarsi. Lo studio *in-silico* ha confermato la tendenza sperimentale (deformazione ε [%] con condizione tie 20.95 e non tie 2.11). Inoltre, è stata eseguita la caratterizzazione biologica *in-vitro* per studiare il potenziale di induzione miogenica della coltura dinamica sui costrutti biostampati in 3D. A tale scopo, i campioni biostampati sono stati stimolati ciclicamente (12%, 1 Hz, 15 minuti di allungamento + 15 minuti di riposo, per 5 ore al giorno per 2 giorni). I risultati hanno evidenziato un'ottima vitalità (circa pari al 90% per tutti i time point) e hanno dimostrato che l'applicazione dello stimolo esterno influenza marcatamente l'espressione genica dei mioblasti murini già dopo 7 giorni di coltura. Inoltre, la sterilità è molto importante per un prodotto destinato a future applicazioni legate allo sviluppo di piattaforme precliniche per lo screening dei farmaci e la modellizzazione delle malattie. A tal fine, è stato dimostrato che il processo tecnologico sviluppato puó essere eseguito in condizioni sterili.

In conclusione, sono ora disponibili i prototipi di una piattaforma meccanica all'avanguardia che integra la fase di biostampa 3D ed è in grado di stimolare costrutti biologici 3D per applicazioni nel campo dell'ingegneria dei tessuti muscolari.

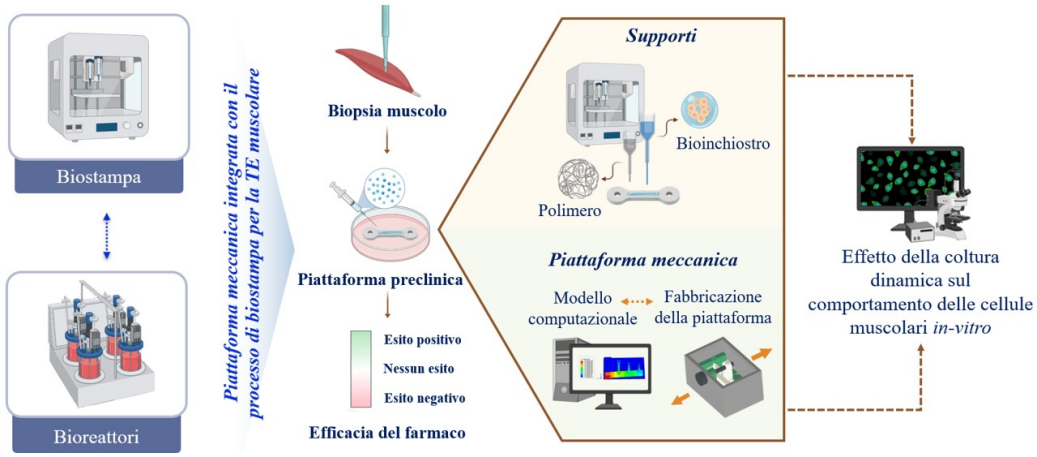

Figure 2: Abstract grafico del progetto di dottorato presentato in questa tesi. Progettazione, fabbricazione e validazione di una piattaforma meccanica integrante il processo di biostampa 3D per promuovere la rigenerazione muscolare per future applicazioni precliniche nello screening farmacologico e/o nella modellizzazione delle malattie.

List of Abbreviations

AM Additive Manufacturing

BioP Bioprinting

BNCT Boron Neutron Capture Therapy

3D Three-dimensional

CAD Computer-Aided Design

CAE Computer-Aided Engineering

cDNA complementary DNA

CFD Computational Fluid Dynamics

CH Chitosan

DAPI 40,6-diamidino-2-phenylindole

DBB Droplet-Based Bioprinting

DLP Digital Light Processing

DMEM Dulbecco's Modified Eagle medium

DOD Drop-On-Demand

EBB Extrusion-Based Bioprinting

ECM ExtraCellular Matrix

EthD-1 Ethidium homodimer

FBS Fetal Bovine Serum

FEA Finite Element Analysis

FEM Finite Element Method

GE Gelatin

GelMA Gelatin methacryloyl

HEPA High-Efficiency Particulate Air

LAB Laser-Assisted Bioprinting

LIFT Laser Induced Forward Transfer

MSC Mesenchymal Stem Cell

NFC Nano-Fibrillated Cellulose

OD Outer Diameter

K Stiffness

PBS Phosphate Buffered Saline

PCL Polycaprolactone

PDMS Polydimethylsiloxane

PEMF Pulsed Electro-Magnetic Field

PGK PhosphoGlycerate Kinase

PH PrintHead

PI Photoinitiator

RT Room Temperature

RT-qPCR Real-Time quantitative Polymerase Chain Reaction

SA Sodium Alginate

SLA Stereolithography

SMC Smooth Muscle Cell

SPD Smart Petri Dish

SS Shear Stress

Star-PEG-MA Star-PEG maleimide groups-functionalized

TE Tissue Engineering

TPP Two Photon Stereolithography

VT Vat Photopolymerization

Contents

List of Figures

List of Tables

Chapter 1

Introduction

The development of engineered muscle constructs for regenerative medicine and *in-vitro* models for pharmacological testing and musculoskeletal disease research has received significant attention in recent years [1]. Achieving these goals requires replicating the 3D structure of muscle tissue [2] and applying external stimuli to enhance muscle cell differentiation [3, 4]. This approach addresses the challenges presented by the complexity of muscle tissue *in-vivo*. In this scenario, Bioprinting (BioP) holds great promise for the production of 3D tissue constructs [5, 6]; however, there is a lack of research on the mechanical stimulation of these 3D bioprinted constructs [7]. To address this gap in knowledge, novel approaches are needed, such as 1) mechanically stimulating the 3D bioprinted construct and 2) integrating the BioP phase into the stimulation device.
For this reason, the present work proposes the design, manufacturing, and benchmarking of a BioP-integrated mechanical platform to mechanically stimulate a 3D muscle model directly printed into the bioreactor. Furthermore, as the design phase of the mechanical platform requires the definition of a large number of process variables, supporting engineering tools such as numerical models have been exploited, limiting experimental tests that require time and economic resources.

This chapter provides a general overview of 3D BioP, mechanical bioreactors and their development process divided into design, fabrication, and validation. Furthermore, the use of numerical models to support the bioreactor design phase and the innovative approach of combining BioP and dynamic culture will be presented. Finally, the aim and organization of the thesis are illustrated.

1.1 Bioprinting

3D BioP is a booming additive manufacturing (AM) method and it is defined as "*the use of computer-aided transfer processes for patterning and assembling living and non-living materials with a prescribed 2D or 3D organization in order to produce bioengineered structures serving in regenerative medicine, pharmacokinetic and basic cell biology studies*" [8].

The BioP process involves the use of a living material, usually cells (from patient biopsy or immortalized cell lines), and/or other biological molecules (e.g., growth factors, genes, and proteins) which are incorporated into a non-living biomaterial. The biomaterials typically used for BioP are the hydrogels thanks to their ability to mimic extracellular matrix (ECM) components and to allow cellular encapsulation in a highly hydrated and mechanically supporting 3D environment [9]. The combination of biological components and hydrogel is defined as bioink [10]. Once formulated and prepared, the bioink is printed layer-by-layer using a bioprinter until the three-dimensional construct is created. Subsequently, the fabricated scaffold is cross-linked to ensure structural stability and biological efficacy. Finally, the construct is placed in the incubator and during the days of culture the cells within the structure proliferate, differentiate, and form the new tissue.

In the BioP process, three main steps can be recognized [11, 12] (Figure 1.1).

1. Pre-printing, with the development and characterization of the bioink.
2. 3D Bioprinting, where the bioink is extruded and the 3D construct is fabricated.
3. Post-printing, with the cross-linking and incubation of the 3D construct.

To increase the success of the third step, the aid of bioreactors that improve and speed up the tissue maturation process is crucial.
A multitude of BioP technologies have been developed and they can be divided into 3 macro groups: extrusion-based bioprinting (EBB), droplet-based bioprinting (DBB), and light-assisted bioprinting (LAB). Furthermore, several approaches have been recently presented in the literature, including *in-situ* BioP.
BioP technologies and approaches are described in detail in the following sections 1.1.1 and 1.1.2.

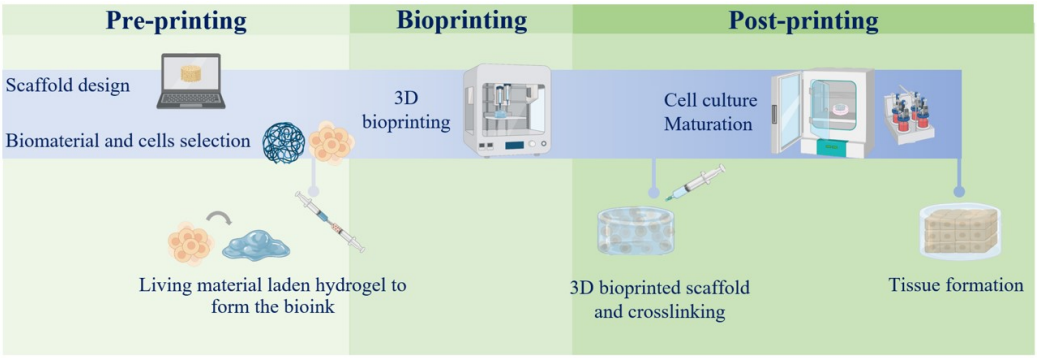

Figure 1.1: 3D BioP process. The process can be divided into three steps: pre-printing, printing, and post-printing. The pre-printing step involves the incorporation of biological components (e.g., cells, growth factors) into a hydrogel to form the bioink. Then, the 3D structure is printed and finally, in the post-printing phase, the scaffold is cross-linked to ensure structural stability and biological efficacy. Finally, the construct is incubated and the cells (within the scaffold) proliferate and differentiate leading to the formation of new tissue. The effectiveness of the third phase is improved thanks to the use of bioreactors developed to promote tissue maturation and cellular nutrition.

1.1.1 BioP technologies

The BioP technologies that enable the processing of a bioink can be classified into three major categories: EBB, DBB, and LAB (Figure 1.2). These techniques vary in precision and accuracy in the material deposition and cell survival [13].

Extrusion-based bioprinting

EBB is the most commonly used BioP technology due to its affordability and practicability [14]. In EBB, the biomaterial is contained in a syringe and extruded onto the printing plate by applying a pneumatic pressure or a mechanical force (i.e., piston- or screw-based extrusion). The extrusion mechanism can move in a 3D coordinate system that allows a precise and repeatable layer-by-layer deposition [15]. The advantage of pneumatic pressure-based extrusion is the simple and compact drive mechanism. Instead, mechanical extrusion systems have the advantage to provide more direct control over the material flow and extrude a wider range of viscous materials (viscosity from 10^{-3} up to 10^{4} Pa s) [16]. Furthermore, EBB can deposit bioinks with high

cell densities (typically less than 10^7 cells/mL to avoid altering the bioink rheology), which allows the creation of biologically relevant constructs in an acceptable time [17].
On the other hand, the main limitations of EBB technologies are: i) the risk of nozzle clogging with high viscosity materials; ii) reduced resolution; iii) difficulties in creating high complex structures [18]. Furthermore, when working with cell-laden biomaterials, cell viability after EBB is lower than other BioP technologies (in the range of 40% - 86% with a decrease in viability related to a decrease in nozzle diameter and an increase in extrusion pressure [19]). However, although cell viability can be increased by choosing a larger nozzle or decreasing the extrusion pressure, this can result in a loss of resolution and printing speed [16].

In this work the discussion will focus on EBB which is the technology used to realize this project.

Droplet-based bioprinting

DBB consists in precisely depositing droplets with a controlled volume on a printing plate. DBB techniques are classified in inkjet BioP, acoustic BioP, and valve-jet BioP [20].

Inkjet-based BioP

Inkjet BioP is the most popular technique in DBB and it is classified into thermal and piezoelectric drop-on-demand (DOD) inkjet. These two approaches share the same principle, i.e., the formation of droplets that lay down through a nozzle, however they present different mechanisms of drop formation.
Thermal DOD is based on a heating element used to heat the aqueous ink (to around 200-300 °C for a very short period of time, in the order of ms) and form bubbles within the liquid material. The pressure generated by the bubbles pushes the ink through the nozzle, therefore a droplet is formed and lays down on the printing plate. On the other hand, in piezoelectric DOD, a shockwave is generated by a piezoelectric crystal which changes its shape when a voltage is applied. As a consequence, the generated shockwave produces the droplet that is ejected through the nozzle.
Thermal DOD printers are generally cheaper compared to the piezoelectric ones. However, the piezoelectric approach can deposit a wider range of materials and is generally chosen for commercial bioprinters [21, 22].
DOD technologies are widely used in BioP due to their low cost and wide

availability of machines. In addition, DOD technologies allow the simultaneous printing of different biological materials and cells by using multiple cartridges and nozzles. The advantages of inkjet BioP compared to EBB are the high printing speeds, high-precision positioning, and high resolution controlled by the final droplet diameter, which has a typical volume in the range of 10-100 pL [23]. For this reason, adding a second cross-linking step is often necessary to increase the stability with the risk of impacting on cell viability [20].
However, inkjet also has several disadvantages. The main disadvantages are the restrictions for the bioinks that should be liquid and have a low viscosity to enable droplet formation and prevent nozzle clogging.
Consequently, to create 3D structures with inkjet BioP, it is necessary to introduce a second crosslinking step to increase the structure's mechanical stability [24] with the risk of increasing the structure fabrication time and impacting cell viability [25]. Furthermore, inkjet bioprinting can suffer from satellite droplet formation, i.e. small secondary droplets that can form next to the larger primary ones reducing the overall accuracy and resolution [26].
Both inkjet technologies enable the printing of cells and biomolecules [27–29] with a higher viability than microextrusion, reaching over 95% for piezoelectric DOD and 90% for thermal DOD [30, 31]. However, despite the high viability, there is a risk of nozzle clogging in the case of high cell concentration. This, combined with the small deposited volume, makes it difficult to achieve biologically relevant cell densities in the printed structure.

Acoustic bioprinting

In acoustic DBB, droplets of liquid material from an open pool are ejected exploiting an acoustic field and without having to use one or more nozzles. The printer features a piezoelectric substrate on which interdigitated gold rings are placed to generate surface acoustic waves on demand. When the waves, focused at the interface between the ink and the air near the channel exit, generate a force higher than the bioink surface tension, the ejection of the material droplets occurs [32]. The main advantage of acoustic bioprinting resides in the open-pool nozzle-less ejection system, which eliminates the shear stress experienced when passing through a nozzle and so decreases both the risk of damaging the cells in the bioink and clogging the nozzle.
The main advantage of acoustic DBB is the absence of the use of nozzles, meaning that the problem of nozzle clogging and cell damage due to the shear stresses experienced by cells as they pass through a nozzle is eliminated.

Valve-jet bioprinting

In valve-jet BioP, the material contained in a pressurized fluid chamber

is expelled through an electromechanical valve that rapidly opens and closes based on applied voltage pulses [32].
Compared to the inkjet-based BioP, this technique, on the one hand, has the possibility of processing materials with higher viscosities (up to 100 Pa s) but on the other hand, it works at lower speeds and distributes larger droplets, resulting in a lower resolution [14]. Furthermore, post valve-jet BioP cell viability decreases following a decrease of diameter and an increase of pressure [33, 34].

Laser-assisted bioprinting

LAB represents those technologies which use a light source for printing a bioink. Vat photopolymerization (VP) and laser induced forward transfer (LIFT) belong to this class.

Vat photopolymerization
The most common technology in LAB is VP. In VP a light source is used to start the polymerization process of a resin or monomer solution contained in a vat. An important parameter of the VP process is the reaction kinetic that influences the printing time and the layer thickness. The reaction kinetic can be controlled by changing the light source power, the scanning speed, and the concentration of monomer and photoinitiators (PIs) [35]. In the BioP field, three VP technologies have been applied: stereolithography (SLA), digital light processing (DLP), and two photon stereolithography (TPP).

SLA uses a focused laser beam as the light source. The process starts with the printing bed positioned just below the solution surface. After that, the laser beam starts scanning the object cross-section and starts the polymerization reaction. When a layer is printed, the printing plate is further lowered (by a distance equal to the desired layer height) and the process is repeated until the 3D object is completed [36].

DLP uses a similar process that uses, instead of a focused laser, a UV or blue light projector that polymerizes an entire layer by projecting a cross-section image of the 3D structure. For this reason, DLP guarantees a significantly higher printing speed compared to SLA [37]. After printing, for both SLA and DLP technologies, the unpolymerized resin is removed from the 3D object and, to improve the mechanical properties, the printed structure is subjected to a post-processing step (e.g., heating, photopolymerization).
One of the main advantages of these techniques is the absence of nozzles

so that the cells do not experience harmful shear stress during the material deposition. On the other hand, factors that should be carefully evaluated are the operating temperature, the toxicity of the monomer solution or any additives (e.g., PI), and the possible damage due to UV light [38].

TPP is a recent technique that produces 3D structures at micro/nano scale. It uses two laser sources focused on a point to locally photopolymerize the material [39]. This technique can achieve high resolutions (as small as 150 nm) but also long printing times. Furthermore, the PI and monomer solutions commonly used in TPP are often cytotoxic to cells, limiting its application in the BioP field [14].

Laser-induced forward transfer

LIFT has been applied to the BioP field to realize biological structures with high accuracy and resolution [40, 41]. This LIFT technology is based on the use of a laser beam and a focusing system, a so-called "ribbon". The focusing system is composed of a glass support covered with a layer absorbing the laser energy (e.g., gold or titanium), a layer of biological material to be printed (for example, cells and/or hydrogel), and a receiving substrate on which the material is deposited.
Laser pulses focused on the absorbent layer generate high-pressure bubbles that push the biological material towards the substrate [16]. The main advantages of LIFT technology include: i) high resolution [14, 42] ; ii) the wide viscosity range of printable biomaterials; iii) high cell viability (>95%), due to the absence of a nozzle [43]. However, the technique also has several disadvantages: the process of preparing the ribbon and the cell coating is difficult and time-consuming, and since it is manual, it is also difficult to include multiple cell types in different layer positions. Furthermore, metal residues could be generated by the vaporization of the laser-absorbing metal layer and could be toxic in case of implantation of the printed structure.

A schematic representation of the three macro-groups of BioP technologies is reported in Figure 1.2.

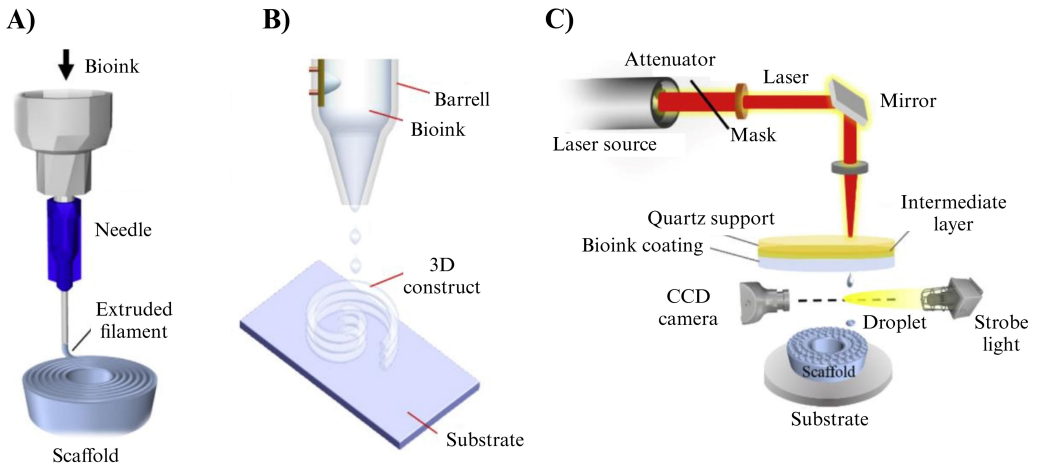

Figure 1.2: Main bioprinting technologies that have been applied to deposit bioinks. A) Extrusion-based bioprinting. B) Inkjet-based bioprinting. C) Laser-assisted bioprinting. Adapted from [44].

1.1.2 BioP approaches

Bioprinting is a promising field in a relatively early and evolving research phase. One of the current trends in the field of bioprinting is to investigate new approaches that overcome the limitations and improve the traditional BioP process.

In-situ Bioprinting

The translation of bioprinted constructs to clinical practice represents one of the main limitations of the traditional BioP approach. In fact, the bioprinted cellularized 3D structure, before being implanted into the body to replace damaged tissues or organs, must be cultured inside bioreactors for in-vitro tissue maturation and formation [22, 45]. Furthermore, the 3D bioprinted tissue is a fragile construct and its handling and transport is very challenging owing to: i) disruption in micro- and macro-architectures during the fixation process [46], ii)) impairment in the structural integrity, iii) risk of contamination due to transportation and manual implantation [47], iv) vulnerability of neighboring native tissue, v) highly sterile environment requirement on the entire routine [48]), and vi) low replication and low error tolerance rate [49]. Finally, it is possible that the shape or the morphology of the bioprinted structure may not match the actual size of the defect owing to the resolution limit of medical imaging, i.e., CT or MRI, on which the CAD model is based. Hence, this could not only lead to extended surgical time

owing to construct-trimming or gap-filling but also compromise the construct mechanical anchoring to the native tissues [50].

A possible solution for these limitations is *in-situ* bioprinting that consists in the direct print of bioinks onto and into the defect site in the living body. *In-situ* approach is advantageous compared to *in-vitro* approach because the human body functions as the effective "*in-vivo* bioreactor" where the bioprinted construct matures [49, 51].
Currently, two main *in-situ* BioP approaches are investigated (Figure 1.3).

1. The *robotic arm approach* consists of a 3-axis movable BioP unit that performs a real-time printing with controlled and precise deposition of bioink at the site of interest. This approach requires less human intervention even though the procedure is still performed under the surgeon's control using an advanced console controller. The starting point of this approach is a CAD model, then a specific software is used to produce a machine code which manages the bioink deposition. This code contains the instructions to control the spatial location of the deposition and define the artificial tissue architecture in a precise way. Finally, a robotic arm executes the machine code with high resolution and accurate movements. With this method, the robotic arm is able to perform complex tasks, can be controlled in force, and allows high resolution and accuracy movements [52, 53]. The robotic approach has found many applications for skin, cartilage, and bone regeneration [54–56]. One of the most promising devices developed in recent years is the Bio-AssemblyBot from Advanced Solutions Life Sciences.

2. The *handheld approach* involves a portable device with a bioprinting unit which allows the surgeon to direct deposit the bioink at the defect site by simply moving her/his hand.
   The handheld approach has many advantages over the robotic arm: i) more flexibility for time-dependent wounds, ii) capacity to deposit bioinks within crevices or beneath overhangs in the native tissue, iii) smaller size, iv) ease of moving and ease of sterilization, v) lower cost of device. Another feature, which can be both an advantage and a disadvantage, is that the printing results depend on the surgeon's hands. However, this approach can be useful for reconstructing not too complex and easily accessible defects [57, 58]. One of the most promising devices developed in recent years is the Biopen [59, 60]

The choice between these two approaches will mainly depend on the anatomical location and complexity of the damaged tissue [49].

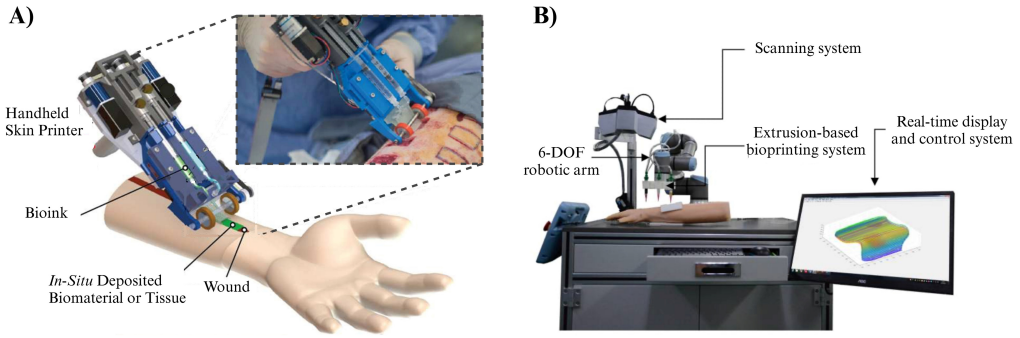

Figure 1.3: *In-situ* BioP approaches. A) Robotic arm system. B) Handheld approach. Adapted from [57, 61].

1.2 Mechanical cell stimulation: bioreactors

Given these premises, explained in Section 1.1, it is necessary to exploit dynamic culture conditions to promote *in-vitro* tissue regeneration.
Initially, in TE and regenerative medicine, standard static cell cultures were carried out to produce *in-vitro* tissue. However, it has been shown that the quality of some tissues improves if the cells are cultured under dynamic conditions that mimic the functioning mechanisms of the *in-vivo* tissue [62].
For this purpose, the use of bioreactors has been introduced in the context of cell culture. The main task of bioreactors is to provide physical stimuli to cells improving the regeneration of *in-vitro* biological tissues, as demonstrated by many scientific works [63–66]. However, in addition to providing physical stimuli, bioreactors can perform other tasks such as improving nutrient transport to the center of the 3D scaffold, cell seeding, and providing cell culture information (such as pH, oxygen, and temperature).
To develop a bioreactor, three steps must be considered (Figure 1.4).

1. Design, in which the use of computational methods can deeply support this stage.

2. Fabrication, in which AM-based techniques allow to obtain versatility and freedom in bioreactor shape.

3. Biological validation, in which the effects of external stimulation on cells in culture are evaluated.

TE Bioreactors have been implemented for the application of different types of physical stimulus: perfusion, mechanical, electro/magnetic. The type of

stimulation determines the final design of the bioreactor. Regardless of the final application, the basic general requirements must be met and then the specific stimulus requirements must be carefully chosen.
Since this is an extremely broad field, in this discussion we will focus on mechanical bioreactors that are the most widely used category in the muscle tissue field of our interest.

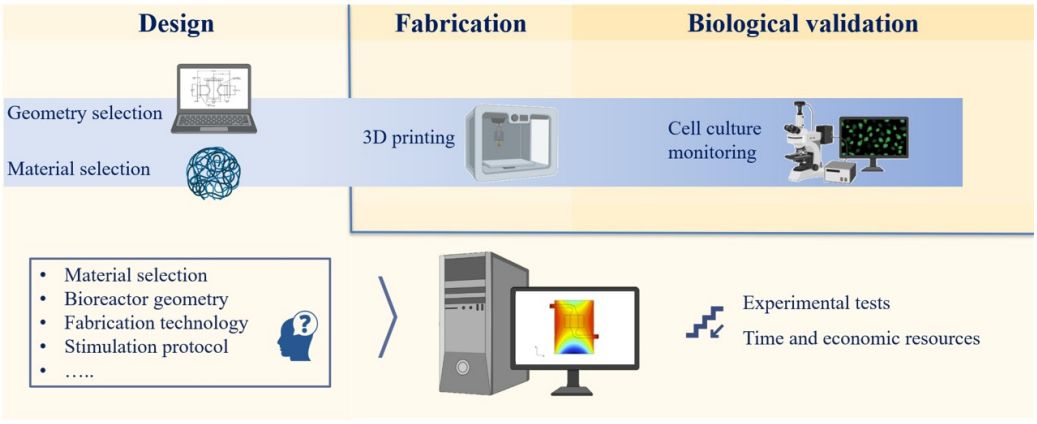

Figure 1.4: Workflow for the development of a bioreactor [67]. To develop the most performant bioreactor, three steps must be considered. 1) Design, in which the use of computational methods can deeply support this stage. 2) Fabrication, in which AM-based techniques allow to obtain versatility and freedom in bioreactor shape. 3) Biological validation, in which the effects of external stimulation on cells in culture are evaluated. Figure adapted from Gabetti *et al.* [68].

1.2.1 From design to validation

A widely used class of bioreactors is the mechanical one, among these we can find compression and traction bioreactors, which can be designed for both static and dynamic loading. Mechanical bioreactors are also divided into macro- and micro-bioreactors based on their size which can vary in the m-mm or in the mm-μm window, respectively.
Mechanical bioreactors have been studied on various tissues, in particular in the field of muscle tissue regenerative medicine. The development of this type of device is structured, as mentioned in the Section 1.2, in three general phases: design, fabrication, and biological validation.

Design

The final application, such as providing mechanical stimuli, is crucial in the design of the bioreactor system; to this end, in fact, specific stimulus requirements must be carefully chosen.
However, whatever the final application, general basic requirements (e.g., material selection, design mechanism, and scale-up strategies) must be satisfied.

General requirements. Among the general requirements for the mechanical bioreactor design, the choice of materials is a very important step because it affects many aspects. First, any material involved in the cell culture environment must not cause any adverse reactions and negative interference with cell proliferation and/or differentiation; for this reason, biocompatible, bioactive, or bioinert materials must be chosen. The materials must be non-degradable and non-porous to avoid fluid leakage problems from the bioreactor. Furthermore, the bioreactor culture chamber must be well isolated from the external environment to avoid contaminations.
A further constraint is that the bioreactor requires the presence of an environment characterized by a humid atmosphere at 37 °C, which is the one used for cell culture. For this reason, the selected materials must be compatible and usable in this condition.
In addition, each component of the bioreactor culture chamber must be sterilizable, possibly by autoclaving, UV light, or alcohol, which are the most widespread and commonly applied sterilization methods in a biological laboratory.
Finally, the bioreactor design should be thought of as a simple and user-friendly mechanism, for example with rapid assembly and disassembly of the device, which facilitates its use by laboratory personnel and reduces the probability of contamination.

Stimulus-specific requirements. About stimulus-specific requirements, in the case of mechanical macro-bioreactors, the class of compression devices generally consists of a motor, a system for providing linear motion, flat plates or handles, and a control mechanism. The load is transferred to the structures evenly via the flat plates. The design of traction macro-bioreactors is very similar to that of compression ones; however, they differ in the method of transferring force to the structure. Instead of flat plates as in a compression bioreactor, handles are needed to lock the scaffold into the device to apply tensile force. Alternatively, tensile deformation can also be applied to a structure by anchoring the structure to a rubber membrane which is then deformed.

Regarding mechanical micro-bioreactors, mainly traction stimulation devices are used. They usually consist of a control system, a stretching strategy induced by a vacuum pump, and a microfluidic chip equipped with an elastic membrane that acts as a support for cell culture.
Therefore, both in macro- and micro-bioreactors a mechanical stimulus is applied but in a different way: in macro-bioreactors the stimulus is provided by exploiting macroscopic cellular chambers and generally motor actuation systems; in micro-bioreactors the stimuli are provided by exploiting the deformation of a flexible membrane incorporated into a microfluidic chip and generally actuation systems based on vacuum pumps.

Given these premises, the design of a bioreactor requires the definition of a large number of process variables. To this end, several works have proposed the use of numerical tools to support bioreactor design by avoiding trial-and-error experimental approaches, reducing costs and time. In Section 1.2.2 this topic will be explored in depth and some literature examples will be presented.

Fabrication

Once the optimal bioreactor design has been selected, the next step in the device development process is fabrication. To date, different technologies can be employed for the fabrication of bioreactors. These technologies can be divided into traditional, such as subtractive processes, and more recent approaches, like AM.
The subtractive manufacturing process, e.g., CNC milling, starts with a block of material and creates the final product by subtracting, in a controlled way, material where needed. Large-scale production of identical components is easy using these conventional approaches, however, it is difficult to produce 3D bioreactors with complex geometry [69].
As opposed to subtractive manufacturing methodologies, AM approach involves adding material in a layer-by-layer process, to build the final object. The use of this technology enables the production of complex and custom-designed structures impossible to be manufactured with standard technologies. Actually, AM, most commonly known as 3D printing, is widely used for the rapid prototyping of bioreactors [70]. However, the increasingly low cost and the development of advanced materials for this technology have made it possible to extend its application from prototyping to production [71]. 3D printing also ensures the bioreactor suitability for applications such as cell

culture and *in-vitro* testing [72].
Several scientific studies have reported the fabrication of mechanical bioreactors using 3D printing techniques. Janvier *et al.* designed a sterilizable and reusable bioreactor consisting of a chamber with six independent wells that was 3D printed in PLA using an Ultimaker 2+. Subsequently, the device was waterproofed using a commercially available coating (XTC-3D, an oxirane resin) [73] and the culture wells were additionally coated with Sylgard-184 PDMS to reduce adhesion. Instead, in the study by Banik *et al.*, the small parts of the bioreactor were printed in SLA using a FormLabs Form 1+ desktop 3D printer while, due to the larger surface area and longer printing times, the base of the bioreactor was printed by selective laser sintering with Nylon 12 material [74].

Biological effects

Finally, the last step in the bioreactor development process concerns the validation in terms of evaluating the biological effect of external stimulation on cell behavior. In this context, numerous studies have demonstrated the fundamental role of mechanical stimulation in the regulation of skeletal muscle cell behavior [75, 76].
A pioneering study conducted by Vandenbergh *et al.* revealed that embryonic chicken myoblasts on a collagen-coated substrate aligned parallel to the strain direction under a slowly increasing uniaxial strain rate of 0.35 mm/h for 3 days [77]. Muscle hypertrophy, increased protein expression, and DNA content were observed.
Subsequently, the majority of studies have been performed to optimize strain parameters including direction, duration, and frequency to obtain the desirable cellular response.
In this context, most previous mechanological studies have been based on 2D experimental designs, such as the use of cell-seeded elastic membranes [78–80], or on 3D constructs fabricated using the molding technique [76, 81, 82].
Candiani *et al.* aimed to study the effect of mechanical conditioning on skeletal tissue development [78]. Muscle engineered constructs were obtained by seeding and culturing murine skeletal muscle cells on electrospun membranes. After 5 days of static culture, skeletal muscle constructs were transferred to the bioreactor and further cultured for 13 days, experimenting with an elongation pattern to resemble mouse development and growth. Results showed that, at day 10, the applied stretch model led to an eight-fold increase in myosin accumulation in the cyclically stretched constructs compared to the

corresponding static controls.
In the study by Powell *et al.* [82] improved human bioartificial muscles are fabricated by suspending muscle cells in collagen/MATRIGEL and casting into a silicone mold containing end attachment sites. Then, engineered tissues are exposed to cyclic stretch for 8 days resulting in an increase in the mean myofiber diameter by 12% and in the myofiber area percentage by 40%. However, the role of tensile stimuli in regulating muscle cell behavior in 3D bioprinted constructs has been poorly investigated. Only Xuan *et al.* [83] have recently attempted to customize a commercial bioreactor to cyclically stimulate 3D bioprinted constructs loaded with smooth muscle cells (SMCs). The results show that the cyclic equiaxial stimulation significantly increased the differentiation of SMCs.

1.2.2 Computational tools to support design

As mentioned in Section 1.2, the design of a bioreactor requires the definition of a large number of process variables. To this end, several works have proposed the use of numerical models to support the design of bioreactors avoiding experimental approaches of trial-and-error, reducing costs and time. Indeed, the key value of computational simulations is the ability to modify and study the effects of bioreactor design with respect to one, more, or combined inputs and by changing their values, without having to build actual physical models, or to run a large number of experimental tests. Furthermore, visualization of the magnitude and orientation of the physical force, possible thanks to the simulation package, allows to determine the efficacy of the system in a more practical way and to better optimize bioreactor design. The numerical strategy was applied for the optimization of the design of bioreactors exercising different types of stimulation: perfusion, mechanical, and electrical.
Concerning mechanical bioreactors, several works have focused from a computational point of view on the study of the mechanical, tensile or compressive, stimulus provided by TE bioreactors. The effect was analyzed both at the cellular level in terms of cell concentration or ECM spatial distribution but also in terms of strain or shear stress generated by the imposed stimulation.

Among the computational works on mechanical macro-bioreactors, Milan *et al.* [84] and Byrne *et al.* [85] proposed models to study the effect of different compressive stimuli on tissue behavior. Both simulated, using the finite element software Abaqus (Dassault Systemes, Waltham, MA), compressive loads applied to scaffolds via a rigid plate. Milan and colleagues [84] simu-

lated a cyclic loading while Byrne *et al.* [85] simulated a static loading. Milan *et al.* [84] model used the precise geometry reconstructed via μ-CT scans but it did not take into account the scaffold degradation. In contrast, Byrne *et al.* [85] model used a model 3D printed scaffold but it took into account the aspect of scaffold degradation. Results showed that bone maturation increased with low compressive loads and high porosity while very high levels of scaffold degradation did not ensure sufficient structural integrity before cell differentiation occurred.
In another model, developed by Soares *et al.* [86] the tissue formation driven by mechanical tensile stimuli imposed by a macro-bioreactor was simulated (Abaqus (Dassault Systemes, Waltham, MA). The model showed to correctly predict experimental data obtained with different cell types. Furthermore, stretching increased collagen formation and uniformity of structural composition. The model could be used to optimize mechanical stimulation parameters, such as strain and frequency.

The *in-silico* strategy has also been used in the field of mechanical microbioreactors to evaluate the deformation imposed during the actuation phase and for the structural optimization of the bioreactor. In the study by Pavesi *et al.*, FEM simulations were applied (Abaqus/Standard 6.10-1), to evaluate the deformation imposed on cell monolayers when negative pressure is applied to the actuation channels of a microfluidic chip [87]. The model allowed to identify a configuration capable of mimicking physiological tensions (i.e., 0-8%). Conversely, He *et al.* developed a finite element method (FEM)-based computational model (COMSOL Multiphysics 4.2a, Stockholm, Sweden) to optimize the structural parameters of microfluidic chips for cycling cell elongation [88]. The simulation outputs indicate that, using inappropriate device parameters, the chip may exhibit a small stretch ratio or large variation in the z-direction. Consequently, the optimized parameters were found; they were able to maximize the stretch ratio and minimize the z-displacement of the membrane. Indeed, when a negative pressure of -30 kPa was applied, the stretch ratio could reach 15% with a z-displacement of $\sim$1%.

In conclusion, the mentioned literature papers demonstrate how computational models can support the design phase of mechanical macro- and micro-bioreactors by optimizing the structure and predicting the strain applied to cells and its effect at the level of tissue growth. Furthermore, the discussion underlines the necessity and importance of model validation with experimental cell tests to confirm the predictivity and reliability of the computational model.

1.3 Bioprinting combined with the use of bioreactors

External stimulation delivered via bioreactors to bioprinted constructs can enhance cell differentiation within these scaffolds. However, this topic remains poorly investigated, as it is mainly studied on 2D constructs or on 3D constructs created using traditional molding techniques. To fill this gap in knowledge, new approaches are needed, such as mechanically stimulating the 3D bioprinted construct and integrating BioP into the stimulation device.
Some recent studies show first attempts towards these approaches. In the following, three literature examples, in which 3D bioprinted constructs were stimulated externally via magnetic, perfusion, and mechanical bioreactors, are reported.

Czichy *et al.*, presented the design of a device for non-contact cyclic magnetic stimulation of scaffolds consisting of a magnetizable bioink based on alginate, methylcellulose, and magnetite microparticles [89]. The force applied, through the use of a magnetic field, generated a deformation only of the samples and did not cause a movement of the magnetic particles of the bioink. By tailoring the magnetic field intensity, it was possible to achieve the desired elongations of 5-15%. The cytocompatibility of the stimulation approach was demonstrated for scaffolds bioprinted with Human mesenchymal stem cells (hMSCs) and chondrocytes with the primary intent of enhancing osteogenic/chondrogenic differentiation. These results demonstrated the suitability and versatility of the bioreactor which can subsequently be tested with other compositions of materials and cells.
In another study conducted by Mainardi *et al.* the effect of perfusion stimulation was studied, specifically fluid dynamic parameters, such as shear stress (SS), and their influence within the 3D bioprinted constructs in terms of mineral deposition were evaluated [90]. hMSCs were incorporated into 3D bioprinted porous structures made of alginate and gelatin. The 3D bioprinted constructs were cultured in an osteogenic medium evaluating the influence of different flow rates (0, 0.7, and 7 ml/min) on calcium and collagen deposition. The results showed that the bone volume increased significantly in the perfused groups compared to the static control and as the flow rate increased.
Finally, a recent attempt to study the effect of mechanical stimulation on 3D bioprinted constructs was made by Xuan *et al.* [83]. In this study, a commercially available mechanical bioreactor was exploited to cyclically mechanical stimulate 3D bioprinted constructs made of Gelatin methacryloyl (GelMA)/

alginate loaded with SMCs. The commercially cell stretching plates were modified with amino or methacrylate groups to promote adhesion of 3D constructs fabricated by BioP. After 6 days of stimulation, the effects of mechanical stimulation on the expression of contractile markers at the mRNA and protein levels were analyzed. Methacrylate-modified surfaces supported stable adhesion of the 3D constructs to the membrane and facilitated cyclic mechanical stimulation, which significantly increased the expression of contractile markers at the mRNA and protein levels.

In light of this, the reported studies demonstrate that external stimulation applied on bioprinted constructs has a significant influence on the behavior of encapsulated cells as briefly summarized below and in Table 1.1.

- Magnetic stimulation applied to bioprinted scaffolds with hMSCs and chondrocytes enhanced osteogenic/chondrogenic differentiation.
- Perfusion stimulation applied to bioprinted scaffolds with hMSCs significantly increased the bone volume.
- Mechanical stimulation applied to bioprinted scaffolds with SMCs significantly increased the expression of contractile markers at mRNA and protein levels.

Table 1.1: Summary of literature studies in which BioP was combined with the use of bireactors.

Year	Author	Bioreactor type	Applied stimulus	Bioink	Results
2022	Czichy *et al.* [89]	Magnetic bioreactor	Magnetic field to generate a cyclic bioink elongation of about 5-15% for over 14 days with a duration of 3 h per day	Alginate, methylcellulose, and magnetite microparticles + hMSCs and chondrocytes	Enhanced osteogenic/ chondrogenic differentiation
2022	Mainardi *et al.* [90]	Perfusion bioreactor	Different flow rates (0, 0.7, and 7 ml/min)	Alginate and gelatin + hMSCs	Increased bone volume as the flow rate increased
2023	Xuan *et al.* [83]	Mechanical bioreactor	Semisinusoidal pulse of 1 s delivered at a frequency of 0.5 Hz. Cells were continuously stimulated at the same time every day for 1 h, for a total of 6 days	Gelatin methacryloyl / alginate + SMCs	Increased expression of contractile markers at the mRNA and protein levels

1.4 Gap to be filled, Thesis aim and organization

During the three years of PhD, my research focused on the use of engineering tools for the automation and standardization of the BioP process for different applications in the TE field. In particular, I dealt with various aspects of this area including:

- the preparation of biomaterials and their printability;
- the design of the scaffold (e.g., geometry);
- the optimization of 3D printing and bioprinting processes (e.g., setting printer parameters, multi-material geometries, *in-situ* BioP strategies);
- the implementation of computational methods (e.g., finite element analysis) to support the design of devices;
- *in-vitro* experimental tests (e.g., mechanical and biological).

I studied all these aspects for different applications in the TE field (for more details refer to Section A.1 in the Appendix). In this thesis a comprehensive example of how these aspects combine with each other is reported. Since, studies relating to mechanical stimulation applied on bioprinted constructs are very few and furthermore the integration of 3D BioP and mechanical stimulation remains underexplored, the proposed project deals with the design, supported by computational tools, manufacturing, and benchmarking of a BioP-integrated mechanical platform for TE applications in the field of skeletal muscle regenerative medicine.

Background

3D BioP, as mentioned in Section 1.1, is a widely used technique in the TE field; among the many applications, one is that of the skeletal muscle regenerative medicine.

In this regard, in the lab BioP@UniPV, the BioP technique had already been applied in the skeletal muscle area, thanks to a collaboration with the group of Professor Gabriele Ceccarelli (Department of Human Anatomy of the University of Pavia) [5]. In the first preliminary work [5], we used BioP to recreate a muscle fiber model *in-vitro* obtaining promising results. Indeed, the bioprinted constructs showed excellent cell viability (>94%) and cell elongations up to 21 days of culture (Figure 1.5). However, the following two main limitations were observed.

1. The escape of cells from the construct and their colonization and growth on the Petri dish.

2. The inhomogeneous and pronounced cellular differentiation at the edges of the structures.

To overcome these problems, a possible solution is to create supports to contain the bioink and avoid the colonization of the cells on the Petri dish and furthermore, promote differentiation through the development of a device capable of providing mechanical stimulation.

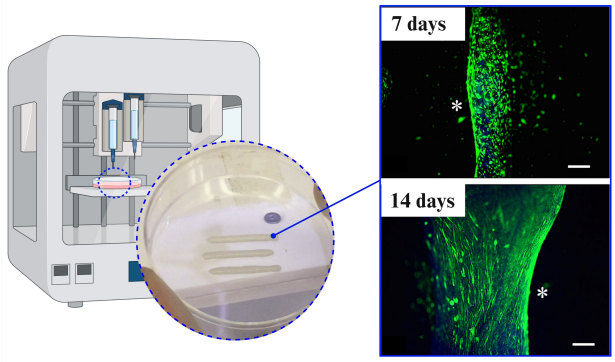

Figure 1.5: BioP process to recreate a muscle fiber model *in-vitro*. 3D bioprinted geometric lines formed by a layer with focus on the biological results, highlighting excellent viability and the presence of cell elongations both at 7 and 14 days of culture. Adapted from [5].

Thesis aim

In this context, the **PhD project proposes the design, manufacturing, and benchmarking of a BioP-integrated mechanical platform for TE applications in the field of skeletal muscle regenerative medicine**. The platform is intended for mechanically stimulate elastic supports that contained the cell-loaded hydrogel directly bioprinted inside the bioreactor.

Regarding **supports**, **two different manufacturing strategies** have been investigated.

- Exploiting the first strategy, supports are fabricated by combining the 3D printing of a thermoplastic biomaterial (polycaprolactone) and the 3D BioP of a commercial biocompatible hydrogel (CELLINK Fibrin) loaded with murine myoblasts (C2C12 cell line). In the following is refereed to **co-printing**.

- In the second manufacturing strategy, supports are fabricated **by combining the molding technique** of a hyperelastic material (polydimethylsiloxane) **and the 3D BioP** of the CELLINK Fibrin biocompatible hydrogel loaded with C2C12 cells.

About the **mechanical platform**, it should support the simultaneous stimulation of at least three elastic supports ensuring a homogeneous transmission of deformation. Therefore, to design and identify the geometry of the device, **computational models** were used predicting the post-stimulation behavior and avoiding the trial- and-error procedure. The device was then **3D printed and validated**, in terms of transmission of mechanical stimulation to the 3D constructs, integration of the BioP phase, and biological effect of the dynamic culture on muscle cells.

This project was carried out in collaboration with the group of professor Gabriele Ceccarelli (Department of Human Anatomy of the University of Pavia).

Project workflow and thesis outline

The project workflow, illustrated in Figure 1.6, involves three primary phases: 1) in the first phase, stretchable supports suitable for bioprinting and long-term cell culture were designed and produced; 2) in the second phase, computational tools will be used to design the mechanical platform. Subsequently, a prototype of a cyclic bioreactor was developed with the addition of sensors connected and monitored by a Cloud platform. 3) Finally, the third phase will involve the *in-vitro* validation of the proposed platform in terms of transmission of the mechanical stimulation to the 3D construct, integration of the BioP step, and the biological effect of dynamic culture on muscle cells. Each of these phases is described in a chapter of this thesis and a summary of the topics covered in each chapter is provided below.

- Chapter 2 presents the **design and development of the containing supports exploiting the 3D co-printing and the molding techniques**. Regarding 3D co-printing, as manufacturing material, the polycaprolactone (PCL) and a commercial biocompatible hydrogel (CELLINK Fibrin) loaded with C2C12 muscle cells were selected. First, the effect of co-printing on cell behavior were evaluated. Afterwards, various supporting structural geometries were created to investigate their effect on cell differentiation. Finally, the comparison between the different geometries is reported.

About molding technique, polydimethylsiloxane (PDMS) was selected as the manufacturing material due to its elasticity. Then, the elastic supports were mechanically characterized to analyze their elasticity and tensile strength.

- Chapter 3 shows the **design and development of the mechanical stimulation platform supported using computational tools**. First, the implementation of a basic computational model simulating the tensile testing of elastic supports is reported. This model was calibrated and validated using experimental test data and then, it was implemented for supporting the design of the mechanical platform. In particular, various configurations of the platform were designed and their behavior after the stretch application was assessed. A printing test was performed for validating computational results and selecting the correct configuration. Finally, a cyclic version of the platform with sensors connected to the Cloud is presented.

- Chapter 4 illustrates the **testing and benchmarking of the mechanical platform in terms of transmission of mechanical stimulation to the 3D constructs, BioP integration, and biological effect of the dynamic culture on muscle cells**. Regarding the transmission of mechanical stimulation to the 3D constructs, an experimental and numerical assessment of the stretch of the hydrogel printed on the supports is proposed. Several hydrogels have been tested experimentally. The experimental results were then compared with the computational ones obtained through the previously defined and validated model. About the integration of BioP, a feasibility study of the process integration on the platform under sterile conditions is presented. Then, the impact of the mechanical stimulation on the *in-vitro* differentiation of murine C2C12 myoblasts loaded in a fibrin-based hydrogel and deposited on the stretchable supports is reported.

- Chapter 5 discusses the **conclusions and future developments** of this thesis focused on validating the platform using new cell types and/or biomaterials and validating its use for TE applications such as drug screening.

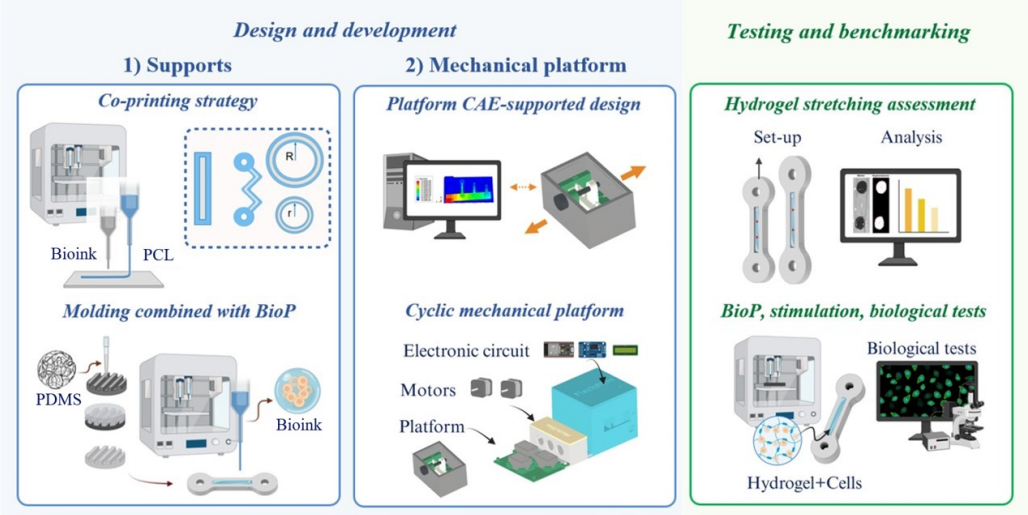

Figure 1.6: Thesis workflow. It started with the design and development of the supports that can contain the bioink and at the same time allow the application of a mechanical stimulus. Two manufacturing techniques were investigated for the creation of the supports: co-printing and molding. Subsequently, the mechanical platform was designed thanks to the support of numerical tools. Then, a cyclical and sensorized version of the platform was developed. Finally, the device was validated, in terms of transmission of mechanical stimulation to the 3D construct, integration of the BioP phase, and biological effect of the dynamic culture on muscle cells.

Chapter 2

Design and development: stretchable supports

The 3D BioP technique has been used to create 3D muscle biological constructs. However, cell maturation does not always succeed. Referring to our experience for example, as mentioned in Section 1.4, cells elongate particularly in the peripheral areas and come out of the hydrogel.
The use of supports that can contain the bioink and at the same time allow the application of a mechanical stimulus thanks to their elasticity could promote, on the one hand, the cellular permanence inside the hydrogel and, on the other hand, an improved *in-vitro* differentiation of the cells encapsulated in the hydrogel. In this scenario, several mechanical devices for muscle repair and regeneration have already been proposed in the literature [76–82]; however, the role of tensile stimuli in regulating muscle cell behavior in 3D bioprinted constructs has been poorly investigated.
In this context, the platform proposes in this thesis is intended for mechanically stimulate elastic supports which contained the cell-loaded hydrogel directly bioprinted inside the bioreactor for muscle TE applications. To this end, two strategies for manufacturing the supports were investigated: i) 3D co-printing of PCL supports on top of which the hydrogel is deposited and ii) molding technique of PDMS supports on top of which the hydrogel is bioprinted. First, the effect of co-printing on cell behavior were evaluated. Afterwards, various supporting structural geometries were created to investigate their effect on cell differentiation.
About molding technique, elastic supports were fabricated and mechanically characterized to analyze their elasticity and tensile strength.

This chapter illustrates the design and development of the supports using the two techniques and provides details on the materials used and their preparation, 3D bioprinter technology employed, the design of the supports, the biofabrication processes.
The methods and results presented below pertain to the study published in 2023 [6].

2.1 Co-printing strategy

The application of co-printing in the field of muscle regenerative medicine is already reported in the literature. In these published works the co-printed engineered muscles showed high cell viability, good *in-vitro* differentiation [91, 92], and high *in-vivo* regenerative effect [92, 93]. However, none of these studies has yet investigated the possibility of making containing supports for the bioink using this technique and of studying the interplay between the bioprinted model and the substrate, although it is known that this may have a crucial role on myoblast's behavior [94–102]. In particular, the curvature feature, i.e., the use of circular, angled substrates with portions characterized by a certain radius of curvature, has been shown by several authors to improve cell proliferation [95–97]. Unfortunately, the effect of the geometrical curvatures on the process of myogenic differentiation is unclear and needs to be further elucidated. Therefore, finding the optimal substrate geometry that can improve myotube differentiation, alignment, and function is critical to engineering muscle tissues [103].
Based on these considerations, this section illustrates the design and development of the containing supports using the co-printing technique. Different structures were designed to understand how geometric cues maximize the differentiation of C2C12 murine myoblast cells. First, we evaluated the capability of the co-printing technique to realize substrates for cells-loaded materials by fabricating linear supports with a central channel made of PCL and containing the fibrinogen-based hydrogel loaded with C2C12 cells, previously selected [5]. Biological tests were carried out to evaluate cell viability and differentiation. Then, once the biological effect of the co-printing technique is verified, we moved on to its application to evaluate the substrate geometry influence on cell differentiation. To this aim, three different geometries including linear, circular with different outer diameters (OD), and hybrid structures (combining linear and circular features) were created and compared.

2.1.1 Material and preparation

For co-printing the supports, two commercial materials were used, a fibrinogen-based hydrogel (CELLINK Fibrin) and Poly(ε-caprolactone) pellets. The fibrinogen component of the selected hydrogel shown in our previous study to recreate a suitable microenvironment for the regeneration of muscle tissue *in-vitro* [5]. Once printed, the bioink was ionically cross-linked using a calcium chloride ($CaCl_2$)-based solution to develop a suitable structural integrity. Instead, PCL was selected because it is one of the widely used biomaterials in BioP due to its biocompatibility and mechanical strength. This polymer allows manufacturing supports with complex geometries for bioink containment in long-term cell cultures.
Details on the materials used for this project are described in the following paragraphs.

Polycaprolactone

Different biocompatible and biodegradable synthetic polymers, such as polylactic acid, polyglycolic acid, poly(lactic-co-glycolic acid), and poly(ε-caprolactone), have widespread for manufacturing scaffolds. Notably, for TE applications, including drug delivery systems, biodegradable sutures, and scaffolds for tissue regeneration, PCL is one of the biomaterials widely used thanks to the ability to realize complex shape. It possesses an excellent thermal stability and mechanical strength, and most importantly, it is FDA approved polyester [104]. Among its most important properties are biocompatibility, low cost, and biodegradability with a degradation that does not produce an acidic environment, unlike other polyester polymers.
For this project, PCL pellets (50 kDa) were purchased from Cellink AB (Gothenburg, Sweden).

CELLINK Fibrin and cross-linking

The experiments were performed using a commercially available nanofibrillated cellulose (NFC)/alginate-fibrinogen-based hydrogel (CELLINK® Fibrin). The hydrogel contains NFC, alginate, fibrinogen, and *in-situ* fibrin to provide a physiologically relevant environment for *in-vitro* muscle tissue generation. These nanosized fibrils make the bioink semi-translucent which allows cell imaging and analysis. CELLINK Fibrin contains low levels of endotoxins that allows creation of healthy and diseased tissue models with minimal interference with drugs during drug discovery and development research. In addition, the commercial kit includes an enhanced cross-linking

solution composed by ionic binding agent ($CaCl_2$) to develop a compound network with suitable printability and stability.
For this project, the Fibrin hydrogel was purchased from Cellink AB (Gothenburg, Sweden).

C2C12 cells

The C2C12 cell line used in this study was purchased from the American Type Culture Collection (ATCC, VA, US). Cells were cultured in T75 flasks, in DMEM growth medium (Dulbecco's Modified Eagle medium, DMEM; Sigma, Milan, Italy) supplemented with 10% fetal bovine serum (FBS), 1% penicillin/streptomycin, 1% glutamine, and 2% sodium pyruvate at 37 °C under a 5% CO2 atmosphere.
When 80% cell density was reached, cells were used for the experiments. C2C12 concentration in the bionk was approximately 25 x 10^6 cells/mL. Cell counting was performed using a Burker's chamber and an Eclipse TE200 microscope (Nikon).

2.1.2 3D bioprinter feature and printing setup

To co-print the selected materials the 3D bioprinter Cellink INKREDIBLE+ (Cellink AB, Sweden) was employed. It is a pneumatic extrusion-based 3D bioprinter equipped with two print-heads (PHs), a UV LED curing system (365 and 405 nm), and a high-efficiency particulate air (HEPA) filter. The PHs temperature can be set up to a maximum of 130 °C and their positioning system has a 10 μm resolution in the three axes. The bioprinter allows the extrusion of a wide range of biomaterials, both thermoplastic and hydrogel, in a viscosity range of 0.001 to 250 $Pa \cdot s$. INKREDIBLE+ is equipped with a patented clean chamber technology that allows it to be used directly on the laboratory bench. The HEPA 13 filter and positive air pressure ensure a sterile environment during the printing process.
In this thesis, the bioink was printed using a plastic cartridge and a 0.41 mm diameter conical nozzle while PCL pellets were printed using an aluminium cartridge and a 0.5 mm diameter metal nozzle, which is able to withstand temperatures above 50 °C.
Before starting printing, INKREDIBLE+ needs to be homed and calibrated. The 3D bioprinter setup involves the following three steps.

- XYZ homing axes to position the first PH in the middle of the printbed.
- Z axis calibration to tune properly the distance between nozzle and printing bed, which is crucial for the printing of first layer.

- Pressure calibration to find the optimal value that enables a proper flow of material.

2.1.3 From the design to printing

The printing process involves a sequence of operations that includes three main steps described in the following.

- A virtual 3D CAD model is created and exported into stereo lithography interface (STL) format.

- The 3D CAD model is sliced in different layers and some parameters, such as layer height, perimeter, printing speed, infill pattern and percentage, are defined.

- Based on 3D printing technology and slicing process, a set of instructions, namely G-code, is created and exported to the 3D printer, allowing the precise control and construction of the model through a layer-by-layer deposition.

In this thesis, Autodesk Inventor software (Autodesk, United States) was used to create the solid 3D CAD model of the scaffold; while Slic3r, an open source software, was used for slicing. Repetier-Host (Hot-World GmbH & Co. KG., Germany) was used as printer interface for activating the printing process.

Supports design

The present paragraph proposes the design and development of 3D co-printed supports containing a cell-loaded hydrogel, intended for modeling skeletal muscle *in-vitro*.
To investigate the substrate geometry effect on murine myoblast differentiation, three different structures were co-printed: linear, hybrid, and circular with different ODs.
Figures 2.1A and 2.1B summarize the geometries designed and used for the 3D co-printing experiments. Linear and serpentine-like structure length was set at 20 mm, while the OD of circular structures was set at 10 and 5 mm. The channel width was 0.93 mm for all geometries. This channel thickness was the minimum distance we were able to achieve when printing PCL substrates (data not shown).

3D co-printing process

The total number of constructs to be printed for the biological tests was 50, comprising 18 samples for Live/Dead analysis and 32 samples for gene expression analysis. Each support printing required approximately 20 minutes, so the co-printing process was carried out in two separate steps.

In the first printing step, all the PCL supports were printed. In the second step, the bioink was deposited into the appropriate channels of the supports. This two-step approach was facilitated by using a reference on the printing plate, which allowed for precise repositioning of the Petri dishes during the second round of printing.

This method was chosen specifically to address concerns about the lengthy printing time, which could lead to cell precipitation and result in cellular inhomogeneity within the constructs. Additionally, prolonged heating of the PH2 could compromise cell viability. Since the print heads (PHs) of the INKREDIBLE + bioprinter are made from metallic and conductive materials, heating PH1 to print the PCL generates a slight temperature increase in PH2, reaching up to about 45 °C. These thermal stresses can affect the rheological properties and structural stability of the hydrogel, as well as the viability of the encapsulated cells [105].

PCL printing

Before the first phase of the co-printing process, the bioprinter was positioned under a biological sterile hood. The aluminum cartridge was filled with PCL pellets, then inserted into the PH1 printer, and heated to 120 °C for 30 minutes to sterilize the material. A 3D-printed reference, sized to match the diameter of the Petri dish and marked with a white dot on the front, was placed on the printing plate (Figure A.1C). The front of the Petri dish was marked with a permanent black marker to ensure it could be repositioned in the same spot during the second printing step. UV light was activated for 1 hour to sterilize all surfaces.

The printing temperature for the PH1 was set to 90 °C. The XYZ axes were homed, the Z axis was calibrated, and the pressure and printing speed were adjusted according to the PCL guidelines (300 E^3 Pa and 0.75 E^{-3} m/s for the PCL). The G-code was loaded onto the bioprinter's SD card, and the PCL supports were printed. After the printing was completed, the samples were placed under UV light for a second sterilization step.

Hydrogel printing

In the second phase of the co-printing process, the bioprinter was placed under a biological sterile hood. The reference material was positioned on the printing plate, and UV light was activated for one hour to sterilize all surfaces.

The bioink was prepared by mixing hydrogel with C2C12 cells in a 10:1 ratio. This bioink was then transferred into a plastic cartridge, to which a conical nozzle with a 0.41 mm inner diameter was attached. The cartridge was subsequently inserted into the PH1 bioprinter. The printing temperature for the PH1 was set to room temperature (RT), and the XYZ axes were calibrated.

For the z-axis calibration, the x- and y-axes were adjusted to align the nozzle with the support channel designated for printing. The z-axis was then lowered until the nozzle made contact with the channel surface. After completing the z-calibration, the x- and y-axes were reset to their initial positions at the center of the printing bed.

The printing speed was adjusted according to the hydrogel guidelines, which specified a range of 10-15 E^3 Pa and a flow rate of 0.01 m/s for the PCL. The parameters for both the first and second phases of the co-printing process are summarized in Table 2.1.

The Petri dish was positioned by aligning a black mark drawn on it with a white line on the reference material placed on the printing plate. The G-code was then loaded onto the bioprinter's SD card, and the bioink was printed onto PCL supports within the channels.

After printing, the constructs were immersed in a $CaCl_2$ solution for five minutes. Following this, the cross-linking solution was removed, and DMEM culture medium was added. The 3D co-printed constructs were incubated at 37 °C in a humidified atmosphere containing 5% CO_2, and they were cultured for up to 21 days, with the culture medium refreshed every three days.

Four days post co-printing, the differentiation process of the C2C12-laden bioink was initiated using a differentiation medium composed of DMEM supplemented with 2% fetal bovine serum. Figure 2.1C and A.1 provide a schematic representation of the described 3D co-printing process.

Table 2.1: Summary of the operational parameters set for the co-printing process.

Operational parameters	**PCL**	**CELLINK Fibrin**
Extrusion pressure [kPa]	300	10-15
Conical nozzle diameter [mm]	0.5	0.41
Printing speed [m/s]	7.5 $E^{-}3$	0.01
Printing temperature [°C]	90	RT

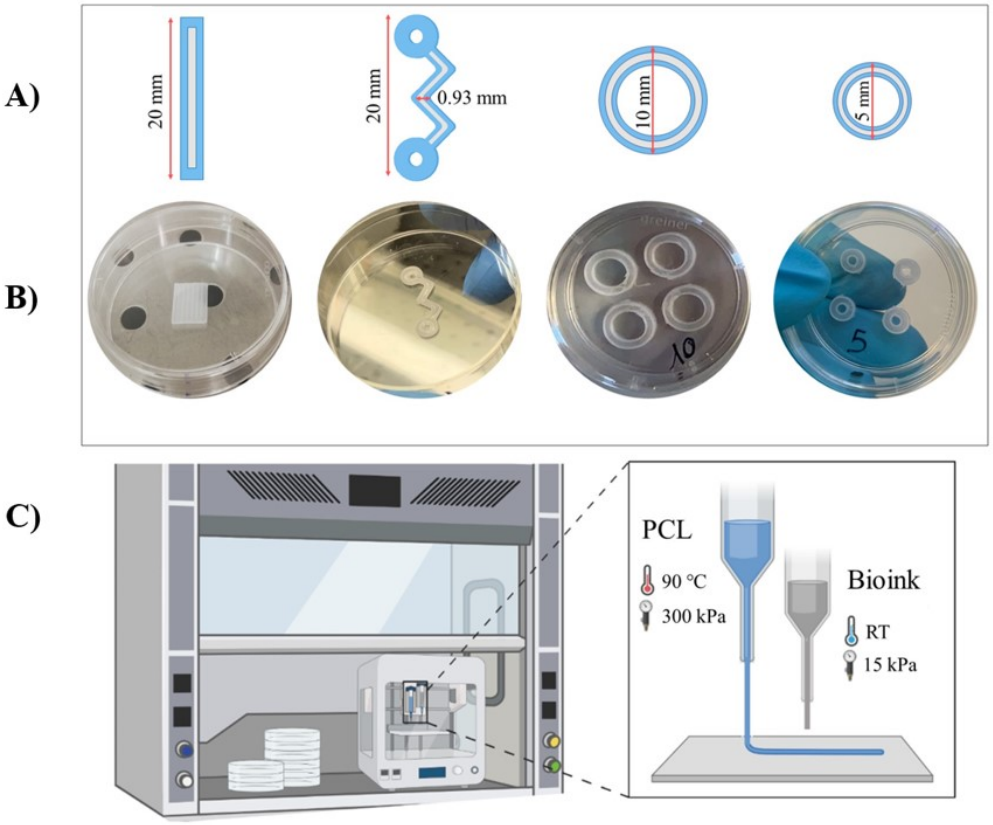

Figure 2.1: Design and development of the different 3D co-printed supports - linear, hybrid, and circular with different outer diameters (OD 10 mm, OD 5 mm). A) Schematic representation of the structures CAD design. B) 3D printed PCL constructs. C) Illustration showing the biofabrication process, selected materials, and printing parameters.

2.1.4 *In-vitro* biological characterization

First, we evaluated the capability of the co-printing technique to realize substrates for cells-loaded materials. Then, once the biological effect of the co-printing technique had been studied, we moved on to its application to evaluate the influence of the geometry of the substrate on cellular differentiation.

Co-printing biological effect

As a preliminary test, the effect of co-printing on cell differentiation was tested. To this end, we performed gene expression analyses, exploiting the Real-Time quantitative Polymerase Chain Reaction (RT-qPCR) technique, comparing structures with the same geometry (linear) realized with different techniques, i.e., BioP and co-printing. Data related to bioprinted structures were derived from our previous study [5]. The bioprinted constructs are named F which stands for fibrinogen-based hydrogel while the co-printed structures are named F + PCL as the same hydrogel has been deposited on a PCL support. The expression of two master muscle genes was quantified: MyoD, characterizing early muscle differentiation, and MCK, indicating late differentiation and maturation of muscle tissue. Analyzes were performed at 7, 14, and 21 days of culture in differentiative conditions (Figure 2.2) following the protocol reported in the appendix Section A.2.2. For each condition, i.e., for each time-point and gene analyzed, 3 biological structures were evaluated.
At 7 days, the MCK gene was significantly expressed by cells cultured in the co-printed linear structures (Figure 2.2A). At 14 days co-printing significantly improves the differentiation showing high expression levels of both MyoD and MCK genes. At 21 days, no statistically significant differences in MCK expression were found; however, MyoD was differentially expressed in the bioprinted structures, showing a still early differentiation.
The results suggest that the co-printing technology does not impair cell viability, and indeed, significantly improves the differentiation at 14 days. However, following the excellent results obtained at 14 days, a decrease in both MyoD and MCK expression was observed at the subsequent 21-day time-point. Considering MyoD, its expression significantly decreased, as we expected, because it is considered the master gene of early myogenic differentiation. While, regarding the MCK, we hypothesize that, following the high expression peak at 14 days, at 21 days, the translation process is favored compared to the transcription process [6].
Considering these findings, all the 3D structures that will be examined below

in the discussion have been created through 3D co-printing.

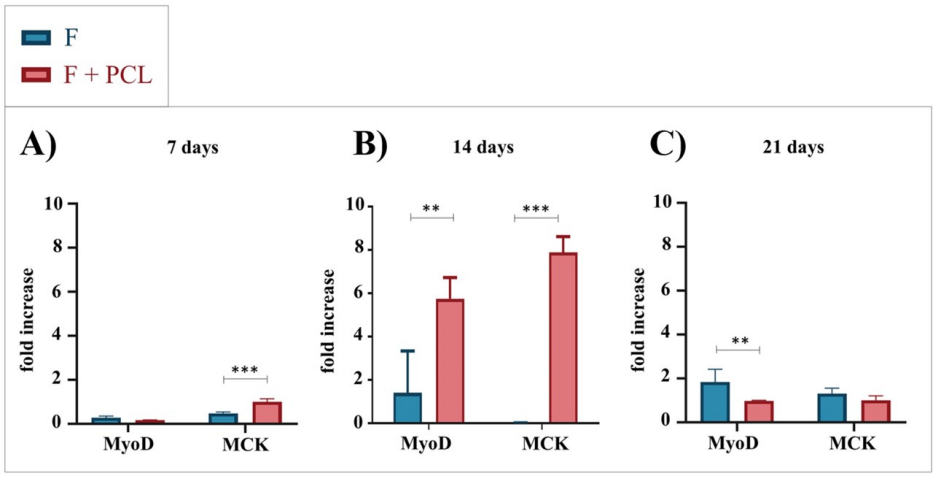

Figure 2.2: Gene expression analysis of C2C12 cells cultured into linear structures bioprinted (F) or co-printed (F+PCL) at A) 7, B) 14, C) 21 days. Statistically significant values are indicated as $*P < 0.05$, $**P < 0.01$, and $***P < 0.001$. Analysis of variance test was performed to evaluate data significance. MyoD and MCK genes were analyzed for evaluating early and late muscle differentiation respectively. For each condition, i.e., for each time-point and gene analyzed, 3 biological structures were evaluated.

Comparison of all tested geometries

To evaluate the effect of substrate geometry on cell behavior we performed viability and gene expression analyses comparing all the considered geometries. The viability analyses were conducted exploiting the LIVE/DEAD assay and following the protocol reported in the Appendix Section A.2.2 while gene expression was evaluated performing the RT-qPCR and following the protocol reported in the Appendix Section A.2.2.

Cell viability

Live/Dead staining was performed at different time points during the culture (1, 7, 14, and 21 days) (Figure 2.3). For all geometries, at 24 hours after printing, cells are rounded shape and homogeneously distributed throughout the construct. Furthermore, at all time points and in all cases considered, cells demonstrated very high viability (>94%).
On day 7, C2C12 cells remained mainly round-shaped in the center of the

construct without merging to form myotubes. However, especially in linear constructs, an initial differentiation of C2C12 began at the edges of the 3D constructs, where cell elongation appeared. This is probably due to an inhomogeneous diffusion of the cross-linking solution or to lower oxygen and nutrient concentrations within the 3D constructs (Figure 2.3b).
Finally, at 14 and 21 days, C2C12 cells grown in linear and serpentine-like structures merged forming primordial myotubes even in the most central part of the 3D structure, and the alignment was promoted by the linear areas of the printed constructs (Figure 2.3d, h).
As for C2C12 cells grown in circular structures, at 7 and 14 days of culture, cells retain a rounded-shaped and slowly begin to elongate only at day 21, especially at the edges of the constructs (Figure 2.3n, r).
The elongation of C2C12 cells significantly decreased when printed in circular 3D structures (Figure 2.3i-r); otherwise, the linear structure appeared to significantly increase myotube formation, and the alignment of the myoblast is mainly located at the edges (Figure 2.3b-d).
Therefore, the Live/Dead results indicated that under differentiative conditions the linear structure effectively induced the alignment of myoblasts in particular at the boundary of the structure with respect to the other geometries tested. An inhomogeneous diffusion of the cross-linker in the center of the construct and/or a lower diffusion of nutrients/oxygen could be responsible for insufficient cell elongation.

Gene expression

Gene expression levels of C2C12 cells cultured under differentiative conditions in the different geometries at 7, 14, and 21 days were compared to evaluate the influence of the geometrical factor on the differentiation rate (Figure 2.4). The expression levels of MyoD and MCK genes in the 3D co-printed structures were detected by RT-qPCR and normalized by the PGK gene. MyoD was analyzed for the 7 and 14 days of culture to characterize early muscle differentiation, while MCK was analyzed for the 21 days of culture as it indicates cell differentiation and maturation of muscle tissue. For each condition, i.e., for each time-point and gene analyzed, 3 biological structures were evaluated.
At 7 days, the MyoD gene is differentially expressed in the serpentine-like structure. But, at 14 days, the linear geometry allows bursting cell differentiation, which reaches a very high gene expression value compared to all the other geometries examined. At 21 days, MCK is differentially expressed in the serpentine-like structure compared to the other ones.

Thus, we obtained the best gene expression results at the 14 days time point, especially with the linear geometry while the serpentine-like construct allows an improved late differentiation at 21 days.

In conclusion, the linear geometry was selected as it proves to be the best 3D structure to promote myoblast alignment along the printed filament in a short-time culture (14 days) and with the highest gene expression level. Furthermore, the application of the co-printing technique for the creation of cellular supports allowed us to overcome one of the limitations that emerged in our previous study [5], i.e., the containment of the bioink and the reduction of cell invasion on the Petri dish. However, based on the results of the viability and morphology tests, the cell differentiation remained inhomogeneous and pronounced at the edges of the 3D structures, as previously observed [5]. For this purpose, an idea to improve the homogeneity of differentiation could be the application of cyclic mechanical stimulation.

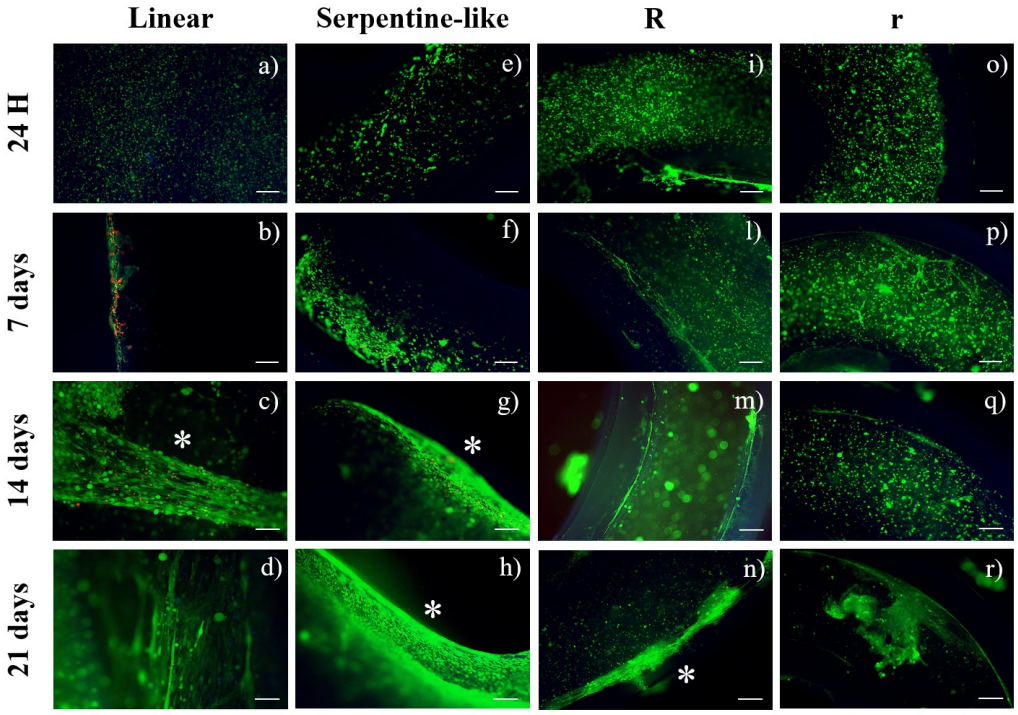

Figure 2.3: Live (green)/Dead (red) images of different 3D geometries at specific time points in differentiative conditions. (a-d) Linear 3D constructs; (e-h) Serpentine-like 3D constructs; (i-n) Circular 3D constructs with OD 10 mm; (o-r) Circular 3D constructs with OD 5 mm. Scale bar 50 μm. Cell elongation is highlighted by asterisks ($*$).

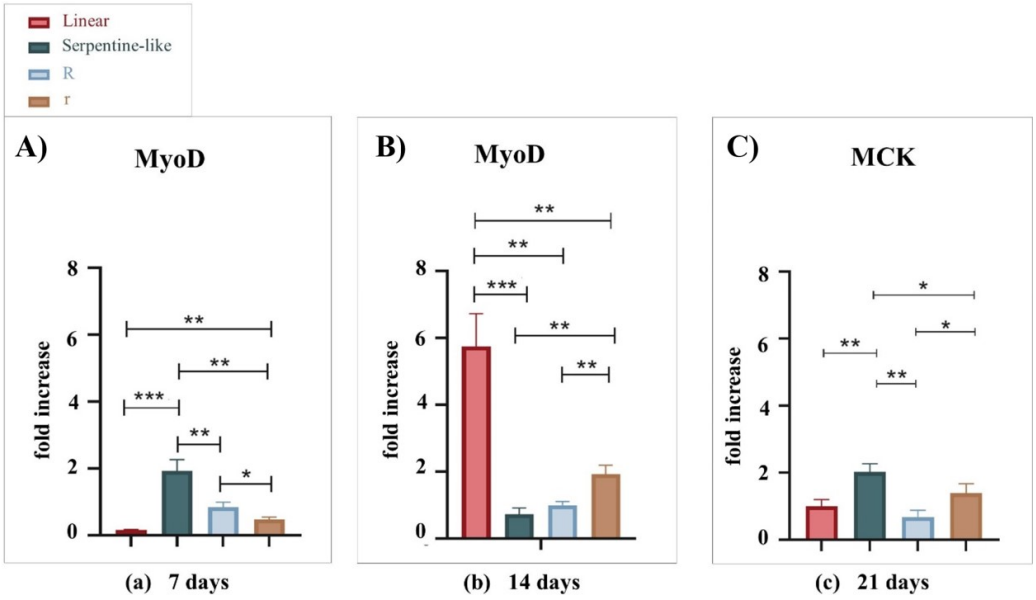

Figure 2.4: Gene expression analysis of C2C12 cultured into the different geometries tested (linear, serpentine-like, and circular) at 7, 14, and 21 days. A) MyoD expression by qRT-PCR at 7 and B) 14 days. C) MCK expression by qRT-PCR at 21 days. Statistically significant values are indicated as $*P < 0.05$, $**P < 0.01$, and $***P < 0.001$. Analysis of variance test was performed to evaluate data significance. R indicates structures with a 10 mm OD while r indicates those with a 5 mm OD. MyoD and MCK genes were analyzed for evaluating early and late muscle differentiation respectively. For each condition, i.e., for each time-point and gene analyzed, 3 biological structures were evaluated.

2.2 Molding strategy

Despite the success of the proposed co-printing strategy and the excellent results obtained, some limitations emerged. In particular, one of the main limitations concerns the inhomogeneous cell differentiation, located at the structure edges, as observed in the preliminary study [5]. Therefore, to improve the homogeneity of differentiation, one solution could be to apply mechanical stimulation. Several examples of mechanical stimulation-based bioreactors to improve muscle tissue maturation are reported in the literature [106–110].
However, the PCL material initially selected for the support fabrication, due to its stiffness, does not allow mechanical stimulation to be easily applied. Therefore, starting from these results, other linear supports were created us-

ing the molding manufacturing technology and the PDMS, a biocompatible and flexible polymer widely used for TE. First, the supports were manufactured exploiting 3D printed customized molds for the PDMS casting. Then, the PDMS and supports elasticity has been evaluated performing experimental mechanical tensile tests. Finally, the material-specific constitutive parameters, used as material properties in subsequent numerical models, were extracted from the tensile tests experimental data.
Details on the materials chosen and their preparation, on the supports' design and manufacturing, on the tensile experimental tests, and on the material constitutive parameters extraction are reported in the following Sections 2.2.1, 2.2.2.
The methods and results presented below pertain to the study published in 2024 [111].

2.2.1 From the design to molding

Polydimethylsiloxane

In recent decades, PDMS has emerged as one of the materials of main interest thanks to its advantageous properties which are useful in a large number of fields of application, such as TE [112]. PDMS is a silicone-based biocompatible polymer that offers good thermal stability, ease of processing, flexibility and elasticity, optical transparency, gas permeability, and resistance to contamination [113, 114]. The most commonly used commercially available version is Sylgard 184, which consists of a silicone base and a light-sensitive curing agent [112]. By mixing the pre-polymer with the hardening agent, the polymer chains and the cross-linking reaction are activated, transforming the material from liquid to solid. The curing time depends on the temperature, which is an important factor to control as it influences the speed of the polymerization reaction [115]. The structure and mechanical properties of the elastomer are highly influenced by the reaction ratio. Therefore, over the years many studies have evaluated the effect of different mixing ratios of the two constituent substances to try to improve the properties of this material.

In this study, PDMS Sylgard 184 was selected for fabricating supports due to its elasticity and its ability to be autoclaved which made it suitable for stretching application and biological experiments, respectively. In detail, we mixed the polymer base and the curing agent with a ratio of 1:10 as it has already been used in previous cell culture studies [113, 116].

Support design and molding

Based on our preliminary results [5, 6], supports were designed as linear geometries (20 mm length) with a central channel (0.93 mm width) in which the bioink will be deposited (Figure 2.5). As mentioned in Section 2.2 we selected the PDMS for the fabrication of stretchable supports. This material, most of the time, is processed through molding techniques. For this reason, customized molds were designed with Autodesk Inventor® and printed using two different AM techniques: an FDM 3D printer with the Nylon/Polyamide 6 (PA6) material and an HP MultiJet Fusion 580 Color with the Nylon/Polyamide 12 (PA12) material. Then, PDMS was cast inside the mold, left to cross-link for about 24 hours at 60 °C, and subsequently the samples were manually extracted from the molds. Based on the curing temperature, the PA6 and PA12 materials were chosen for the construction of the molds as they resist temperatures above 60 °C (melting point at 220 °C and 180 °C for PA6 and PA12, respectively). Of the two materials, PA6 was selected as PA12 did not allow the perfect PDMS curing, probably due to the high surface roughness cause by the used powder-based 3D printing strategy.

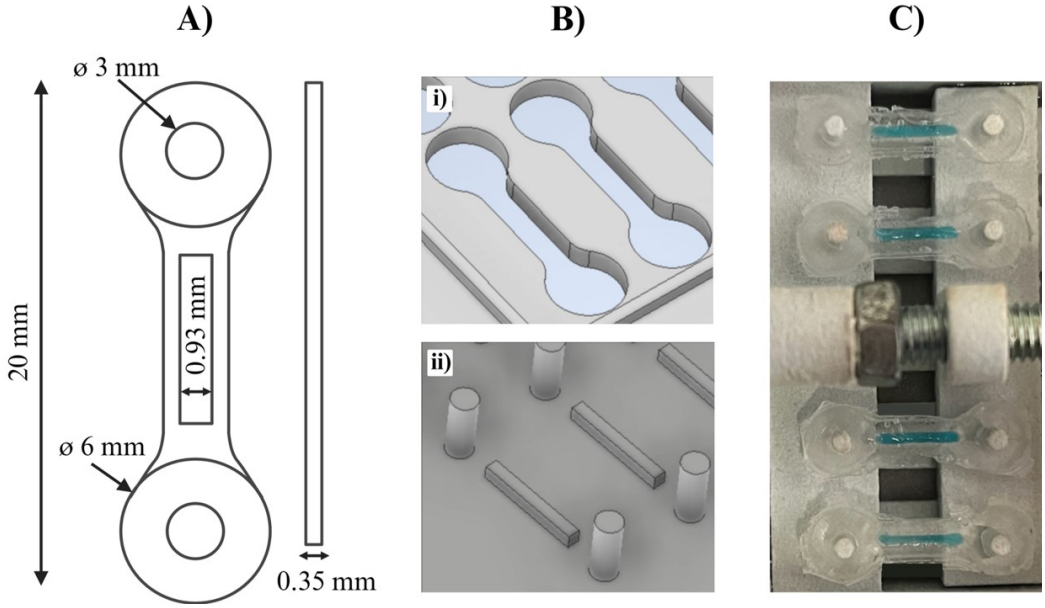

Figure 2.5: Supports design and molding. A) Support geometry. B) Mold used for the production of supports consisting of two parts: i) upper and ii) lower plate. C) Supports manufactured with molding technique.

2.2.2 Mechanical characterization of PDMS and supports

Uniaxial tensile test

In order to investigate the mechanical properties of our supports, we first characterized the PDMS by performing uniaxial tensile tests following the standard ASTM D412 [112] for tensile testing of rubber and elastomeric materials. We designed with Autodesk Inventor® specific molds to obtain PDMS sample with geometrical features in accordance with the standard ASTM, then the molds were 3D printed using an FDM printer and PLA material. PDMS was cast inside the mold and left to cross-link for about 24 hours at 60 °C. Then, PDMS samples were extracted and tensile tests were performed (Figure 2.6). Crosshead speed was set at 2 mm/min and tests ended with the samples breaking [117]. From the resulting curves (n=5), we extracted the average one, and we fitted it in order to obtain the coefficients of the hyperelastic constitutive model of our material used for the subsequent computational simulations. The same mechanical tests (2 mm/min until sample rupture) were carried out for the stretchable supports (n=8) and we calculated the average values for then compared them with numerical results. Before starting the test, width, length, and thickness of each sample were measured using a digital caliper. Applied force and corresponding displacement were simultaneously recorded. Only structures that failed in the central portion were considered.

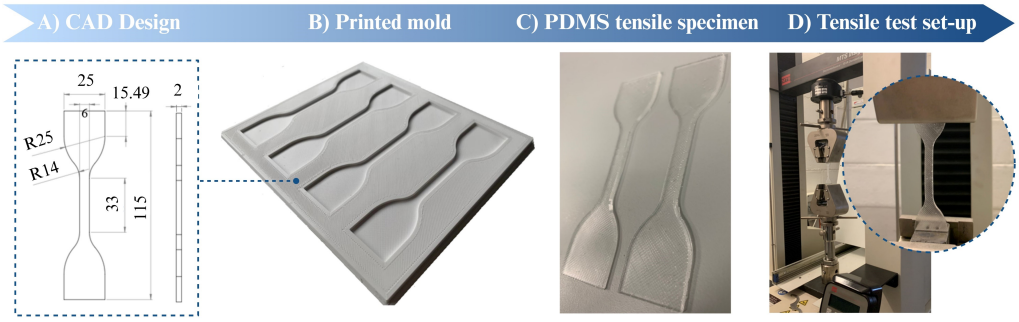

Figure 2.6: PDMS mechanical characterization. A) CAD design of the mold to obtain the samples sized in accordance with the ASTM D412 standard. B) Mold printed in PLA using a FDM 3D printer. C) Fabrication of the PDMS tensile specimens. D) Set-up for tensile testing: samples positioned between the testing machine grips.

All the mechanical tests were performed using a MTS Insight 30 Electromechanical Testing System (MTS System Corporation, United States), equipped with a 10 kN load cell while fitting was performed using Abaqus software.

Data elaboration

Data were elaborated according to a previous study published by our group [118]. The force-displacement curve was spline-fitted using a least squares approach.
The equivalent Young's modulus (E) was calculated as follows: the nominal stress (σ) was calculated as the ratio of the applied force (F) to the sample area (A), while the strain (ε) was calculated as the ratio between the dimensional change (ΔL) and the initial sample length (L0).
The mean force-displacement and stress-strain curves were calculated by averaging the force-displacement and stress-strain curve of each support, five and eight samples for the PDMS and supports group, respectively.

Data processing

The results of the experimental tests were processed and then, to extract from them, the PDMS constitutive parameters, the property module of the ABAQUS/CAE software v2020 (Dassault Systems, France) was used. In detail, a hyperelastic material has been defined and the average experimental stress-strain curve has been loaded into the Uniaxial stress data section. Then, the evaluation of the material was performed by selecting the strain energy potentials of interest (i.e., Ogden, Mooney-Rivlin, Neo-Hookean, Yeoh, Arruda-Boyce, Van der Waals).

Results of the characterization and constitutive parameters extraction

Force-displacement average curve obtained from PDMS uniaxial tensile test and from the Abaqus fitting are illustrated in Figure 2.7. As a result of the experimental study, the stress-strain curves show trends and values of the mechanical behavior of PDMS consistent with the literature [138, 139].
A comparison between the data obtained in this work and those of other articles published in the literature is reported in Appendix A.2.4. However, in all the analyzed articles different process parameters were used, resulting in a less effective comparison. The outcome of the mechanical test is strongly influenced by the set process parameters including the PDMS and curing agent ratio, the curing time and temperature, the sample geometry, the tensile test

speed, and the standard used for the mechanical characterization.
Furthermore, all the hyperelastic constitutive models evaluated are able to optimally fit the experimental curve. Tables in Appendix A.2.5 reported the estimated parameters.

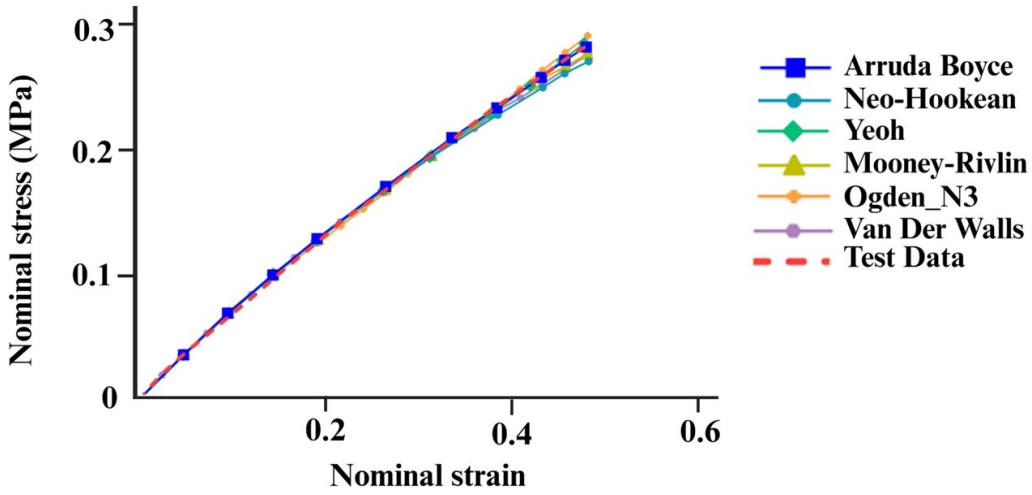

Figure 2.7: Results of the PDMS constitutive parameters extraction

Regarding the experimental characterization of the supports, data are shown in the Figure 2.8. Results showed that to generate a support elongation of 4 mm the force to be applied is approximately 1.68 ± 0.36 N. The value of 4 mm was considered as a reference on the basis of previous mechanological studies present in the literature. In previous studies percentages of 10% [76, 80, 81], 12% [119], 15% [75, 82] up to a maximum of 20% [77] had been applied compared to the initial length of the stimulating membranes. Therefore, the maximum displacement that is expected to be applied via the bioreactor corresponds to 20% of the total length of the support, i.e., 4 mm.
Furthermore, in this case, since it is a specific and non-standard geometry, we cannot compare the curve trends with other literature studies; however the plot show a certain dispersion between the 8 samples' curves.

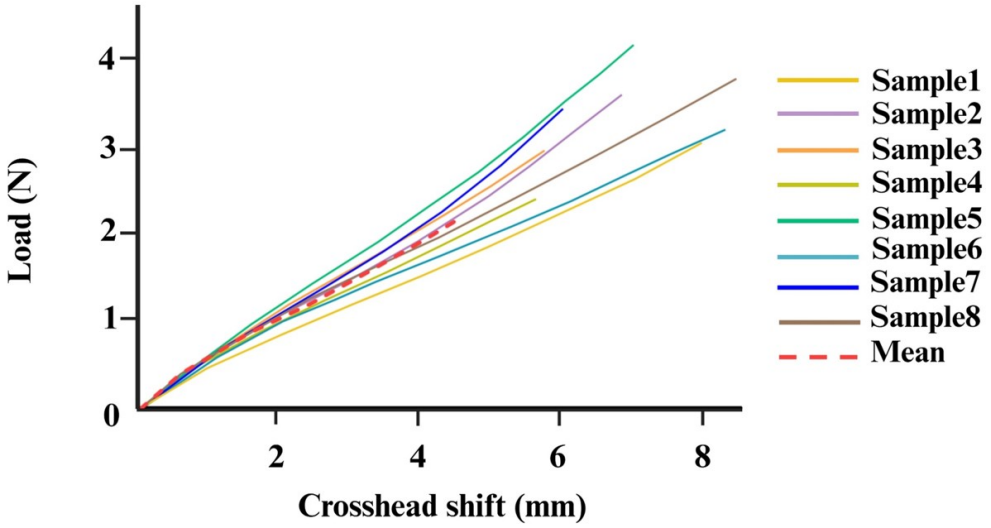

Figure 2.8: Results of the stretchable supports (N=8) mechanical characterization.

2.3 Discussion, Limitations, and Conclusions

Regarding the support design, PCL, a particularly stiff material, was replaced with PDMS, a more elastic and less rigid material. However, the possible influence of substrate stiffness on cell behavior has not been investigated. Furthermore, no mechanical characterization of PCL has been performed. These aspects will need to be explored in depth in future developments of this work. Furthermore, one of the main observed limitations concerns the inhomogeneous cell differentiation, located at the structure edges, probably both because structure edges are the areas where the stiffness and the cross-linking effect are greater and because cells need oxygen/nutrients and so they move to peripheral areas where the oxygen/nutrients concentration is higher. In this regard, the stiffness of the hydrogel is an aspect that will certainly have to be considered and explored in future studies, as it could have a significant impact on cell distribution and migration. Finally, concerning the mechanical PDMS supports characterization, the number of samples used for the mechanical tests should be increased to limit the experimental data's variability and consolidate the statistical data. Furthermore, it would be useful to complete the characterization of the PDMS material through confined compression tests.

Chapter 3

Design and development (2): mechanical platform

Bioreactor design and the way physical stimuli are applied are closely connected and, for this reason, have to be well studied together to enhance the positive effects on cells under specific conditions [120, 121]. To aid device design and the connected stimulation, a powerful tool is represented by computational simulations. Widely utilized in different fields of industry (e.g., automation) and research (e.g., cardiovascular stent design), computational simulations have been recently adopted in the field of TE. Particularly, these tools are employed to optimize bioreactor design, both in terms of shape and function, to avoid approaches of trial-and-error, which are characterized by useless and iterative steps of experimental tests with associated cost and time waste. Indeed, the key value of computational simulations is the ability to modify and study the effects of bioreactor design with respect to one, more, or combined inputs and by changing their values, without having to build actual physical models, or to run a large number of experimental tests.
For these reasons, it is extremely useful to support the design phase of the bioreactor development process by exploiting the computational tools that allow the optimization and ad-hoc design of the device.

In this chapter, an experimentally validated computational framework to support the design of a mechanical platform is presented. To this aim, a Structural Finite Element Analysis (FEA) of the supports and platform under tension, comparing the numerical results with corresponding experimental data was performed. Then, the cyclic platform prototype and the validation of a connected proof-of-concept sensor with data transmission on the Cloud are presented.

3.1 Numerical model calibration: structural FEA of the supports stretching

FEA was first used to optimize the mechanical stretch apply by our mechanical platform and to predict the structural mechanical properties of the supports; therefore, the uniaxial tensile test described in Section 2.2.2 was simulated using ABAQUS/CAE software v2020 (Dassault Systems, France). Subsequently, the FEA results have been compared with the experimental data as validation steps.

3.1.1 From CAD to FEA mesh

To create a high-fidelity model of the support suitable for FEA, the CAD model of the specimens was designed by Autodesk Inventor on the basis of the measurements taken by caliper from the real samples tested experimentally in Section 2.2.2. The geometry was then imported in ABAQUS/CAE as a geometrical part of the model.
The structure exhibits geometric symmetry, but it is non-structural because the load is applied unidirectionally rather than bidirectionally. As a result, only half of the structure was analyzed using FEA (Figure 3.1A). This approach was taken to reduce and optimize calculation times. Furthermore, a geometry partition was then performed to allow the generation of high-quality mesh (Figure 3.1A). A mesh with global seed 0.4 was used (Figure 3.1B). The C3D8RH elements of Hex shape, integrated in a reduced way and of linear geometric order, were obtained with the sweep technique guaranteeing at least 3 elements in the thickness.

3.1.2 Material properties

PDMS was modelled as an hyperelastic isotropic material. The specific constitutive coefficients obtained in Section 2.2.2 and reported in Tables in the Appendix Section A.2.5 have been assigned to the PDMS. All the different fitted hyperelastic models were implemented and compared.

3.1.3 Interactions and boundary conditions

The simulation of the support traction requires the modelling of the contact between the grips of the testing machine and the support ends. To this aim, the following interactions were implemented: an MPC constraint has been defined that linked the central reference/control point of the samples

hole to all the slave geometry, i.e., all the geometry stretched by the testing machine grip (Figure 3.1C); a null displacement was assigned to the specimen lower surface which during the test is held by the machine fixed grip (Figure 3.1D); symmetry along the X axis taking into account the partition applied at the beginning to simplify the model (Figure 3.1D); application of the displacement at the control point of 4 mm along Z (Figure 3.1D). The value of 4 mm has been set as it is not expected to apply a greater displacement inside the bioreactor (20% of the total length of the support)[77], as mentioned in paragraph 2.2.2.

3.1.4 Analysis setup

Being a particularly slow event, that of traction (2 mm/min), a Static analysis was computed using an implicit solver (ABAQUS/Standard, Dassault Systemes, France). Simulations were run using an Intel Core(TM) i7-12700H desktop (3.5 GHz, 16GB RAM).

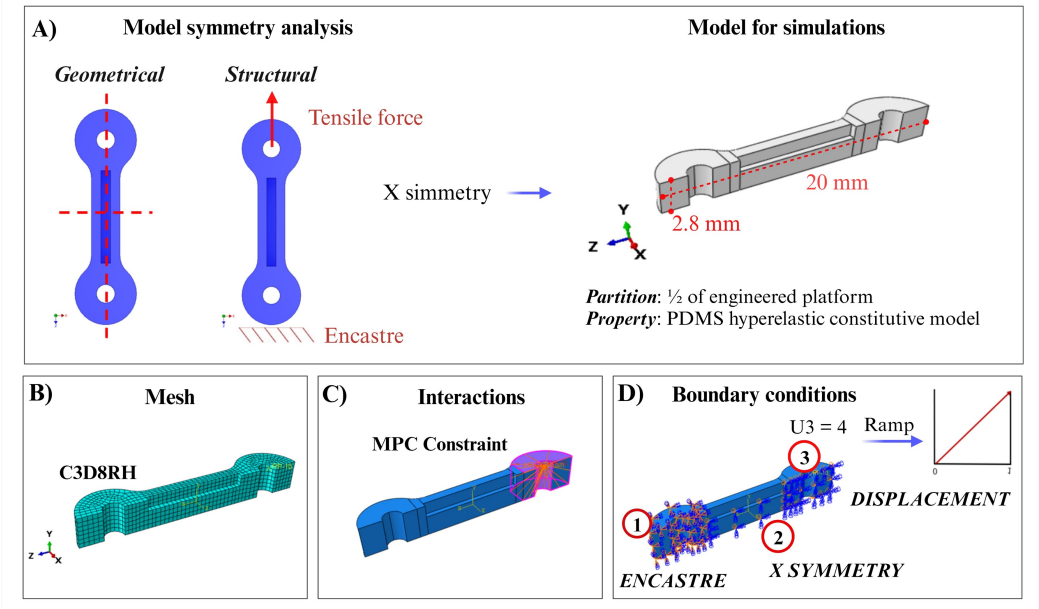

Figure 3.1: Numerical model: structural FEA of the supports stretching. A) Analysis of the geometry symmetries and definition of the model for the simulation (partitioning and material properties). B) Mesh creation. C) Definition of the model interactions. D) Boundary conditions imposed for the simulation.

3.1.5 Data validation and processing

Experimental results obtained from the experimental tensile tests of supports (Section 2.2.2) were used for validating the FEA model. Both experimental and calculated with the FEA force-displacement curves were processed to calculate stiffness (K). The mechanical behavior of the supports were studied in the linear regime. To identify this region, the derivative of the force-displacement curve is computed over the full range of displacement; the limit of the elastic region is then defined as the point where the derivative begins to decrease. K was calculated for all supports, experimental and numerical, as the maximum derivative calculated in the linear region. Finally, the numerical and experimental results were compared to validate the model.

3.1.6 Results of numerical study and comparison between experimental and numerical data

As described in Section 2.2.2, PDMS supports were fabricated and mechanically characterized. In the computational model, the PDMS supports tensile tests were simulated for each previously fitted constitutive model (Section 2.2.2). Experimental and numerical curves were compared. The computational model has been validated; in fact, a good correspondence between experimental and numerical curves is shown in Figure 3.2. Furthermore, by calculating the stiffness K, it can be seen that the constitutive model most similar to the experimental case is that of Ogden (Table A.9). Considering the Ogden computational results, we obtained that if we want to stretch our structure up to a maximum of 4 mm, the force that the bioreactor will have to apply will be approximately equal to 1.6 N.

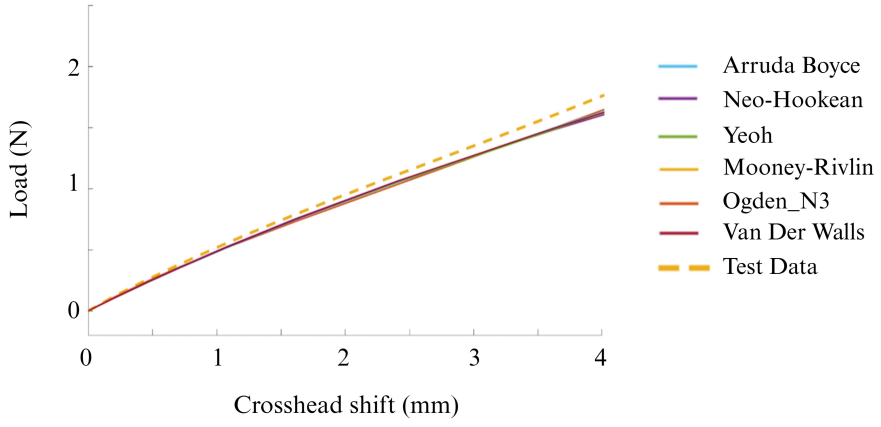

Figure 3.2: Comparison between experimental and numerical results.

3.2 Mechanical platform design supported with the calibrated structural FEA

For the development of the mechanical platform, we worked on designing prototypes capable of stimulating multiple samples simultaneously in a high-throughput mode. In particular, a number of samples equal to at least three were taken into consideration as the triplicate is the minimum value required in case of biological experiments.
Initially, the platform was developed to impose a static mechanical stimulation applied via a stimulation system consisting of a hexagon head screw and activated via an Allen key (SECCARO cylindrical head screw M5 x 30 mm). Another property of the proposed platform was that of being a cellular chamber suitable for long-term cell culture, defined as a "Smart Petri Dish" (SPD), consisting of a small box with a lid inside which the stimulation mechanism is inserted. The device is designed to be modular, so all the components are separable (Figure 3.3): 1) small box with pins at the corners for interlocking the mechanism; 2) fixed part of the mechanism that fits into the box; 3) mobile part of the mechanism that fits on the fixed one; 4) screw with hexagonal head that can be stimulated with an Allen key; 5) lid. The modularity allows to replace only the necessary component in case of problems and to guarantee excellent cleaning and sterilization, essential for cellular experimentation. The stimulation, for this prototype, as mentioned, is a static one and using an Allen key we are able to impose a known stretch thanks to the references printed on the sides of the cellular chamber (Figure 3.3).
In order to reduce as much as possible the trial-and-error aspect and therefore the number of prints and the experimental time, the mechanical platform design has been optimized through computational techniques. Two versions of the platform were designed using Autodesk Inventor CAD software and studied numerically using ABAQUS software as described in detail in Section 3.2.1. In the first version of the platform, the screw-based actuation mechanism was placed on one side and three samples were placed on the opposite side. The second version was designed with the screw-based stimulation mechanism positioned in the center of the cell chamber and four samples positioned two to the right and two to the left (Figure 3.4).
To validate the numerical results, the SPD prototypes were printed using PA12 with the HP MultiJet Fusion 580 Color printer. PA12 was chosen for its autoclave suitability, as it has a melting point of 220 °C and the autoclave operates at 140 °C. Additionally, the MultiJet Fusion printing technique ensures excellent resolution, which is essential for creating our cellular chamber.

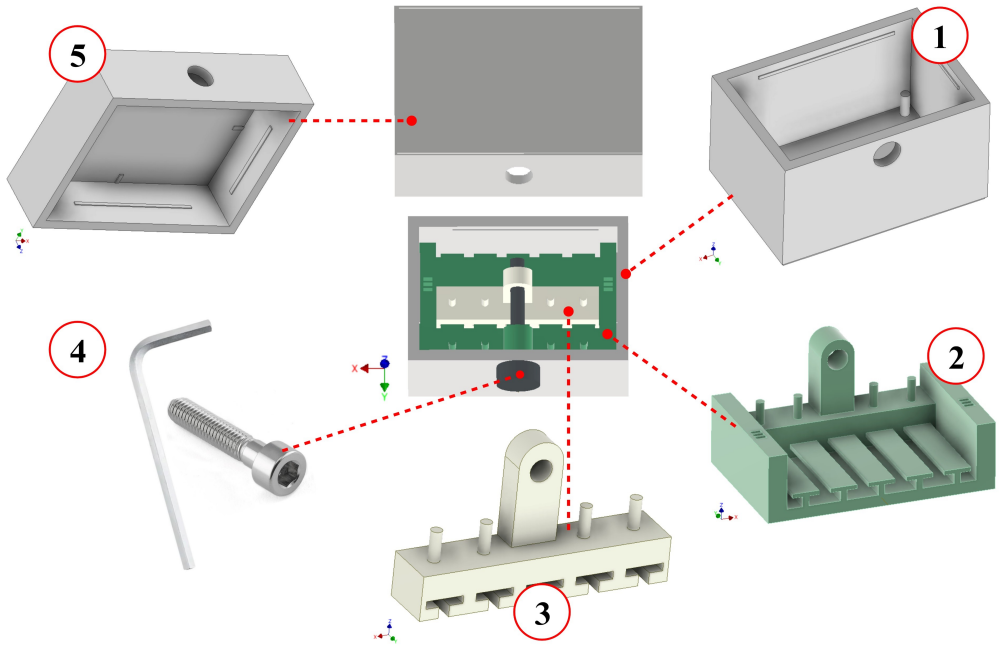

Figure 3.3: Mechanical platform design. The device is designed to be modular with all the components separable: 1) small box (60.4 x 41.4 x 33 mm) with pins at the corners for interlocking the mechanism; 2) fixed part of the mechanism that fits into the box; 3) mobile part that fits on the fixed one; 4) screw with hexagonal head that can be stimulated with an Allen key; 5) lid. All parts were printed in PA12 and HP MultiJet Fusion 580 Color technology except the commercially purchased stainless steel screw (SECCARO cylindrical head screw M5 x 30 mm).

3.2.1 Numerical model: structural FEA of the mechanical platform

Structural FEA was used to optimize the design of our cellular chamber and to predict its structural behavior after the stretching application; therefore, the cell chamber-imposed stretch was simulated using ABAQUS/CAE v2020 software (Dassault Systems, France). Subsequently, the FEA results were compared with the experimental data as validation steps.

From CAD to FEA mesh

The CAD model of the two platform prototypes and of the PDMS supports were imported in ABAQUS/CAE as a geometrical part of the model. In total, our models consists of three parts: 1) PDMS samples; 2) mobile

part of the device; 3) fixed part of the device. In the assembly module the different components have been arranged in their correct working position. The different parts were translated and rotated in the 'Assembly' Section to create the whole CAD model.
Due to the geometric and structural non-symmetry, in the case of the first version of the platform the whole structure was analyzed by the FEM (Figure 3.4A), while in the case of the second prototype, thanks to the geometric and structural symmetry, only half of the structure was analyzed by the FEM following a partition (Figure 3.4B), in order to reduce and optimize the computational cost. Furthermore, in both cases a partition of the geometries, both of the supports and of the components of the cell chamber, was performed to allow the generation of high quality meshes. Regarding the mesh, for PDMS supports the same properties reported in Section 3.1.1 were defined, instead, for the platform, a mesh convergence analysis was performed. The mobile and fixed parts were discretized by linear hexahedral structured reduced elements (element type C3D8R) (Figure 3.4A-i and B-i). Next, convergence analysis was performed considering three different mesh sizes: coarse, medium, and fine (Figure 3.4A-i). The total number of elements of the FEA model (supports and bioreactor) is 7361, 25332, and 118869 for coarse, medium, and fine mesh sizes, respectively.

Material properties

In the property module, we defined two different materials, PDMS for the stretchable supports and PA12 for the mechanical platform. PDMS was modelled as an hyperelastic isotropic material using the constitutive parameters fitted with the Ogden model (Table A.4), which is the one selected in Section 3.1.6. Furthermore, as reported in Table 3.1, mass density and Poisson's ratio were set at 965 Kg/m^3 [122] and 0.45 for PDMS [123] and 1020 Kg/m^3 [124] and 0.39 [125] for PA12. Finally, for PA12 a Young's modulus of 1650 MPa [126] was set.

Table 3.1: PA12 and PDMS properties set into FEA model. Values are from literature [122–126].

Material	Mass density [Kg/m^3]	Poisson's ratio	Young's modulus [MPa]
PA12	1020	0.39	1650 MPa
PDMS	965	0.45	-

Interactions and boundary conditions

The simulation of the support traction imposed by the mechanical platform requires the implementation of the following interactions (Figure 3.4A-ii, iii and B-ii, iii): an MPC constraint has been defined that linked the central reference/control point of the mobile part hole to all the slave geometry, i.e., all the hole internal surface; a general contact for all surfaces with a frictionless tangential behavior is defined as we have three parts in the assembly; a null displacement was assigned to the lower surface of the platform fixed part; application of the displacement at the control point of 4 mm along X. The value of 4 mm has been set as it is not expected to apply a greater displacement inside the platform (20% of the total length of the support)[77].

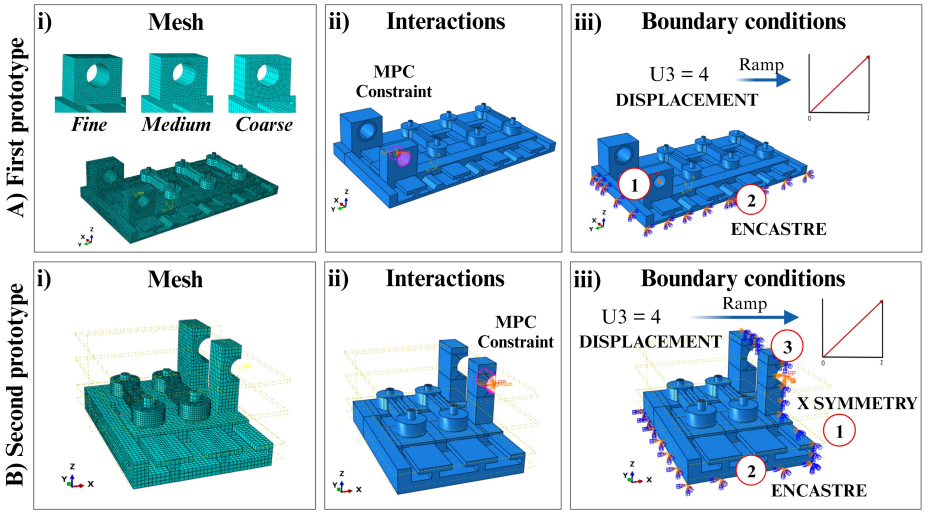

Figure 3.4: Numerical model: structural FEA of the mechanical platform. A) First and B) second prototype. i) Mesh creation. ii) Definition of the model interactions. iii) Boundary conditions imposed for the simulation.

Analysis setup

Being a particularly slow event, that of manual traction, a Static analysis was computed using an implicit solver (ABAQUS/Standard, Dassault Systemes, France). Consequently, a preliminary sensitivity analysis was performed to assess the time step impact on the inertial forces. A single time step equal to 6 sec was studied, which corresponds to the time interval necessary to manually stretch the constructs for about 4 mm. To verify that the analysis was effectively quasi-static, the ratio between kinetic energy (ALLKE) and internal energy (ALLIE) was monitored during the analysis. Simulations were run using an Intel Core(TM) i7-12700H desktop (3.5 GHz, 16GB RAM).

Data validation and processing

The two versions of the platform simulated at the FEA were 3D printed for the model validation. The two prototypes were printed in Nylon PA12 and with HP Multijet fusion printing technology as described in Section 3.2. Finally, the numerical and printed structures behaviors were compared to validate the model.

Results of numerical study

First, the model parameters, time step, and mesh size, were optimized, considering the first version of the bioreactor. Specifically, the quasi-staticity of the analysis was verified in the case of the time step equal to 6 sec. Then, the mesh size associated with the platform was varied to set up the FEA model. For the considered time step, the kinetic energy showed to be less than 5% of the internal energy, confirming the quasi-staticity of the analysis (Figure A.3A).
Once the time step was verified, three meshes were considered: coarse, medium, and fine. To verify the influence of the mesh size, the stretching over time of the sample positioned closest to the stimulation mechanism was monitored. The displacement-time curves simulated by varying the mesh size showed that as the mesh size increased, the calculated displacement increased (Figure A.3B). Furthermore, the curves related to fine and medium mesh were very similar to each other. Based on these results, considering the result's precision (Figure A.3B) and the calculation times (Table A.10), the medium mesh size was chosen as a compromise.
Once the parameters of the FEA model were set, the behaviors of the two platforms prototypes were simulated and then compared. The first prototype

(one-side) showed the flexion of the mobile part when the movement was imposed causing an inhomogeneous stretching of the supports (Figure 3.5A-i), while the optimized prototype with the central mechanism showed a homogeneous stretch of the samples without the flexion of the mobile part (Figure 3.5B-i). About the first prototype, we hypothesized that the flexion of the mobile part was connected to the 0.2 mm tolerance placed between all the parts in contact as the prototypes had to be made with 3D printing. Thus, a further test considering the same geometry without the tolerance was analysed. This third configuration show that, as we hypnotized, removing the tolerance, the flexion disappear and the sample are stretch homogeneously (Figure A.3C).

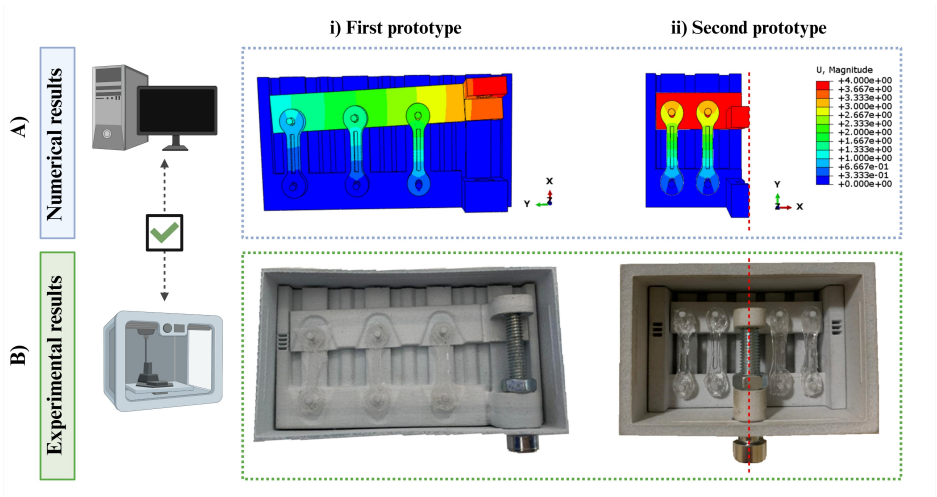

Figure 3.5: Comparison between experimental and numerical results. A) Numerical displacement distribution and B) experimental behavior of the printed mechanical platform after the application of a 4 mm stretch. i) First and ii) second prototype of the mechanical platform.

Comparison between experimental and numerical data

First and second configuration of the platform (one-side and central) were 3D printed and the displacement of 4 mm was applied. The experimental and numerical behavior of the two configurations were compared. A good correspondence between experimental and numerical behaviors is shown in Figure 3.5 since the first platform prototype, as mentioned in Section 2.2.2, shows a flexion of the mobile part causing an inhomogeneous stretch of the supports confirmed also by the simulation. Furthermore, considering the second prototype, both the experimental and the numerical behaviors show the

homogeneous stretch of the samples and also the absence of the mobile part flexion (Figure 3.5B-ii).

After this semi-quantitative validation, we subsequently defined a set-up to quantitatively validate the model, focusing on the measurement of the stretch imposed on the supports and on the gel deposited in the central channel. Details will be reported in the Chapter 4.

3.3 Design and fabrication of a cyclic mechanism with Cloud-connected sensors

Since the importance of mechanical stimuli is well known in the literature when applied especially in cyclic mode to muscle cells culture, as a next step we developed a prototype mechanical platform capable of providing cyclic mechanical stimulation.
Furthermore, as mentioned in Section 1.2, since bioreactors can perform several tasks in addition to providing physical stimuli such as monitoring the cell culture environment, a temperature and humidity sensor, as a proof-of-concept, was implemented and connected to a Cloud platform in our prototype.

3.3.1 CAD Design and fabrication

The cyclic platform prototype is designed to be modular and made up of a set of sub-parts (Figure 3.6A).

1. The cell culture chamber which include multiple SPDs.

2. The actuation part which include stepper motors connected to an endless screw.

3. The electronic control part based on an Arduino microcontroller circuit.

Regarding the cell chamber, a tray with slots in which the SPDs are placed and blocked during the culture period is designed. For the actuation part, it is design a geometry which included holes for the exit of the threaded rods connected to the stepper motors and for the motor power cables. A further component of this part is the lid which has been sealed using four screws. Concerning the last third part, so the electronic control one, a geometry is designed to contain and place the electronic components inside. Also in this

case, holes have been made for the exit of the general and motors power supply cables, and furthermore, this too was closed with a lid and four screws. This part is meant to be placed outside the incubator, while parts 1 and 2 are designed to be placed inside. This choice because the third part contains electronic components which would certainly be affected by the environment inside the incubator, i.e., heat and above all very high humidity. All the screws used in the prototype are made of stainless steel to ensure their prolonged use in the humid environment of the incubator.

All the components of the cyclic platform prototype were designed using Autodesk Inventor and then 3D printed using a commercial FDM printer (ANYCUBIC Kobra Go Max Professional 3D Printer) and PLA material (ANYCUBIC PLA Filament 1.75 mm) (Figure 3.6B).

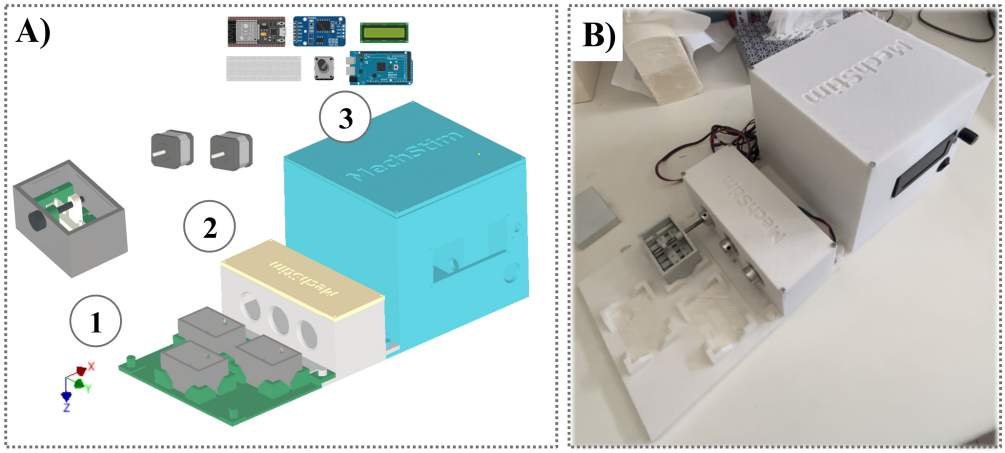

Figure 3.6: CAD Design and fabrication of the cyclic mechanical platform prototype. A) Platform schematization composed by three principal parts: 1) cell culture chamber which include multiple SPDs; 2) the actuation part which include stepper motors connected to an endless screw; 3) the electronic control part based on an Arduino microcontroller circuit. B) 3D printed cyclic mechanical platform prototype. All the components were 3D printed using a commercial FDM printer and PLA material.

3.3.2 Electrical circuit and Cloud connection

For the control of the actuation system, we designed an electric circuit based on the Arduino MEGA Rev3 microcontroller. The electronic components were implemented on breadboards (AZDelivery MB-102 Breadboard

Basette); among the electronic components, an LCD display (IIC I2C Serial LCD Screen 2004 20X4 Display Module), a rotary encoder (DIFCUL Rotary Encoder Module, KY-040 360), stepper motors (Redrex High Torque Nema 17 Stepper Motor 1.5A 40Ncm/57) with their respective control drivers (Longruner A4988 Stepstick stepper Motor driver module), a clock (AZDelivery Real Time Clock RTC), an on/off button (Gebildet 6A/250V 10A/125VAC SPST 2Pins), and a power supply card (AZDeliveryPower Supply Adapter Module), a temperature-humidity sensor (AZDelivery KY-015 DHT11), and a Wi-Fi card (AZDelivery ESP32 NodeMCU WiFi Development Board CP2102) have been implemented.
In addition to designing the hardware part of the circuit, we write the control software using the Arduino App. In particular, a menu has been implemented that can be viewed via an LCD display and with the following items selectable via a rotary encoder.

- "STATUS SCREEN" which allows to view the output of the clock (i.e., date and time).
- "TEMP/HUMIDITY" which allows to view the instantaneous output values of the temperature humidity sensor.
- "BIOREACTOR PROTOCOL" which starts the clockwise and counterclockwise rotation of the stepper motors based on the data entered in the software.

Once the software was written, it was loaded onto the card Arduino MEGA via USB port.
Furthermore, the temperature-humidity sensor, to be easily monitored, was connected to the Arduino IoT Cloud platform via the Wi-Fi card. To this end, a Dashboard was created within the platform and then different widgets associated with the sensor output variables were selected within the Dashboard. Specifically, gauge and percentage widgets have been used to monitor the temperature and humidity respectively, and the chart widget has also been used to view the trends of the two quantities over time by adding every 15 seconds the output sensor value and then connecting the various points via spline. This Arduino IoT Cloud platform allows monitoring not only from a PC but also from a mobile phone via App.

3.3.3 Cloud validation: proof-of-concept

The temperature-humidity sensor, as mentioned, has been implemented as a proof-of-concept for verifying the functioning of the first sensorized cyclic

bioreactor prototype as it is easy to validate using the known temperature indicated by the culture incubators (Figure 3.7).
For the validation of the sensor, only the third part of the cyclic platform prototype was exploited. The part was placed next to and outside a cell culture incubator. The circuit was connected to the power supply and turned on by the power button, the Wi-Fi board automatically connected to the pre-defined, at the software level, Wi-Fi network, the Dashboard on the Arduino IoT Cloud was opened to monitor the sensor output, and finally the temperature-humidity sensor was inserted inside the incubator.
The results showed that as soon as the sensor was inserted into the incubator the temperature and humidity values started to increase until reaching a plateau value (Figure 3.7A). Specifically, the initial humidity and temperature monitored in the external environment of the laboratory was equal to 39% and 20 °C and finally reached a value of 74% and 36 °C, respectively. The temperature recorded by the cell incubator was equal to 36.9 °C, as can be seen in Figure 3.7B, so our sensor has an estimation error 2.7% compared to the target value.

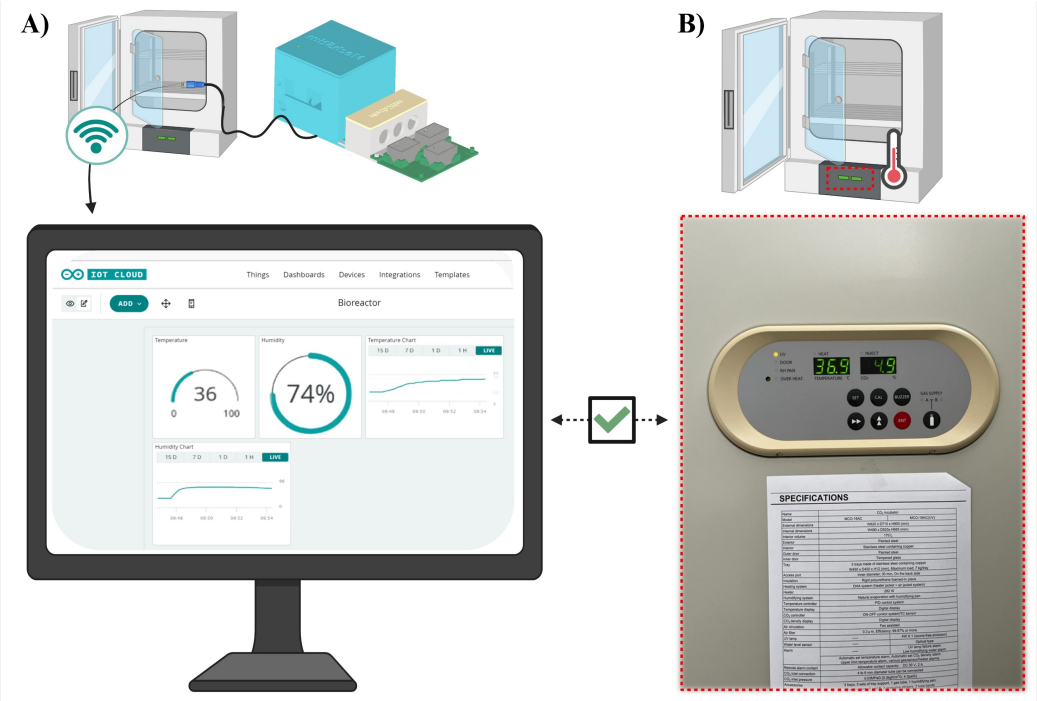

Figure 3.7: Cloud validation: proof-of-concept. A) Cloud monitoring of the output data of the temperature-humidity sensor inserted inside the incubator. B) Correct temperature output value indicated by the incubator.

3.4 Discussion, Limitations, and Conclusions

The reliability of the device should be improved through the implementation of better quality sensors, electronic components, motors. Furthermore, the cyclic mechanical platform was tested by evaluating a single type of actuation based on stepper motors; in order to demonstrate its translationality it will have to be adapted also to other types of stimulation, such as the use of different motors (for example brushless motors, pneumatic motors) or, as we are currently studying in the laboratory, the use of shape memory alloy wires for actuation applications. The latter approach could reduce the limitation linked to noise and above all to the vibrations produced by the rotation of the motors.
Finally, regarding PA12, the material selected for the platform prototypes, has shown to be a material capable of withstanding autoclave cycles, ensuring the device sterilization. However, it is necessary to study the durability and the effect of multiple wet heat treatments on its mechanical properties. Furthermore, the SPDs placed inside the culture chamber should be made using transparent materials to allow visual monitoring of the structures inside. The possible materials we have identified for this purpose are Formlab dental resin and Stratasys MED610 material. Dental resin is an autoclavable and biocompatible resin for applications including 3D printing of dental surgical guides for implant placement. This resin was specially formulated for Formlabs printers and rigorously tested to meet solvent disinfection and autoclaving standards for implant systems. The biocompatible Clear MED610^{TM} is instead a rigid and transparent dental resin characterized by high dimensional stability intended for printing surgical guides and removing partial denture casting models.
The first resin has already been applied for the construction of a perfusion bioreactor with excellent results [68].

Chapter 4

Testing and benchmarking of the mechanical platform

As a final step we carried out the mandatory validation of the proposed mechanical platform by analyzing the transmission of the mechanical stimulation from the stretchable support to the 3D construct, the integration of the BioP on the platform, the device sterility, and finally the biological effect of the dynamic culture on muscle cells.
The aim of the platform is to transmit to the 3D culture, i.e., to the hydrogel loaded with cells deposited on the PDMS stretchable supports, a stimulus capable of promoting cell differentiation and fusion. For this purpose, the contact PDMS-hydrogel should guarantee the deformation of the latter in order to allow the transmission of the mechanical stimulus to the cells.
However, as known in the literature, these two materials are of a completely different nature; in fact, the hydrophobic characteristics of PDMS and the hydrophilic characteristics of the hydrogel do not favor the interaction between the two materials [127]. Many studies carried out in the past have dealt with the topic of hydrophobicity of PDMS by proposing various methods of surface modification (chemical or coating of the material) in order to impart hydrophilic characteristics to the material [113, 114, 128, 129]. Therefore, it was necessary to address and assess this topic.
Additionally, a crucial requirement for the mechanical platform is to ensure the sterilizability and biocompatibility of its materials so that it can effectively influence the *in-vitro* proliferation and differentiation of cells encapsulated within the hydrogel.
In this context, another problem in the field of the mechanical devices is that of guaranteeing the sterile condition of the cell scaffold: normally 2D membranes on which cells are seeded are used or in the case of 3D cultures,

scaffolds are created separately, for example using molding techniques, and subsequently transferred into the device. However, performing multiple steps increases the likelihood of developing contamination and not ensuring the culture sterility. For this reason, it is extremely useful to integrate the printing process directly within the platform.

This chapter initially presents an experimental set-up to assess the transmission of the mechanical stimulation from the stretchable support to the hydrogel. The experimental set-up consisted in monitoring the displacement of markers positioned inside the hydrogel deposited on the stretchable constructs and subjected to traction. Furthermore, the transmission was also examined numerically by exploiting the previously developed computational model. Subsequently the numerical results were compared with the corresponding experimental data. Once the model was validated, it was exploited to test new geometries, avoiding the experimental trial-and-error approach which is undoubtedly cumbersome, costly, and time-consuming. Therefore, the idea was to generalize the PDMS supports, modifying their structure through the addition of new structural elements, in order to guarantee a more efficient transmission of the deformation from the supports towards the hydrogel and consequently to the cells.
Finally, the chapter presents the sterility assessment of the mechanical platform and subsequently the feasibility study of the integration of the BioP process on the platform under sterile conditions. Thus, the *in-vitro* effect of the application of the mechanical platform on 3D bioprinted construct loaded with C2C12 murine myoblasts is reported. To this aim, cell viability and gene expression analyses were carried out.

The biological studies presented were conducted in collaboration with the group of Prof. Gabriele Ceccarelli (Human Anatomy Department of the University of Pavia).

4.1 Hydrogel stretching assessment

An experimental and computational assessment were proposed to test the transmission of the mechanical stretching from the stretchable supports to the hydrogel deposited on top of them (Figure 4.1).
To test the stretch of the hydrogel deposited on the PDMS supports channel, three different categories of biomaterials were tested and compared:

1. A non-cross-linkable hydrogel (CELLINK START).

2. A chemically cross-linked hydrogel (Gelatin-Chitosan-PEG).

3. An ionically cross-linked hydrogel (Gelatin/Sodium Alginate-based hydrogel cross-linked with $CaCl_2$).

Our hypothesis was that non-cross-linked or chemically cross-linked hydrogels would be stretchable because of their soft consistency after printing; conversely, the ionically cross-linked hydrogels would not be stretchable because the addition of calcium ions makes the alginate structures rigid with excellent shape retention, which is essential for BioP applications in general but not suitable for our application where the elasticity of the gel is required. The elongation of the hydrogel was also assessed using the previously validated numerical model and then the experimental and numerical results were compared.

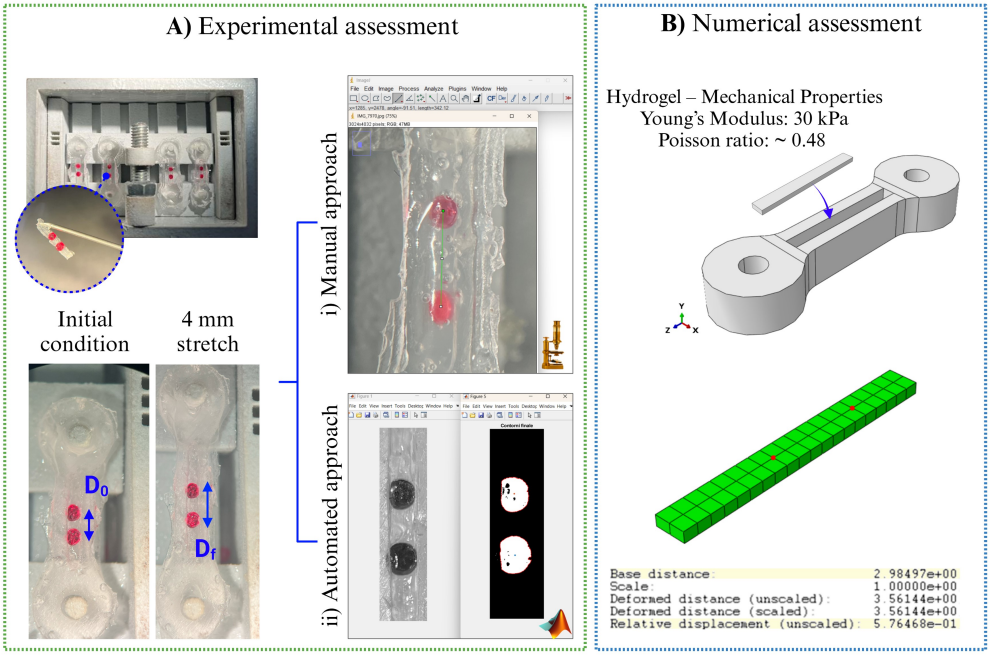

Figure 4.1: Assessment of hydrogel stretching: experimental and numerical approaches. A) Experimental assessment based on PDMS supports within which the hydrogel is extruded and two markers are positioned. Image processing via i) manual and ii) automated approach. B) Numerical assessment with the hydrogel addition to the computational model and the monitoring of the distance between two nodes of the mesh.

Non-cross-linkable hydrogel: CELLINK START

CELLINK START is a commercial non-cross-linkable water-soluble gel often used for preliminary printing tests. It is a biocompatible material which therefore can also be used as a sacrificial material for cell-laden constructs, bioinks with poor shape fidelity, and constructs with porosity along all three axes. CELLINK START prints at room temperature and dissolves easily after washing with culture media, making it an easy-to-use sacrificial material. For this section activity, CELLINK START was chosen because being a non-cross-linkable gel it maintains a particularly soft consistency after printing which we hypothesized could guarantee the stretch of the hydrogel coherently with the PDMS support.
CELLINK START hydrogel was purchased from CELLINK AB (Gothenburg, Sweden).

Chemically cross-linked hydrogel: Gelatin-chitosan-PEG

Gelatin-Chitosan-PEG hydrogel is a new protein-polysaccharide hybrid biomaterial, promising as a bioink, which was developed by the group of Laura Russo (University of Milano Bicocca, Italy) and then characterized in an our previous study [130]. It is based on gelatin (GE) and chitosan (CH) functionalized with methylfuran groups and cross-linked by Diels-Alder cycloaddition with a commercial Star-PEG functionalized with maleimide groups as a dienophile (Star-PEG-MA). Compared to traditional biomaterial inks, the advantages of this functionalized biomaterial include the control of biological and mechanical features by tunable and cell-safe cross-linking. Furthermore, it is well established in the literature that the microenvironment recreated by CH is suitable for cell growth and that GE is a natural polymer that has specific amino-acid residues, such as Arginyl-glycyl-aspartic acid, which is an ECM adhesion sequence. For this reason, CH-GE hybrids are considered promising materials for TE applications.
For this activity section, the GE-CH-PEG hydrogel was chosen because it is a chemically cross-linkable gel, therefore it does not require the addition of external ions, which maintains a particularly soft consistency after printing which we hypothesized could guarantee the elongation of the hydrogel coherently with the PDMS support.

Ionically cross-linked hydrogel: Gelatin/Sodium Alginate

Alginic acid is a biocompatible naturally occurring anionic polymer typically obtained from brown seaweeds. One of its derived salts is Sodium Alginate (SA) used for many biomedical applications [131], including BioP,

thanks to its biocompatibility, low toxicity, and relatively low cost. Alginate is known to be a whole family of linear copolymers containing blocks of (1,4)-linked β-D-mannuronate (M) and α-L-guluronate (G) residues. Generally, alginate is cross-linked using ionic cross-linking agents, such as divalent cations (e.g., Ca^{2+}) [131], to ensure the stability and structural integrity of the hydrogel. Specifically, the α-L-guluronate (G) blocks of the alginate participate in the intermolecular cross-linking with divalent Ca^{2+} cations of CaCl2 to form the so-called "egg-box" model of cross-linking forming crevices where calcium ions are located; the result is a hydrogel network. Furthermore, to improve SA printability and biocompatibility, it is often combined with other biopolymers, such as GE. Thus, in this test an hydrogel composed of 8% (w/v) SA and 4% (w/v) GE was used.
Materials were prepared following protocol optimized in a previous study [132]. In detail, SA powder was dissolved into deionized water (at room temperature) and subsequently mixed until homogenization. Then, also GE powder was added and mixed until homogenization and, finally, the hydrogel was pasteurized for 1 hour at 75 °C for decontamination.
SA and GE powders were purchased from Sigma Aldrich (Milan, Italy) while $CaCl_2$-based solution was purchased from CELLINK AB (Gothenburg, Sweden). For this experiment, the SA/GE-based hydrogel was cross-linked in two different ways:

1. With Cellink's $CaCl_2$ solution for 5 minutes.

2. With the Cellink's $CaCl_2$ solution diluted 1:2 with PBS for 5 minutes.

This choice, as the less cross-linked gel maintains a softer consistency that we hypothesized could guarantee the elongation of the hydrogel coherently with the PDMS support.

4.1.1 Experimental assessment

The experimental assessment of the hydrogel stretch was carried out thanks to the definition of a specific set-up. This experimental set-up first involved the extrusion (also manual) of the hydrogel inside the central channel of the PDMS support and then the placement, approximately in the same position, of two circular red markers with a diameter of about 1 mm. The markers were embedded in the gel and not positioned on the PDMS support as we demonstrated with the alginate-based hydrogel (Figure 4.1A). For the observation of the samples, two main laboratory equipment were used: a PHOTONIC PL 2000 light source and a Nikon type 2 microscope with which

it was possible to provide the correct illumination and the correct magnification to view gel and markers positioned in the PDMS support channel.
Photos for each sample were acquired both in the initial condition and following the application of the 4 mm stretch. The image processing was then carried out using both a manual approach with ImageJ software and a automatized approach with a MATLAB code specifically developed for this purpose (Figure 4.1A, Appendix A.4.1).
The initial distance (D_0) and the post-stretch distance (D_f) between the markers' centers was measured, and finally the percentage of stretch was calculated as described by the following equation.

$$\%hydrogel\_stretch = \frac{D_f - D_0}{D_0} * 100 \tag{4.1}$$

The MATLAB code allowed, starting from the acquired image, to extract the markers' contours and centers, and consequently to automatically calculate the parameter of interest, i.e., the percentage of stretch.

Furthermore, to generalize the platform and the stimulus imposed by it, we also evaluate the compressive stretch. In this case, the samples were pre-stretched to 4 mm, the gel was deposited, the markers were inserted into the PDMS sample channel, and finally the samples were compressed to their original length. In this case, photos were acquired for each sample in the initial pre-stretched condition and after the compression, and subsequently image processing was performed.

Four conditions were tested for both tension and compression cases: only PDMS with markers positioned on the surface of the channel, CELLINK START, GE-CH-PEG, alginate-based hydrogels cross-linked with the Cellink's $CaCl_2$ solution diluted (1:2 with PBS) and not. For each tested condition, 10 repetitions were analysed.

4.1.2 Numerical assessment

At the computational level, the hydrogel stretch was simulated by adding to the previously validated numerical model (Chapter 3) a parallelepiped with a side of 0.93 mm (thickness of the channel) and a height of 0.35 which corresponds to the height of the hydrogel layer defined by G-code. Simplified material properties of a hydrogel were associated with this part, specifically an incompressible elastic linear behavior with a Young's Modulus of 30 kPa [133] and a Poisson ratio of 0.48 [134] was defined (Figure 4.1B). Finally, the part was discretized with a 0.4 global seed mesh (like the PDMS support).

About the hydrogel-PDMS interaction, between the lower surface of the gel and the upper surface of the support channel, two different types of interactions were investigated: a tie- and a non-tie interaction. The tie constraint was investigated to try to reproduce the behavior of soft hydrogels capable of adhering to PDMS supports and therefore stretching coherently with it. On the other hand, the non-tie constraint was investigated to simulate the behavior of stiff hydrogels that do not interact with the underlying PDMS support. At the end of the simulation, the distance between two points of the mesh, which were approximately in the same position of the experimental markers, was extracted. Finally, the percentage of stretching was obtained as follows.

$$\%hydrogel\_stretch = \frac{Relative\_displacement}{Base\_distance} * 100 \tag{4.2}$$

4.1.3 Hydrogel stretching: experimental results

First of all, the percentages of deformation were evaluated in the case of samples subjected to traction stimulus both with the approach through ImageJ software and through MATLAB code. Comparing the results, as shown in the Appendix Figure A.4, it can be seen that no statistically significant difference was observed between the two approaches. Therefore, since the two methods are equivalent and since the MATLAB code allows to automate and speed up the image analysis, this method was selected for the subsequent analyses.
Furthermore, as shown in Figure 4.2A, as expected, the non-cross-linkable CELLINK START hydrogel and the chemically cross-linked GE-CH hydrogel showed excellent elongation, coherently with their particularly soft consistency. However, the alginate-based hydrogel when cross-linked with pure $CaCl_2$ was found to be too stiff to stretch while the 1:2 diluted cross-linker allowed for greater traction.
Finally, comparing the results obtained from the traction and compression experiments, no statistically significant difference was observed in any case except for the alginate-based hydrogel cross-linked with the pure $CaCl_2$ solution. Indeed, as showed in Figure 4.2A, it is evident that the compressive stimulus allows to facilitate the deformation even in the case of totally cross-linked rigid alginate.

4.1.4 Hydrogel stretching: comparison between experimental and numerical data

To validate in another way the computational model, the experimental and numerical results relating to the hydrogel stretching were compared. Experimental and numerical results are presented, in Figure 4.2B, as box-plots and scatter plots, respectively. The results highlight that the numerical model with the tie interaction between the PDMS support and the hydrogel is validated for all conditions except in the case of the purely cross-linked alginate-based gel. As we expected, in fact, the purely cross-linked alginate is excessively rigid, thus it does not adhere to the PDMS support, and consequently it does not stretch coherently with it, as highlighted also by the experimental results in the Section 4.1.3.
However, as shown in the Figure 4.2B, the non-tie interaction was found to be able to model the totally cross-linked PDMS-alginate interaction by validating the computational model.
In conclusion, as the FEA model was able to reproduce the behavior of the different hydrogels observed during the experimental activity, it was subsequently exploited to test new structures and generalize the supports.

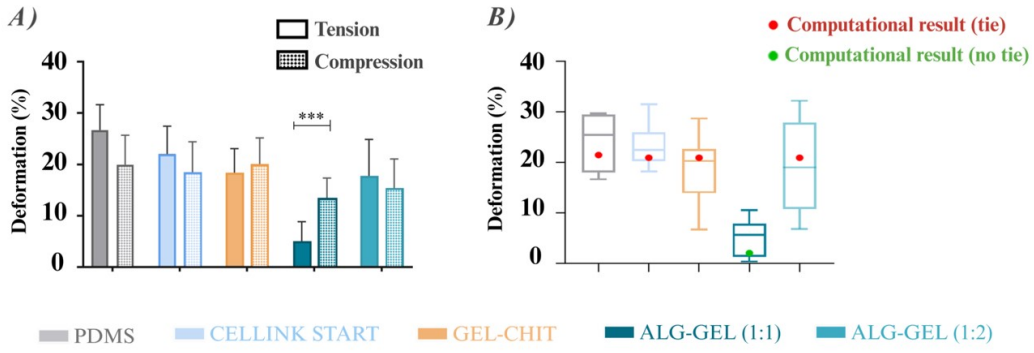

Figure 4.2: Assessment of hydrogel stretching: experimental and numerical results. A) Comparison of results obtained from image analyzes of tensile and compression tests using the automated approach. B) Comparison of the experimental results with those obtained from the two numerical simulations (tie and no-tie constraint).

4.1.5 Support generalization

Based on the results obtained and in particular on the insufficient interaction between PDMS and purely cross-linked alginate hydrogel, the idea

was to generalize the supports by introducing new structural elements within them to optimize the transmission of the deformation to the hydrogel. The two main structural elements evaluated are the insertion of pins or holes within the support channel. This choice is also supported by other literature studies.
For example, Zhang *et al.* [128], improved the adhesion between PDMS and a hydrogel by exploiting a series of micropillars which allowed an increase in the contact surface between the two materials.
While, Christensen *et al.* [135], in 2019, created a 3D printed polyethylene glycol diacrylate platform, characterized by two pins that are used as attachment points for the formation of a strip of muscle tissue. A hydrogel containing the cells of the C2C12 line was deposited inside the platform and acted as an ECM for the culture.
Therefore, based on these studies, it was decided to introduce the pin as a new structural element within the channels of the PDMS supports. Conversely, the structure with the holes was designed with an inverse logic, *i.e.* assuming that the fit of the hydrogel inside the holes facilitates its elongation. To allow the insertion of pins and holes, taking into account the printing resolution for the mold realization, the channels have been enlarged, compared to those originally designed from 0.93 mm to 1.53 mm. The pin and hole geometries were created on the CAD by extruding, respectively, towards the outside and inside of the bottom of the channel, circular structures with a diameter of 0.7 mm. The height or depth of the elements is 0.6 mm in both cases.

Support generalization results

As control, the 4 mm tensile simulation of the PDMS support with smooth channel was used, considering the non-tie interaction to simulate the behavior of the alginate hydrogel totally cross-linked (Figure 4.3A). In this condition, the length of the hydrogel reaches 9.18 mm after deformation which compared to the initial length of 9 mm corresponds to approximately 2% elongation.
As regards the new structures, the one with the pins, it highlighted that the pins inside the channel are not able to keep the gel in place following deformation (Figure 4.3B). This phenomenon has also been observed experimentally due to the poor adhesion between the two materials. Similar behavior was observed with the structures with holes, in fact, as seen in the Figure 4.3C, the hydrogel bar bends at the ends and comes out of the channel.
To solve this problems, a further structural modification was introduced to the channel characterized by pins. In particular, disks were added to the top of each pin which act as a block/constraint for the hydrogel, as showed

in Figure 4.3D. The discs are characterized by a diameter greater than that of the pin (0.9 mm), so as to prevent the cross-linked hydrogel inside the channel from coming out.
By implementing this structure, the simulation results highlight that the hydrogel, in addition to being kept inside the channel, is also deformed, reaching a final length of 9.82 mm (approximately 10% deformation). Therefore this structure allows a better transmission of deformations to the hydrogel deposited on the stretchable supports compared to the other geometries.

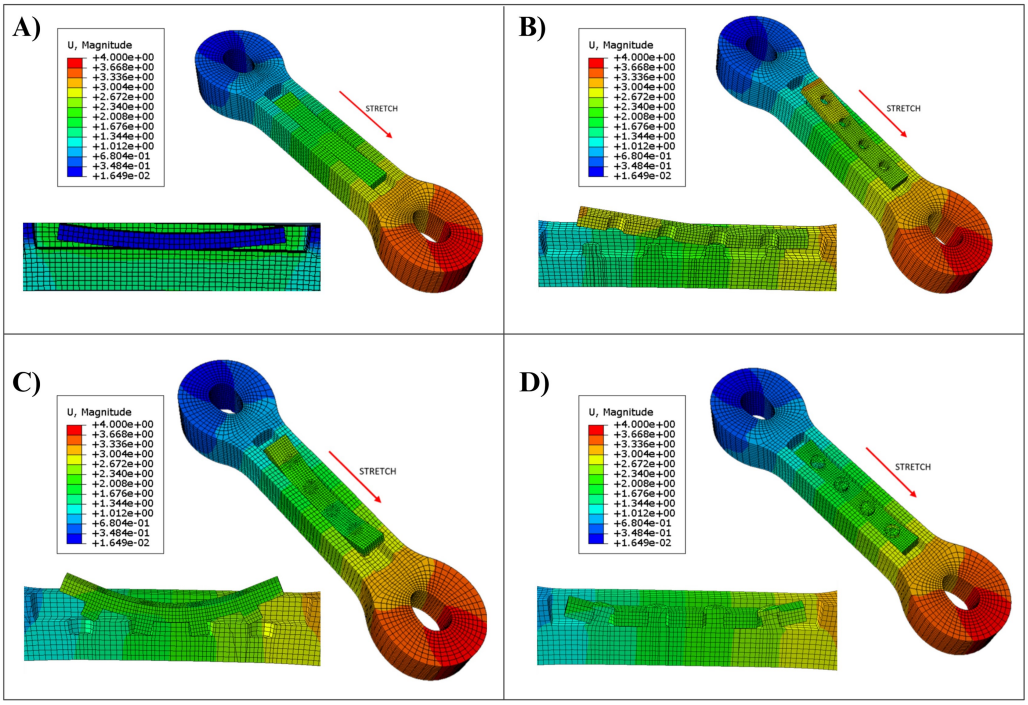

Figure 4.3: Generalization platforms results. A) Simulation result with smooth channel, B) with pins, C) with holes, D) with modified pins.

4.2 Sterility assessment

A crucial requirement for the mechanical platform is to ensure the materials are sterilizable and biocompatible, in order to effectively influence the *in-vitro* proliferation and differentiation of cells encapsulated within the hydrogel. To this aim, a further check to validate the proposed mechanical platform was carried out in terms of device sterility assessment. The SPDs were assembled with all components, including stretchable supports and the

screw with hexagonal head, and were subjected to an autoclave cycle to ensure sterility. Working under a hood, the culture medium was added inside the platforms until the supports were covered. The devices were then placed in the incubator and left in a humid environment at 37 °C in order to monitor the possible formation of contaminations.
After 4 days, SPDs left in the incubator showed contaminations (Figure A.5-i). This result was due to the porosity of the material used for printing the devices; in fact, being selected a powder bed printing technology, the printed material remains porous also after the post-processing.
To overcome this aspect, a PDMS Sylgard 184 coating was carried out on the internal surfaces. The PDMS polymer was generated as described in Section 2.2.1 by mixing the polymer base and the curing agent at the 1:10 ratio. Subsequently, the PDMS was brushed on the internal surfaces and left to cure for 24 hours at 60 °C (Figure A.5-ii).

4.3 Bioprinting and *in-vitro* biological characterization

Finally, the mechanical platform should favor, through the mechanical stimulus exerted, the *in-vitro* myogenesis of the cells encapsulated within the bioprinted hydrogel.
Therefore, as a last step in the validation and testing of the mechanical platform, the BioP was integrated on the platform and the biological effect of the dynamic culture on muscle cells was evaluated through cell viability and gene expression analyzes.

4.3.1 3D Bioprinting integration

Before the cell experiment, to obtain an accurate print on the platform, test prints were performed using a test hydrogel (Cellink START). The accuracy along the x and y axes was optimized, using a trial-and-error approach, by manually correcting the G-code initially generated by the software. The test prints and the G-code correction were repeated until the hydrogel was effectively deposited inside the 4 supports channels placed inside the SPD. The SPD had to always be positioned with the screw facing the front side of the printer. Thanks to the high reproducibility of the elastic supports and the SPDs and the presence of the reference position on the printing bed, it was possible to use, for the cell experiment, the single optimized G-code.
Instead, the Z-axis calibration is performed using a single reference elastic support as all the samples have approximately the same thickness.

Regarding the cell experiment, before starting the printing process, the bioprinter was placed under a sterile hood. UV light was turned on for 1 h to sterilize all the materials and surfaces. CELLINK Fibrin hydrogel was mixed with C2C12 cells (10:1 ratio). The cartridge was filled with bioink, then nozzle connected (inner diameter 0.41 mm), and finally placed into the PH1. The PH1 printing temperature was kept constant at RT. HEPA filter was activated setting 100 % air flow, ensuring the sterility of the working area during the entire printing process. In order to perform the printing step directly on the supports placed in the bioreactor, a 3D printed reference was placed on the printing plate. This referment has the dimensions of the printer plate and a central hole of the bioreactor dimensions (Figure 4.4A). The autoclaved SPDs were opened under the hood and positioned in the center of the reference. The axes were homed, and for the calibration of the Z-axis, the x- and y-axes were first adjusted to position the nozzle directly above the central channel of the elastic support located inside the mechanical platform. Next, the Z-axis value was decreased until the nozzle made contact with the surface of the channel. Once this was completed, the Z calibration was finalized, and the x- and y-axes were returned to their initial positions or to the center of the print bed. Additionally, the pressure and printing speed were set according to standard guidelines, specifically 10-15 E^3 Pa for pressure and 0.01 m/s for speed. The 3D constructs were bioprinted on the PDMS supports placed inside the bioreactor.
After printing, the cross-linking process was performed as follows. $CaCl_2$ droplets were applied to cover the whole 3D structure and immediately after, the samples were incubated for 5 min at RT. The cross-linking solution was subsequently removed from the constructs and DMEM culture complete medium was added. Dishes were then incubated at 37 °C and 5% CO_2. The cross-linking process was repeated weekly before medium refreshment to keep the 3D structure unchanged and avoiding degradation.

4.3.2 *In-vitro* biological characterization

To validate the biocompatibility of the SPDs, cellular tests were carried out. To this aim, we printed 9 SPDs (36 samples) of which 6 were monitored in static conditions and 3 in dynamic conditions for up to 14 days. All samples were kept in a static culture condition in a proliferative medium for 2 days post-printing to avoid excessive cell stress. Then, the proliferative medium was replaced with the differentiative one for all samples. Furthermore, regarding the dynamic condition, the samples were stimulated cyclically (12%, 1 Hz, 15 minutes stretch + 15 minutes rest, for 5 hours/day for 2 days) us-

ing the developed mechanical platform (Figure 4.4B). The strain percentage equal to 12% compared to the initial length of the samples was used, as it falls within the range defined by previous works [75, 76, 80–82, 119], 12% [77, 119]. Furthermore, the protocol with 15 minutes of stretching + 15 minutes of rest for 5 hours a day for 2 days was adapted starting from the study by Oortgiesen *et al.* [136], in which the stimulation thus defined had provided encouraging results.
Then, cell viability and gene expression were assessed at 7 and 14 days of culture by LIVE/DEAD assay and RT-PCR analysis, following the protocols described in Appendix Sections A.2.2 and A.2.2. Specifically, to elucidate the differentiation process of C2C12-laden bioink for both static and dynamic conditions, the gene expression profile of relevant myogenic differentiation markers was evaluated. Different genes were selected according to the time points. MyoD, Myf5, and Cyclin D1 were analyzed at 7 days of culture; MyoD and Myf5 as genes characterizing early muscle differentiation, and Cyclin D1 for evaluating cell proliferation. At 14 days of culture, MyoD, MyoG, MyH1, and Cyclin D1 were evaluated; MyoD was measured to study early differentiation, MyoG and MyH1 for late differentiation, and finally, Cyclin D1 to evaluate cell proliferation. The primer sequences used for gene expression analysis are listed in Table A.1.

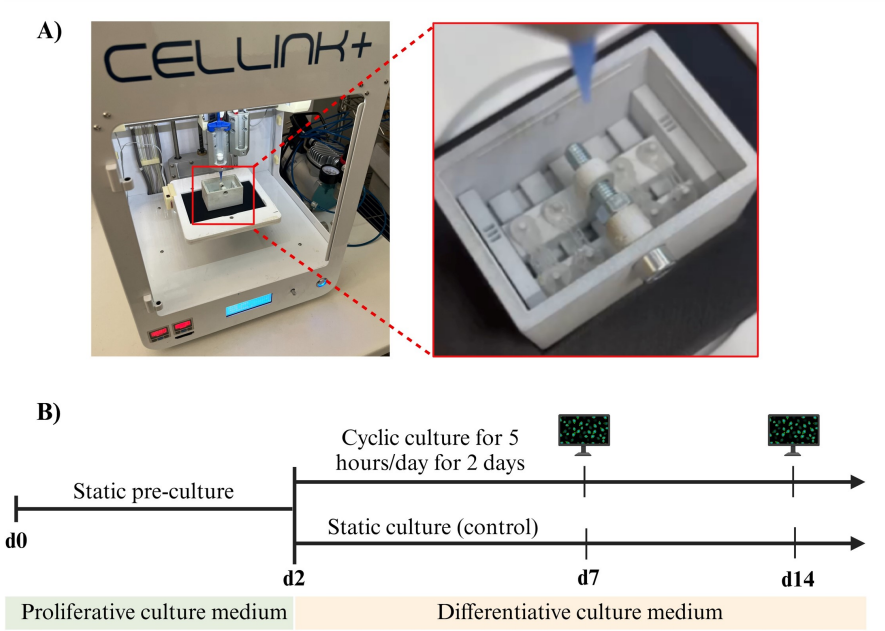

Figure 4.4: BioP integration and biological validation. A) BioP process integrated on the mechanical platform. B) Biocompatibility experiment.

Results of biological assessment

Live/Dead staining and RT-PCR were performed at 7 and 14 days in culture for both bioprinted structures treated under static and dynamic conditions. The C2C12s encapsulated inside the hydrogel and bioprinted inside the channels of the PDMS supports showed an excellent viability of approximately 90% at each time point in both the static and dynamic cases. Furthermore, the cells did not show a perfectly rounded morphology but in some areas cell elongations were observed. However, it was not possible to discriminate the effect of mechanical stimulation on a morphological level. Conversely, in the case of the quantitative RT-qPCR test, a significant effect of mechanical stimulation on gene expression was highlighted both at 7 and 14 days. At 7 days mechanical stimulation increased cell proliferation indicated by a statistically significant expression of the cyclin D1 gene. The Myf5 gene was more expressed in the dynamic case compared to the static one but there was no a statistically significant difference while MyOD highlighted a statistically significant greater expression in the dynamic case compared to the static one. Regarding the 14 days, Cyclin D1 is expressed more with a statistically significant difference in the static case, indicating that in the dynamic case the process of cellular differentiation has already started. In fact, the three differentiation genes appear to be more expressed in the dynamic samples, specifically MyoG and MyH1 are expressed with a statistically significant difference, suggesting the initiation of the late cellular differentiation.
Concerning these biological results, the increased gene expression due to the applied mechanical stimulation confirms what was previously observed in other works [76, 78, 83]. On the other hand, contrary to other studies in the literature, it was impossible to observe the effect of mechanical stimulation at the cellular morphological level. In literature, this aspect has been observed in particular in studies in which mechanical stimulation was applied on 2D membranes seeded with cells [78–80]. Placing cells within a 3D environment adds complexity and affects the outcomes of biological experiments. This is particularly important for the C2C12 cells used in this study, as they rely on adhesion for growth. Therefore, it is essential to use a hydrogel that includes specific adhesion sites to allow the cells to proliferate, differentiate, and respond to external mechanical stimulation. In this research, we aimed to evaluate the suitability of Cellink Fibrin hydrogel for transmitting mechanical stimulation to cells incorporated and bioprinted within the hydrogel. Our choice of this material was based on previous studies that identified Cellink Fibrin as a suitable option during a bioink screening process [5]. However, most studies employing 3D constructs for this application

have used, as biofabrication material, collagen, or home-made fibrinogen-based hydrogels which are particularly suitable for this application [76, 81, 119]. In particular, in 2015, Heher *et al.* created, by casting, rings made of a home-made fibrin-based hydrogel loaded with C2C12 cells [76]. These rings were subjected to a quasi-static mechanical stimulation (after 3 days of static culture, mechanical stimulation in the bioreactor was started by application of 10% static strain for six hours followed by an 18 h rest phase at 3% static strain. This strain protocol was repeated for 6 days). Results highlighted that the stimulation promoted cellular alignment and the presence of myotubes with a more mature phenotype in terms of sarcomeric patterning, diameter, and length. Furthermore, on the molecular level, a faster progression of the myogenic gene expression program is evident as myogenic determination markers, such as MyoD and Myogenin, are significantly upregulated when strain is applied. In the study most similar to the work presented in this thesis, Xuan *et al.* bioprinted cell-laden constructs made of hSMCs mixed with the GelMA/alginate blend solution [83]. These bioprinted constructs were subjected to a dynamic mechanical stimulation (semi sinusoidal pulse of 1 s delivered at a frequency of 0.5 Hz. The cells were continuously stimulated at the same time every day for one h, for a total of 6 days). Results show that the transcription level of all genes was significantly promoted by stimulation, however, even in this study, no effect was observed at the cellular morphological level.

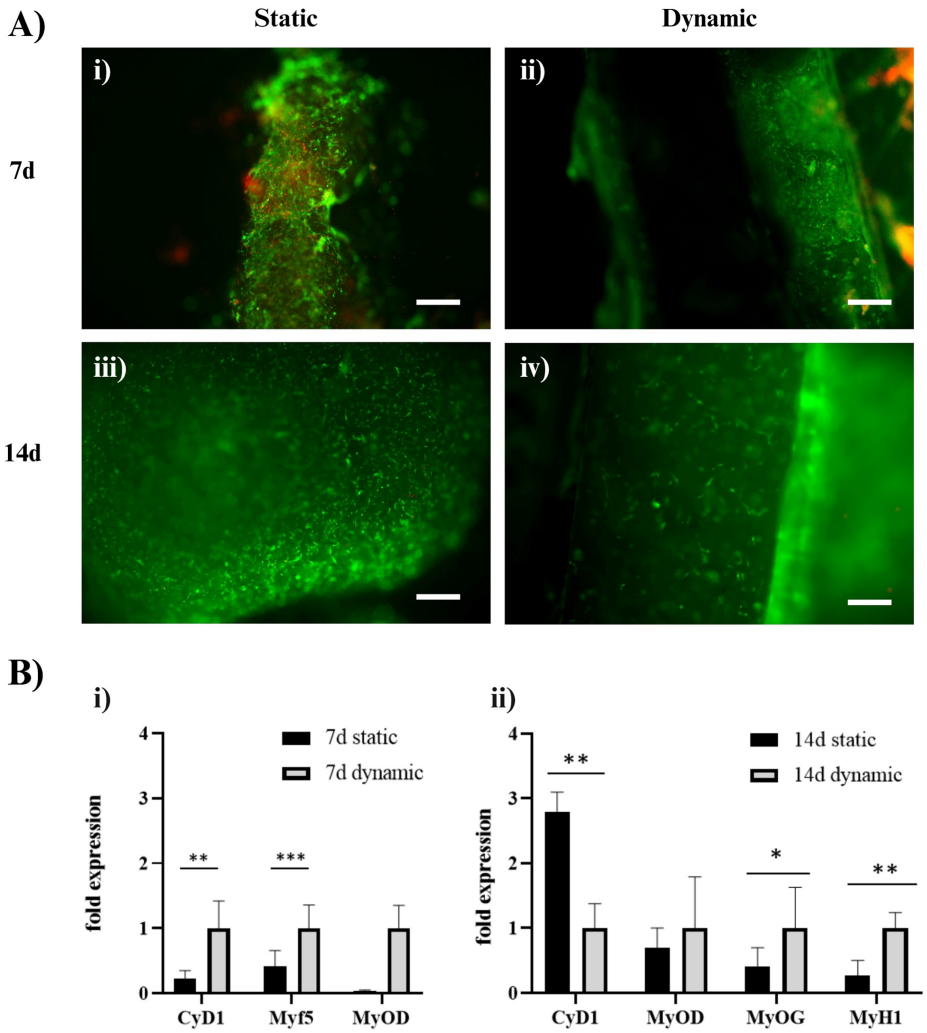

Figure 4.5: *In-vitro* biological validation. A) Live (green)/Dead (red) images and B) Gene expression analysis of 3D bioprinted constructs cultured in static and dynamic conditions at 7 and 14 days. Scale bar 50 μm. Statistically significant values are indicated as $*P < 0.05$, $**P < 0.01$, and $***P < 0.001$. Analysis of variance test was performed to evaluate data significance.

4.4 Discussion, Limitations, and Conclusions

Concerning the numerical hydrogel stretching assessment, the two points selected for the distance calculation are approximately correct as they are nodes of the mesh discretization which therefore do not correspond exactly to the positions of the markers. This aspect could be improved by refining the mesh of the PDMS supports, in order to selected the two points as close

as possible to the experimentally measured position. Furthermore, a reference should be used to position the markers always in the same position.
Another aspect concerning the computational model is the fact of having simulated all the hydrogels with the same mechanical properties obtained experimentally for the alginate hydrogel [133]. It would be more correct to characterize mechanically all hydrogels and assign the specific properties of each hydrogel.
Finally, the computational model has been validated on several occasions, the fabrication of the new generalized PDMS structures with pores and pins could be a further verification.
Regarding biological experiments, the main limitation concerns the biomaterial. Indeed, our starting point in this work was to test the entire workflow with a biomaterial previously selected for the static culture of C2C12 cells [5]. However, it will be necessary to carry out a screening of materials also for the dynamic culture, taking into account that the material to be selected must allow cell adhesion with specific adhesion sites and the consequent transmission of the stimulation to the cells. For this purpose, collagen-based biomaterials are often proposed in the literature and will be analyzed for future experiments. Furthermore, at the moment the tests have been carried out with a murine cell line, it will be necessary to repeat the process also switching to a human cell line. Regarding the stimulation protocols, it will be necessary to carry out a more detailed evaluation, testing multiple protocols, to select ad hoc parameters for stimulation. Moreover, cell culture protocols such as the duration of culture in proliferative and differentiative medium will need to be optimized based on this application.
Furthermore, regarding the device design and sterility, SPDs should be made using a different material for two main reasons: first, the selected PA12 material is not transparent and does not allow visual monitoring of the structures inside, and secondly, it has highlighted contamination problems linked to its porosity. In this regard, the solution based on the PDMS coating of the internal surfaces of the culture chamber is considered temporary and unsuitable for intensive use of the bioreactor, as the PDMS tends to degrade over time and with the autoclave cycles. Therefore, to avoid repeating the procedure over time, a more effective solution could be to use a different production technique for the SPD, such as the stereolithography approach and the use of cytocompatible, autoclavable, and transparent resins, widely adopted in the prototyping of bioreactors [137]. As mentioned in Section 3.4, we identified the possible materials for this purpose: Formlab dental resin [68] and Stratasys Med610 material.
Finally, the approach proposed in this work, the BioP-integrated platform, compared with recent and innovative approaches such as *in-situ* BioP, high-

lights the dependence of printing on the initially optimized G-Code, constrained by platform geometry and position in the printing bed. Therefore, by changing the geometry of the biological construct to be realized and its position in the printing bed, the entire pre-printing process from the generation of the G-code to its optimization must be repeated. On the contrary, approaches such as *in-situ* BioP offer a greater number of degrees of freedom and automation. An initial *in-situ* BioP strategy applied on supports is proposed and presented in Appendix A.4.4. In this strategy, it is possible to obtain a G-Code after processing a photo of the printing plate with the support on which to print. In this way, greater flexibility is obtained in terms of the geometry to be printed and the position of the object in the printing bed, even when printing multiple supports. However, this approach is based on a segmentation algorithm and has the limitation linked to the need to highlight the edges of the support channel in which to print. This highlighting step is incompatible in the case of BioP with cells as it requires high levels of sterility; therefore, this proposed strategy will have to be optimized.

Chapter 5

Conclusions and Future Developments

This thesis focuses on the design, manufacturing, and benchmarking of a BioP-integrated mechanical platform intended for the *in-vitro* culture and stimulation of elastic supports containing a bioprinted cell-loaded hydrogel, to promote the muscle regeneration for future applications such as the development of preclinical platforms for drug screening and disease modeling. The integration of the 3D BioP with a mechanical platform developed through the support of computational tools represents an interesting approach in TE and regenerative medicine to obtain next-generation 3D cellular constructs with myogenic induction, improving the speed and the quality of new muscle formation.

In this scenario, BioP to recreate an *in-vitro* muscle fiber model was preliminarily applied in the lab BioP@UniPV, obtaining promising results, but also highlighting two main limitations: the escape of cells from the construct and their growth on the Petri dish and the differentiation non-homogeneous and pronounced at the edges of the structures. To overcome these problems, a proposed solution is to create supports to contain the bioink and avoid the colonization of cells on the Petri dish and to create a mechanical platform capable of promoting differentiation through the provided mechanical stimulation.

Consequently, the cell supports proposed in this thesis (Chapter 2) allow the bioink containment, avoiding the escape of cells from the hydrogel, but also the transmission of the mechanical stimulus to the cells thanks to the elasticity of the PDMS, the selected manufacturing material.

However, finding a suitable design for the mechanical platform that allows the correct transmission of the physical stimulus using a trial-and-error ex-

perimental approach is expensive and time-consuming. To this end, computational tools were used to support the platform design. In particular, a structural model was implemented; it was calibrated and experimentally validated through mechanical and printing tests.
The experimental and numerical study of the platform (Chapter 3) showed a good correspondence between the experimental and numerical results, in fact, the 3D printed structures highlighted the same post-stretch behaviors numerically obtained. Therefore, this study demonstrated that it is possible to optimize the design of the mechanical platform by exploiting a numerical model. The configuration numerically selected was then exploited to create the cyclic prototype of the platform based on a stepper motors actuation mechanism controlled via an electronic circuit and Arduino microcontroller. Furthermore, a proof-of-concept temperature and humidity sensor was connected to the Cloud, monitored remotely, and validated using the output data indicated by the cell incubator.
Finally, the mandatory validation of the proposed mechanical platform was carried out by analyzing the transmission of the mechanical stimulation from the stretchable support to the 3D construct, the integration of the BioP on the platform, the device sterility, and finally the biological effect of the dynamic culture on muscle cells.
The study of the interaction between PDMS supports and hydrogels deposited on the top of them (Chapter 4) demonstrated that soft-textured hydrogels are able to stretch coherently with the underlying support while stiff hydrogels, such as purely cross-linked alginate, are not able to interact and therefore stretch. The *in-silico* study confirmed the experimental trend; specifically, results highlight that the numerical model with the tie interaction between the PDMS support and the hydrogel validated the soft hydrogels behavior while the non-tie interaction was found to be able to model stiff hydrogels. This trend does not occur in the case of experimental compression stimulation, where even cross-linked alginate can deform.
Then, the sterility of the BioP integration process was demonstrated and the *in-vitro* biological characterization (Chapter 4) demonstrated that the platform markedly influences the behavior of murine myoblasts encapsulated in the hydrogel already after 7 days of culture.

In conclusion, the present research activity have demonstrated the importance of a framework to support the design of a cutting-edge BioP-integrated mechanical platform. Prototypes are now available for efficacy testing in muscle regenerative medicine and in particular for their use as preclinical platforms for drug screening.

5.1 Futures developments

Future developments of the study will certainly focus on deepening the biological characterization.
In particular, in this work a biomaterial previously selected for the static culture of C2C12 cells was used [5]. A screening of biomaterials for dynamic culture will then be carried out, taking into account that the material to be selected must allow cell adhesion with specific adhesion sites and the consequent transmission of stimulation to the cells. For this purpose, collagen-based biomaterials are often proposed in the literature and will be analyzed for future experiments. Furthermore, at the moment the tests have been carried out with a murine cell line, it will be necessary to repeat the process also switching to a human cell line. Regarding stimulation protocols, it will be necessary to carry out a more detailed evaluation, testing multiple protocols, to select ad hoc parameters for stimulation. About cell culture protocols, such as duration of culture in proliferative and differentiative medium, will need to be optimized based on this application. Furthermore, the cyclic prototype will be modified by implementing other types of motors or other stimulation systems in order to improve performance and stimulate as many samples as possible in parallel and address limitations such as vibrations. As regards other stimulation systems, the implementation of mechanical stimulation using Shape Memory Alloys, an activity already started in a preliminary way, will be explored in depth.
Finally, regarding the device design and sterility, SPDs should be made using a different material for two main reasons: first, the selected PA12 material is not transparent and does not allow visual monitoring of the structures inside and secondly, it has highlighted contamination problems linked to its porosity. In this regard, the solution based on the PDMS coating of the internal surfaces of the culture chamber is considered temporary and unsuitable for intensive use of the bioreactor, as the PDMS tends to degrade over time and with the autoclave cycles. Therefore, to avoid repeating the procedure over time, a more effective solution could be to use a different production technique for the SPD such as the stereolithography approach and the use of cytocompatible, autoclavable, and transparent resins, widely adopted in the prototyping of bioreactors [68, 137].

Appendix A

Appendix

A.1 Other 3D printing and bioprinting applications during PhD

A.1.1 Printing evaluation of new customizable bioinks for 3D bioprinting applications

Innovative biomaterials are necessary to create bioink suitable for bioprinting that is rapidly adopted by pharmaceutical industry and research labs for drug testing and TE. Our project proposes for the first time a library of customizable hybrid inks with biochemical and mechanical properties tunable on the basis of the interest tissue, e.g., lung, colon, and skin. The project aims to transfer a preliminary bioink formulation to a ready-tomarket biomaterial, assessing: i) printability and shape fidelity; ii) biological compatibility with different cellular lines; iii) scale-up of the manufacturing process to sustain high-volume production; iv) storage and stability studies.

Collaboration with L. Russo (Dept. of Biotechnology and Biosciences, Milano-Bicocca University).

A.1.2 Design and biofabrication of bacterial hybrid living materials with robust and multiplexed biosensing capabilities

This activity focuses on the use of synthetic biology techniques combined with Bioprinting to create engineering living materials. Our project started

with the realization of an innovative bacterial printing setup to obtain biosensors of hormones and antibiotics, and an actuator that produces a polymer helpful in bioremediation. The results are promising, and future studies will focus on improving cell viability, quantifying heavy metals removal, and proposing biocontainment strategies for a safe use in the environment. Taken together, these two types of materials could represent a new generation of biodegradable, user friendly, reproducible devices to aid in toxic substances detection or valuable biomolecules production.

Collaboration with L. Pasotti, F. Usai, P. Magni (BMS Lab., Pavia University).

A.1.3 *In-situ* bioprinting for wound healing applications in Hirudo medicinalis

This activity focuses on the development and validation of an in situ bioprinting of the 3D model in Hirudo medicinalis. The aim was, using an in vivo model of wound healing in Hirudo medicinals already used by ASAcampus UNIFI colleagues, to implement in situ bioprinting techniques directly in the wound bed to promote and accelerate healing. For this purpose we worked in particular on the formulation of the bioink which must meet the requirements suitable for in situ bioprinting and promote the healing process. Then, we worked on 3D designing the wound bed and optimizing the 3D bioprinting process (print setup and workflow).

Collaboration with ASAcampus(Monica Monici, Resp. lab.), Dip. Di Scienze Biomediche Sperimentali e Cliniche, UNIFI.

A.1.4 3D bioprinted osteosarcoma model for experimental Boron Neutron Capture Therapy applications preliminary assessment

Osteosarcoma is the most common primary malignant bone tumor affecting children and adolescents. Despite the introduction of several therapeutic options, the treatment and cure of osteosarcoma still remains an open challenge.
For this reason, Boron Neutron Capture Therapy (BNCT) has been investigated as an alternative or integrative treatment. BNCT is an experimental binary radiotherapy based on the irradiation with low energy neutron of neoplastic cells previously enriched with atoms of 10-boron. This alternative

technique selectively destroys neoplastic cells while sparing normal ones. The goal of this work is to create tumor models using 3D bioprinting for BNCT studies. In particular, this study focuses on the optimization of the technical protocol for bioprinting the in vitro osteosarcoma tumor model.

Collaboration with C. Ferrari, L. Cansolino, E. Delgrosso (Dept. of Clinical Surgical Sciences, Pavia University); INFN; Dept. of Physics, University of Pavia; F. Riva (Dept. Public Health, Experimental and Forensic Medicine, Histology and Embryology Unit, Pavia University).

A.1.5 Development of an *in-vitro* muscle fiber model using volumetric BioP based on xolography

Volumetric 3D printing abandons the conventional sequential approach of layer fabrication in favor of direct curing of a volume of resin defined with arbitrary geometry. Therefore, it allows the creation of geometrically complex objects without support structures at unprecedented printing speeds. Xolography is a rapid volumetric 3D printing method that uses dual-color polymerization (DCP) for precise volumetric polymerization via photoswitchable photoinitiators. The goal of this work is to: 1) optimize the printing of a commercial resin xoloOne_375T; 2) optimize the formulation of a bioink based on methacrylated gelatin, DCPI photoinitiator and BisTris buffer that can be compatible for printing and cell encapsulation.

Collaboration with Matteo Moretti, RTM research group, Bellinzona Research Institute.

A.2 Design and development: stretchable supports

A.2.1 3D co-printing strategy

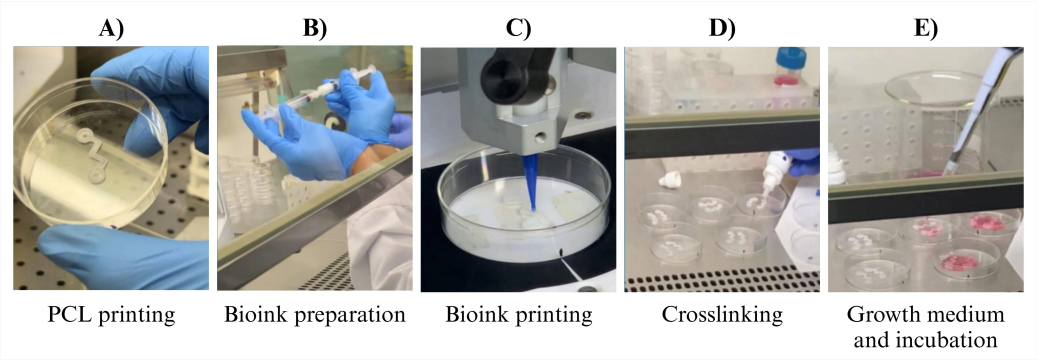

Figure A.1: 3D co-printing process: A) PCL printing; B) Bioink preparation; C) Bioink printing; D) Crosslinking with $CaCl_2$; E) Addition of growth medium and incubation at 37 °C.

A.2.2 3D co-printing: *in-vitro* biological characterization

LIVE/DEAD

The LIVE/DEAD assay provides a two-color fluorescence cell viability assay that is based on the simultaneous determination of live and dead cells with two probes. In this thesis, calcein and ethidium homodimer (EthD-1), optimal dyes for this application, were used. Calcein is well retained within live cells, producing an intense uniform green fluorescence. EthD-1 enters cells with damaged membranes and undergoes a 40-fold enhancement of fluorescence upon binding to nucleic acids, thereby producing a bright red fluorescence in dead cells. DAPI or 4',6-diamidin-2-phenylindole was also subsequently added. It is a fluorescent organic dye that strongly binds rich DNA regions in A-T sequences. It is widely used in fluorescence microscopy to highlight cell nuclei and takes on a blue tint.
In this study, we used the Live/Dead staining purchased from Invitrogen (Waltham, US). In detail, 500 μL of a solution consisting of 1.5 ml of Phosphate Buffered Saline (PBS), 3 μL of EthD-1, and 1.5 μL of calcein, was added to 3D constructs. Samples were incubated for 45 min in the dark, then the solution was removed, and cell nuclei were counterstained with 500 μL 40,6-diamidino-2-phenylindole (DAPI) for 10 min according to the protocol.

Fluorescent image acquisition was carried out by semi-confocal microscope (ViCo confocal, Nikon).

RT-qPCR

To elucidate the C2C12 cell proliferation and differentiation process, the gene expression of relevant myogenic differentiation markers was quantified using the Real-Time quantitative Polymerase Chain Reaction (RT-qPCR) at different time points.
RT-qPCR is a technique used to analyzed the mRNA and evaluate the expression levels of specific myogenic genes previously selected. The first method step is always to extract the total RNA and reverse transcribe it into complementary DNA (cDNA). In detail, the protocol started with nucleic acids extraction from cells using the TRIzol reagent. This reagent causes cell membranes rupture and allows DNA, RNA, and proteins isolation from the sample. In our case, with this approach, Fibrin was extracted from the central channel and consequently also the nucleic acids of cells deposited there. Then, Directzol RNA Miniprep reagents and the manufacturer's protocol (Zymo Research) were used for total RNA extraction from which we obtained a mix solution divided into three phases: the most superficial and transparent one is that of RNA, the whitish intermediate part is that of DNA and proteins, and the part in the bottom is the organic phase. Therefore, the transparent phase (RNA) was transferred into an Eppendorf and it was quantified by the NanoDrop^{TM} (Thermo-Fisher Scientific) spectrophotometer. After that, reverse transcription of the cDNAs, obtained from 350 ng of RNA, was performed using the iScript^{TM} cDNA Synthesis Kit (Biorad). Then, the expression of muscle genes of interest was quantified. The reaction and data analysis were performed respectively by using Mini-Opticon Real-Time PCR System (BioRad Laboratories) and CFX Manager Software. The expression of each gene was studied in triplicate and normalized using the expression of a housekeeping gene, i.e., phosphoglycerate kinase (PGK). The primer sequences used for gene expression analysis are listed in Table A.1.

Table A.1: Summary of primers used for RT-qPCR.

Gene	Primer sequences
PGK (115 bp)	Fw 5' CAA AAT GTC GTC TTC CAA CAA G 3' Rw 5'AAC GTT GAA GTC CAC CCT CAT 3'
MyoD (115 bp)	Fw 5' TGCACTTCCACCAACCCCAACCAGC 3' Rw 5' CCTGGACTCGCGCACCGCCTCACT 3'
Myf5 (176 bp)	Fw 5' GCCCTGAGGAAGAGGAACAC 3' Rw 5' CAAGGTCTCGAATGCTTGGT 3'
Cyclin D1 (150 bp)	Fw 5' TCCTGCTACCGCACAACGC 3' Rw 5' CCAGCTTCTTCCTCCACTTCCC 3'
MyoG (152 bp)	Fw 5' GGGCCCCTGGAAGAAAAG 3' Rw 5' AGGAGGCGCTGTGGGAGTT 3'
Myh1 (113 bp)	Fw 5' AGTCCCAGGTCAACAAGCTG 3' Rw 5' CACATTTTGCTCATCTCTTTG 3'

A.2.3 PDMS mechanical characterization

A.2.4 Comparison of results with literature

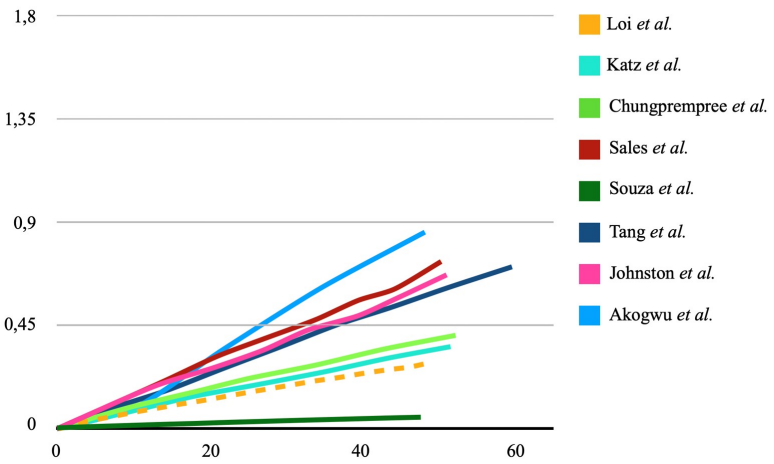

Figure A.2: PDMS mechanical characterization. Comparison of the results obtained in this study (dotted line) with those obtained in the literature.

Table A.2: PDMS mechanical characterization. Comparison of this work with other studies published in the literature.

Year	Author	PDMS ratio	PDMS curing temperature and time	Standard tensile test	Sample geometry	Tensile test speed
2024	Loi *et al.* [111]	1:10	60 °C for 24h	ASTM D412	115 x 25 x 2 mm	2 mm/min
2022	Katz *et al.* [138]	1:10	NA	NA	20 x 2.5 x 0.5 mm	5 N/min
2022	Chungprempree *et al.* [139]	1:10	60 °C for 3 h	ASTM D882	100 x 10 x 1 mm	50 mm/min
2021	Sales *et al* [140].	1:10	RT for 48h	ASTM D412	115 x 25 x 2 mm	500 mm/min
2020	Souza *et al.* [117]	1:10	85 °C for 45 min	ASTM D412	115 x 25 x 2 mm	2 mm/min
2017	Tang *et al.* [141]	1:10	NA	NA	20 x 2 x 1,4 mm	2 mm/min
2014	Johnston *et al.* [142]	1:10	25 °C for 48h, 100 °C for 48 min, 125 °C for 33min, 150 °C for 23 min, 200 °C for 18 min	ASTM D412	115 x 25 x 2 mm	254 mm/min
2010	Akogwu *et al.* [143]	1:10	60 °C for 1h	NA	26.457 x 10.257 x 1 mm	0.06 mm/min

A.2.5 Constitutive parameters extraction

Table A.3: MOONEY-RIVLIN

D1	C10	C01
0	0.142938766	-1.276394011E-02

Table A.4: OGDEN WITH N = 3

N	MU	ALPHA	D
1	-2.56997555	-3.47267193	0
2	1.38552274	-1.48308676	0
3	1.47389037	-5.58930310	0

Table A.5: NEO-HOOKEAN

D1	C10	C01
0	0.132540963	0

Table A.6: YEOH

C10/C20/C30	C01/C11/C21	C02/C12	C03	D
0.131421402	0	0	0	0
-5.119891592E-03	0	0	0	0
1.623948658E-02	0	0	0	0

Table A.7: ARRUDA-BOYCE

MU	MU_0	LAMBDA_M	D
0.206239358	0.260071387	1.80235258	0

Table A.8: VAN DER WALLS

MU	LAMBDA_M	ALPHA	BETA	D
0.261095174	9.97182442	-0.101627833	0.259520932	0

A.3 Design and development (2): mechanical platform

A.3.1 Structural FEA of the stretchable supports: comparison between experimental and numerical data

Table A.9: Stiffness K extracted from curves

Considered cases	Stiffness K ($N \cdot mm^{-1}$)
Experimental data	0.616
Ogden	0.589
Mooney-Rivlin	0.547
Neo-Hookean	0.556
Yeoh	0.551
Arruda-Boyce	0.545
Van der Waals	0.548

A.3.2 Structural FEA of the mechanical platform: results of numerical study

Table A.10: Computation time of FEA model varying mesh size.

	Course	Medium	Fine
Computational time	9 min, 56 sec	29 min, 13 sec	2h 51 min 45 sec

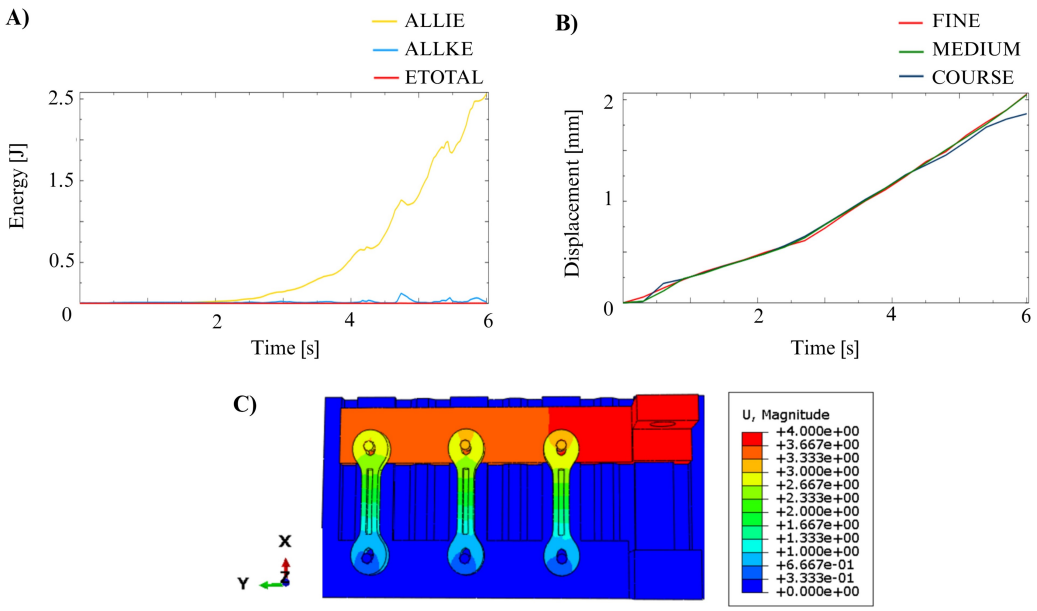

Figure A.3: Results of numerical study. A) Energy analysis: Internal, kinetics, and total energies. B) Tuning the mesh size of the FEA model. C) Numerical displacement distribution following a 4 mm stretch imposed by the mechanical platform in the case of the first prototype without 0.2 mm of tolerance.

A.4 Testing and benchmarking of the mechanical platform

A.4.1 Hydrogel stretching assessment: MATLAB code

```
%% Cleaning
clear
close all
clc


%% Image loading
img_in = imread('Sample4.jpg');
img_fin = imread('Sample4_3.jpg');
img_in = img_in(:,:,2);
img_fin = img_fin(:,:,2);
figure(1)
imshow(img_in)
```

```
figure (2)
imshow(img_fin)
title('Img')

    % Image binarization im_BW _in = imbinarize(img_in, 0.55);
im_BW_fin = imbinarize(img_fin,0.55);
im_BW_in = imcomplement(im_BW _in);
im_BW_fin = imcomplement(im_BW_fin);
figure(3)
imshow(im_BW_in)
imshow(im_BW_fin)
title('Binarized Img')

    % Erosion and dilation to eliminate non-functional dots.
se = strel('arbitrary', ones(1, 1), zeros(1, 1));
im_er_dil_in = im_BW_in;
im_er_dil_fin = im_BW_fin;

    %% Boundaries detection.
[Bound_in] = bwboundaries(im_er_dil_in,'noholes');
[Bound_fin] = bwboundaries(im_er_dil_fin,'noholes');
B_in = ;
B_fin = ;

    % Check, if the found object is too small, it is deleted.
for j = 1:length(Bound_in)
size_B_in = size(Bound_inj);
if size_B_in(1) > 200
B_in = [B_in, Bound_inj];
end
end

    figure(4)
imshow(im er_ dil_in)
hold on
MEAN1_in= mean (B_in1);
MEAN2_in= mean (B_in2);

    plot(MEAN1_in(2),MEAN1_in(1),'.', 'MarkerSize',10)
plot(MEAN2_in(2),MEAN2_in(1),'.', 'MarkerSize',10)
```

```
    for k = 1:length(B_in)
boundary = B_ink;
plot(boundary(:,2), boundary(:,1), 'r', 'LineWidth', 1)
end

    title('Initial boundaries')

    distance_iniziale=norm(MEAN2_in-MEAN1_in);

    for j = 1:length(Bound_fin)
size_B_fin = size(Bound_finj);
if size_B_fin(1) > 200
B_fin = [B_fin, Bound_finj];
end
end
figure(5)
imshow(im_er_dil_fin)
hold on
MEAN1_fin= mean (B_fin1);
MEAN2_fin= mean (B_fin2);
plot(MEAN1_fin(2),MEAN1_fin(1),'.', 'MarkerSize',10)
plot(MEAN2_fin(2),MEAN2_fin(1),'.', 'MarkerSize',10)

    for k = 1:length(B_fin)
boundary = B_fink;
plot(boundary(:,2), boundary(:,1), 'r', 'LineWidth', 1)
end

    title('Final boundaries')

    distance_fin=norm(MEAN2_fin-MEAN1_ fine);

    Percentage_all=abs((distance_fin-distance_ in)/distance_in)*100;
```

A.4.2 Hydrogel stretching assessment: Manual vs Automated approach

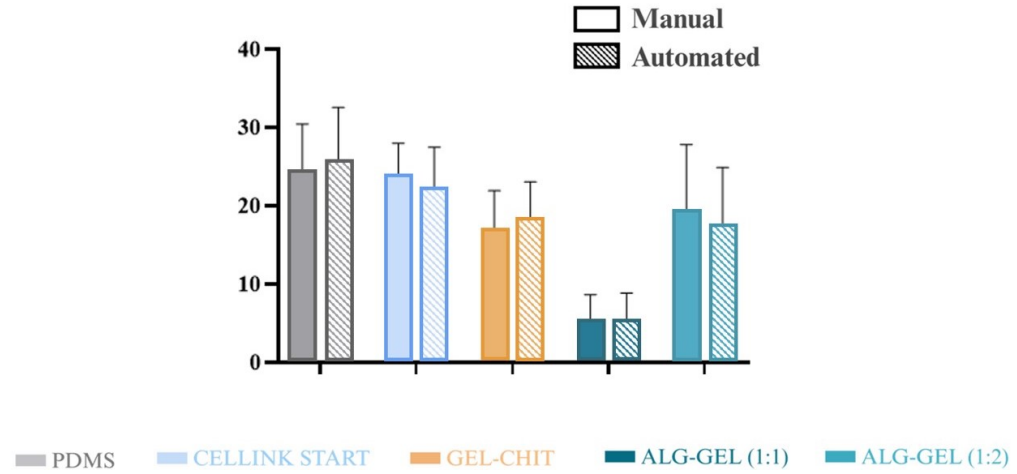

Figure A.4: Experimental assessment of hydrogel stretching. Comparison of results obtained from analyzing images using the manual or the automated approach.

A.4.3 Sterility assessment

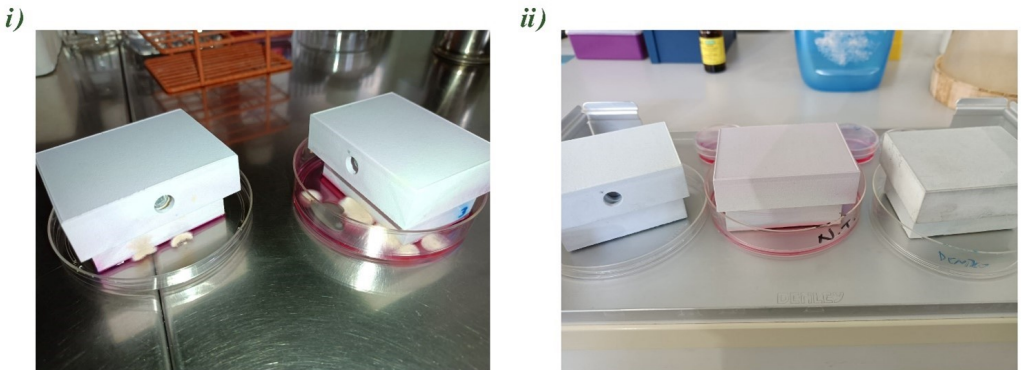

Figure A.5: Sterility assessment results. i) SPDs initially autoclaved, filled with culture medium and left in an incubator at 37 °C. They highlight leakage of culture medium and formation of contamination. ii) The PDMS coating treatment on the internal walls of the SPD solved the problem of culture medium leakage (SPDs on the right and left).

A.4.4 *In-situ* BioP strategy

Set-up for in-situ bioprinting

The purpose was to process a picture of the printing plate and the channel in which the printing will occur in order to obtain a specific G-code for the *in-situ* 3D BioP. Three steps were employed to switch from the acquired image to the final G-code. In each of them, a different software was used: i) image segmentation with MATLAB (R2019b): the image was imported, segmented, and the coordinates of the channel in which printed are extracted; ii) CAD model development with Autodesk Inventor: the CAD model was developed based on the extracted channel coordinates and the model was exported in STL format; iii) G-Code generation with Repetier-Host and Slic3r: the STL file was imported and the printing options were set for the G-code generation.
Before starting the printing step, the bioprinter set-up is performed. The axes are homed, and the z-axis is calibrated. Finally, the correct printing pressure is set: starting from a pressure of 0 kPa, the PH1 was opened, and the pressure was gradually increased until the material was extruded.

Picture acquisition of the printing bed

A software using MATLAB was developed to process an image of the printing bed and the area of the channel where *in-situ* BioP will take place. The processing involves binarization and segmentation techniques to emphasize both the outline of the channel and the printing plate. To outline the channel, the edges were colored with a black permanent marker.
Furthermore, the contour of the printing plate is essential to convert the pixel obtained from the segmentation into motion coordinates for the PH. Thus, to create a contrast detectable through segmentation, strips of black adhesive tape were placed along the edge of the white printing plate.
Then, a four-step procedure was followed to take the picture. First, the HEPA filter was removed from the top of the Bioprinter. Secondly, through the Bioprinter's Move axis function, the PHs were moved to the lowest coordinate on the x-axis and to the highest coordinate on the y-axis, to be able to frame the entire printing plate. Third, a phone was placed on the Bioprinter to take photos of the entire printing plate. Finally, the images were edited and cropped to the edges of the printing plate to segment and analyze only the objects of interest.

Image segmentation

The second step is performed in MATLAB; a code about the image segmentation and processing was developed. This step aims to obtain the coordinates of the channel in which it will be printed. The procedure of image segmentation can be divided into the following five phases.

1. *Image reading.* The image of the printing plate and of the object on which printing will happen, is imported on MATLAB. Since the printing plate images are color images (i.e., red, blue, and green), the resulting data is a 3D matrix. In order to work on a 2D matrix, only one channel is selected (Figure A.6A).

2. *Image binarization.* Firstly, the complement image was generated, which is a fundamental step to invert the image colors. Subsequently, the image was binarized, choosing an appropriate threshold that allows the identification of all necessary structures (i.e., the printing plate contour and the object of interest (Figure A.6B).

3. *Contour pixels selection.* The boundary pixels of all features in the binarized image were extracted. Then, a check was implemented that selects only the contour pixels of the printing plate and the objects of interest. This control is based on the number of pixels that compose an element and removes the elements that contain too few pixels since they could derive from shades in the picture (Figure A.6C).

4. *Transformation of contour pixels in coordinates.* The fourth step in order to extract from the image the correct movement coordinates for the 3D Bioprinter, is to convert the selected contour pixels in coordinates placed in the right reference system. The new reference system will be based on the real dimensions of the printing plate. Initially, the printing plate pixels are converted into coordinates; then the object coordinates are obtained. This transformation is needed principally for two reasons. Firstly, the read image automatically has a reference system centered in the upper left corner. This system origin has to be moved in the image center so that it can be congruent with the 3D Bioprinter settings. Secondly, the read image has a discrete representation, given by the pixels, which has to be modified in a continuous representation in order to create the CAD model. This transformation adjusts image dimensions according to the printer plate dimensions (Figure A.6D).

5. *Coordinates saving.* The last step is to save the extracted coordinates of the objects of interest. They are finally written in a XLSX file. The

XLSX format was chosen because it is easy to be read on Autodesk Inventor the CAD model development.

To give high usability, an app based on the code just described was developed with the section 'App Designer' of MATLAB. In the first window (Figure A.6E), there is a button ("Select the picture") to choose the desired picture from a folder, import it, and view the picture selected. Then, through a slicer, it is possible to choose a threshold for binarization and view the resulting binarized image in real-time. With another button ("Extract the contours") a second window opens. In the second window (Figure A.6F), starting from the binarized image, it is possible to view all the extracted contours and select only the contour pixels of interest that are converted in coordinates and shown in a plot. If the contour pixels aren't exact, the user can return to the previous window through a button ("Change the threshold") and change the binarization threshold. On the contrary, if the contours seem to be appropriate, it is possible to give a name and generate the XLSX file with the selected coordinates of the object of interest, thanks to a button ("Generate XLSX file").

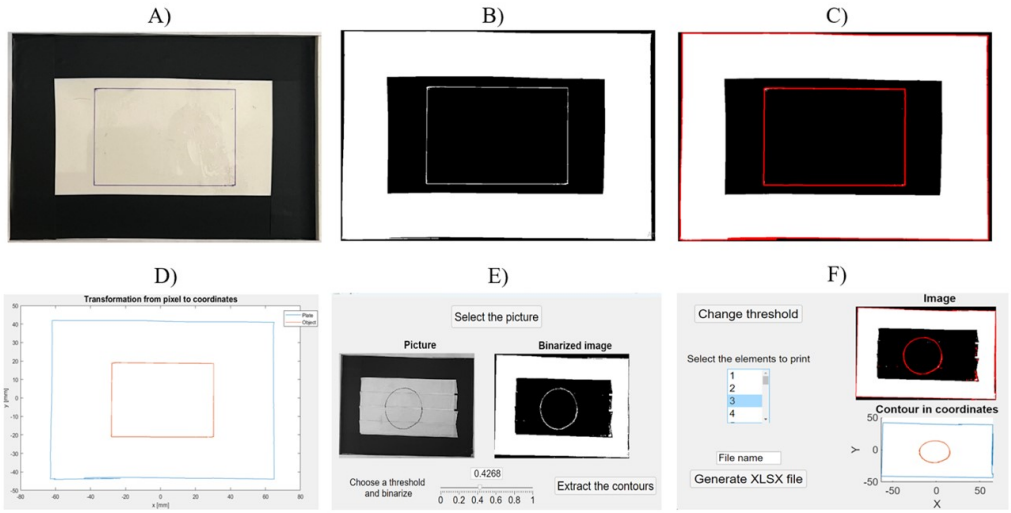

Figure A.6: Segmentation steps. A) Image reading. B) Image binarization. C) Contour pixel selection. D) Transformation of contour pixels in coordinates. App created with App Designer in Matlab. E) First window to select, import, and binarize the image. F) Second window to select the contour pixels and generate the XLSX file.

CAD model development

The points saved in the XLSX file and based on the printing plate coordinate

system, are imported in Autodesk Inventor. In particular, in the 2D sketch environment of Autodesk Inventor, the points can be imported through a specific function. Based on the shape given by the points saved on the XLSX file and derived from the image, a sketch is created in 2D. Then it is extruded and the height of the object extrusion is set as needed. The CAD model is then exported as STL file.

Options setting and G-code generation
The third part is about the G-code generation and the print settings. Initially, the STL file is imported in Slic3r where the printing parameters are set. The main parameters are summarized in Table A.11 and principally concern the extrusion height that defines the layer height, the extrusion width, and the printing bed dimensions and origins to correctly calibrate the printer. Then, the G-code is generated and printing is started.

Table A.11: Main printing parameters.

Layer height	0.35 mm
Default extrusion width	0.41 mm
Bed size (x)	128 mm
Bed size (y)	86 mm
Origin (x)	63 mm
Origin (y)	44 mm

Software validation

The protocol was optimized and validated through monolayer, multilayer, and the two support models (linear and serpentine). In all these tests, the selected ink was the SA-GE-based hydrogel.

Monolayer
The monolayer validation replicates some plan geometrical shapes drawn on the printing plate. A picture of the shapes was taken and processed. Finally, the printing was made, verifying the correct material deposition on the drawing. The procedure was optimized to correctly reproduce a rectangle, three straight lines, and a circle (Figure A.7A).

Multilayer
The multilayer validation was made through the correct deposition of four layers of material within a support with a hole. The first one was a par-

allelepiped with dimensions 10x10x2 mm. In this case, an SA-GEL-based hydrogel was used as it is cross-linkable with a $CaCl_2$-based solution and extractable from the support to analyze the structure. Furthermore, two different dyes were used mixed with the hydrogel to highlight the separation of the layers (Figure A.7B).

Supports To validate the set-up on the supports, the channel edges were highlighted with a black permanent marker. The image of the supports and the print bed was taken and processed. Finally, the print was performed, verifying the correct deposition of the material inside the channel. The procedure was validated by testing the protocol both on linear PDMS supports and on serpentine PCL supports (Figure A.7C).

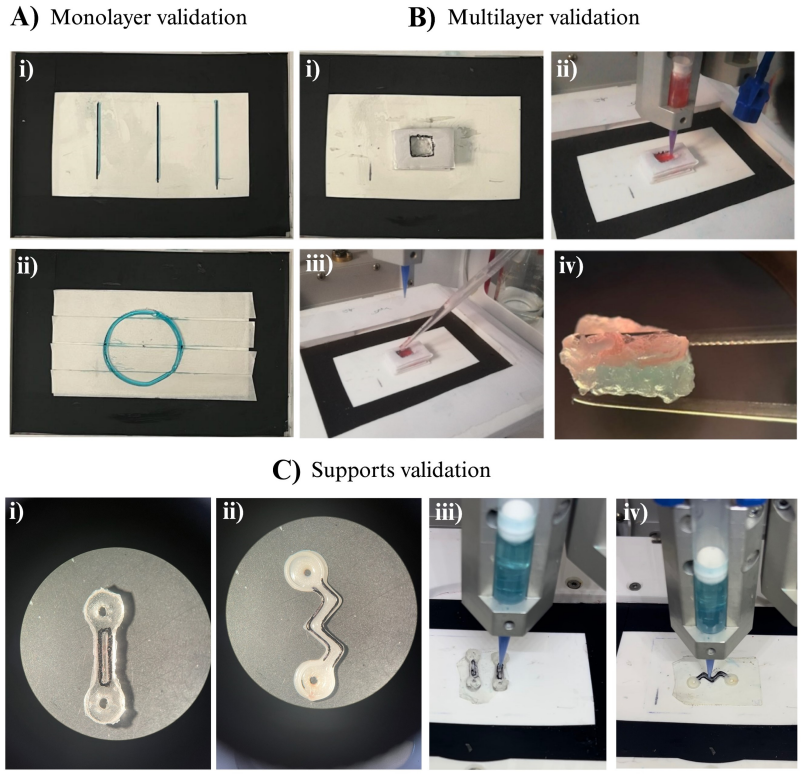

Figure A.7: Software validation. A) Monolayer. i) Three separate straight lines, ii) circle. B) Multilayer. i) Printing plate with the support. ii) Printing within the support. iii) Crosslinking with the calcium chloride. iv) Printing result. C) Supports. i) PDMS linear support and ii) PCL serpentine-like support with highlighted channel edges. iii) Printing within the linear channel, iv) Printing within the serpentine-like channel.

Bibliography

[1] Louise A Moyle, Erik Jacques, and Penney M Gilbert. "Engineering the next generation of human skeletal muscle models: from cellular complexity to disease modeling". In: *Current Opinion in Biomedical Engineering* 16 (2020), pp. 9–18.

[2] Tyler Potyondy et al. "Recent advances in 3D bioprinting of musculoskeletal tissues". In: *Biofabrication* 13.2 (2021), p. 022001.

[3] Claudia Mueller et al. "Effects of external stimulators on engineered skeletal muscle tissue maturation". In: *Advanced Materials Interfaces* 8.1 (2021), p. 2001167.

[4] Yaqi Wang et al. "Multiple effects of mechanical stretch on myogenic progenitor cells". In: *Stem Cells and Development* 29.6 (2020), pp. 336–352.

[5] Flavio L Ronzoni et al. "Myoblast 3D bioprinting to burst in vitro skeletal muscle differentiation". In: *Journal of Tissue Engineering and Regenerative Medicine* 16.5 (2022), pp. 484–495.

[6] Giada Loi et al. "3D Co-Printing and Substrate Geometry Influence the Differen-Tiation of C2C12 Skeletal Myoblasts". In: (2023).

[7] Pei Zhuang et al. "Bioprinting of 3D in vitro skeletal muscle models: A review". In: *Materials & Design* 193 (2020), p. 108794.

[8] Jürgen Groll et al. "Biofabrication: reappraising the definition of an evolving field". In: *Biofabrication* 8.1 (2016), p. 013001.

[9] Jos Malda et al. "25th anniversary article: engineering hydrogels for biofabrication". In: *Advanced materials* 25.36 (2013), pp. 5011–5028.

[10] Monika Hospodiuk et al. "The bioink: A comprehensive review on bioprintable materials". In: *Biotechnology advances* 35.2 (2017), pp. 217–239.

[11] Kaivalya A Deo et al. “Bioprinting 101: design, fabrication, and evaluation of cell-laden 3D bioprinted scaffolds”. In: *Tissue Engineering Part A* 26.5-6 (2020), pp. 318–338.

[12] Enrique Mancha Sánchez et al. “Hydrogels for bioprinting: A systematic review of hydrogels synthesis, bioprinting parameters, and bioprinted structures behavior”. In: *Frontiers in Bioengineering and Biotechnology* 8 (2020), p. 776.

[13] Amer B Dababneh and Ibrahim T Ozbolat. “Bioprinting technology: a current state-of-the-art review”. In: *Journal of Manufacturing Science and Engineering* 136.6 (2014), p. 061016.

[14] Lorenzo Moroni et al. “Biofabrication strategies for 3D in vitro models and regenerative medicine”. In: *Nature Reviews Materials* 3.5 (2018), pp. 21–37.

[15] Mohammadmahdi Mobaraki et al. “Bioinks and bioprinting: A focused review”. In: *Bioprinting* 18 (2020), e00080.

[16] Sean V Murphy and Anthony Atala. “3D bioprinting of tissues and organs”. In: *Nature biotechnology* 32.8 (2014), pp. 773–785.

[17] Ibrahim T Ozbolat and Monika Hospodiuk. “Current advances and future perspectives in extrusion-based bioprinting”. In: *Biomaterials* 76 (2016), pp. 321–343.

[18] N Peelman et al. “Manufacturing of advanced biodegradable polymeric components”. In: *J. Appl. Polym. Sci.* 132.48 (2015), p. 42305.

[19] Robert Chang, JAE Nam, and WEI Sun. “Effects of dispensing pressure and nozzle diameter on cell survival from solid freeform fabrication–based direct cell writing”. In: *Tissue Engineering Part A* 14.1 (2008), pp. 41–48.

[20] Amedeo Franco Bonatti et al. “Bioprinting technologies: An overview”. In: *Bioprinting* (2022), pp. 19–49.

[21] Rachel Elizabeth Saunders and Brian Derby. “Inkjet printing biomaterials for tissue engineering: bioprinting”. In: *International Materials Reviews* 59.8 (2014), pp. 430–448.

[22] Madhusudan Singh et al. “Inkjet printing-process and its applications”. In: *Advanced materials* 22.6 (2010), pp. 673–685.

[23] Ahu Arslan-Yildiz et al. “Towards artificial tissue models: past, present, and future of 3D bioprinting”. In: *Biofabrication* 8.1 (2016), p. 014103.

[24] Gabriele Maria Fortunato et al. “An ink-jet printed electrical stimulation platform for muscle tissue regeneration”. In: *Bioprinting* 11 (2018), e00035.

[25] Katja Holzl et al. “Bioink properties before, during and after 3D bioprinting”. In: *Biofabrication* 8.3 (2016), p. 032002.

[26] Ibrahim T Ozbolat, Kazim K Moncal, and Hemanth Gudapati. “Evaluation of bioprinter technologies”. In: *Additive Manufacturing* 13 (2017), pp. 179–200.

[27] Thomas Boland et al. “Drop-on-demand printing of cells and materials for designer tissue constructs”. In: *Materials Science and Engineering: C* 27.3 (2007), pp. 372–376.

[28] Xiaofeng Cui and Thomas Boland. “Human microvasculature fabrication using thermal inkjet printing technology”. In: *Biomaterials* 30.31 (2009), pp. 6221–6227.

[29] Tao Xu et al. “Viability and electrophysiology of neural cell structures generated by the inkjet printing method”. In: *Biomaterials* 27.19 (2006), pp. 3580–3588.

[30] Xiaofeng Cui et al. “Cell damage evaluation of thermal inkjet printed Chinese hamster ovary cells”. In: *Biotechnology and bioengineering* 106.6 (2010), pp. 963–969.

[31] Rachel E Saunders, Julie E Gough, and Brian Derby. “Delivery of human fibroblast cells by piezoelectric drop-on-demand inkjet printing”. In: *Biomaterials* 29.2 (2008), pp. 193–203.

[32] Hemanth Gudapati, Madhuri Dey, and Ibrahim Ozbolat. “A comprehensive review on droplet-based bioprinting: Past, present and future”. In: *Biomaterials* 102 (2016), pp. 20–42.

[33] Kalyani Nair et al. “Characterization of cell viability during bioprinting processes”. In: *Biotechnology Journal: Healthcare Nutrition Technology* 4.8 (2009), pp. 1168–1177.

[34] Andreas Blaeser et al. “Controlling shear stress in 3D bioprinting is a key factor to balance printing resolution and stem cell integrity”. In: *Advanced healthcare materials* 5.3 (2016), pp. 326–333.

[35] Helena N Chia and Benjamin M Wu. “Recent advances in 3D printing of biomaterials”. In: *Journal of biological engineering* 9 (2015), pp. 1–14.

[36] Abdul W Basit, Simon Gaisford, et al. *3D printing of pharmaceuticals*. Springer, 2018.

[37] Abiy Wubneh et al. “Current state of fabrication technologies and materials for bone tissue engineering”. In: *Acta Biomaterialia* 80 (2018), pp. 1–30.

[38] Francis LC Morgan, Lorenzo Moroni, and Matthew B Baker. “Dynamic bioinks to advance bioprinting”. In: *Advanced healthcare materials* 9.15 (2020), p. 1901798.

[39] Cristian Felipe-Mendes, Leire Ruiz-Rubio, and José Luis Vilas-Vilela. “Biomaterials obtained by photopolymerization: From UV to two photon”. In: *Emergent Materials* 3.4 (2020), pp. 453–468.

[40] Philippe Delaporte and Anne-Patricia Alloncle. “Laser-induced forward transfer: A high resolution additive manufacturing technology”. In: *Optics & Laser Technology* 78 (2016), pp. 33–41.

[41] J Marcos Fernández-Pradas and Pere Serra. “Laser-induced forward transfer: a method for printing functional inks”. In: *Crystals* 10.8 (2020), p. 651.

[42] Amir K Miri et al. “Effective bioprinting resolution in tissue model fabrication”. In: *Lab on a Chip* 19.11 (2019).

[43] Bertrand Guillotin et al. “Laser assisted bioprinting of engineered tissue with high cell density and microscale organization”. In: *Biomaterials* 31.28 (2010), pp. 7250–7256.

[44] AP Sughanthy Siva et al. “Three-Dimensional (3D) printing and bioprinting for orthopaedic biomaterials-A short review”. In: *IOP Conference Series: Materials Science and Engineering*. Vol. 1128. 1. IOP Publishing. 2021, p. 012028.

[45] Xiaohong Wang et al. “Generation of three-dimensional hepatocyte/gelatin structures with rapid prototyping system”. In: *Tissue engineering* 12.1 (2006), pp. 83–90.

[46] Dongjin Yoo. “New paradigms in internal architecture design and freeform fabrication of tissue engineering porous scaffolds”. In: *Medical engineering & physics* 34.6 (2012), pp. 762–776.

[47] Michael J. Sawkins et al. “3D cell and scaffold patterning strategies in tissue engineering”. In: *Recent Patents on Biomedical Engineering* 6.1 (2013), pp. 3–21.

[48] Roel Kuijer et al. “Assessing infection risk in implanted tissue-engineered devices”. In: *Biomaterials* 28.34 (2007), pp. 5148–5154.

[49] Satnam Singh et al. “In situ bioprinting–bioprinting from benchside to bedside?” In: *Acta biomaterialia* 101 (2020), pp. 14–25.

[50] Ibrahim T Ozbolat and Yin Yu. "Bioprinting toward organ fabrication: challenges and future trends". In: *IEEE Transactions on Biomedical Engineering* 60.3 (2013), pp. 691–699.

[51] Manyi Wang et al. "The trend towards in vivo bioprinting". In: *International Journal of Bioprinting* 1.1 (2015).

[52] John J O'Neill et al. "3D bioprinting directly onto moving human anatomy". In: *2017 IEEE/RSJ International Conference on Intelligent Robots and Systems (IROS)*. IEEE. 2017, pp. 934–940.

[53] Yang Wu, Dino J Ravnic, and Ibrahim T Ozbolat. "Intraoperative bioprinting: repairing tissues and organs in a surgical setting". In: *Trends in biotechnology* 38.6 (2020), pp. 594–605.

[54] Mohammed Albanna et al. "In situ bioprinting of autologous skin cells accelerates wound healing of extensive excisional full-thickness wounds". In: *Scientific reports* 9.1 (2019), p. 1856.

[55] Xiao Li et al. "Development of a robotic arm based hydrogel additive manufacturing system for in-situ printing". In: *Applied Sciences* 7.1 (2017), p. 73.

[56] Kaiwei Ma et al. "Application of robotic-assisted in situ 3D printing in cartilage regeneration with HAMA hydrogel: An in vivo study". In: *Journal of advanced research* 23 (2020), pp. 123–132.

[57] Navid Hakimi et al. "Handheld skin printer: in situ formation of planar biomaterials and tissues". In: *Lab on a Chip* 18.10 (2018), pp. 1440–1451.

[58] Virginie Keriquel et al. "In vivo bioprinting for computer-and robotic-assisted medical intervention: preliminary study in mice". In: *Biofabrication* 2.1 (2010), p. 014101.

[59] Cathal D O'Connell et al. "Development of the Biopen: a handheld device for surgical printing of adipose stem cells at a chondral wound site". In: *Biofabrication* 8.1 (2016), p. 015019.

[60] Claudia Di Bella et al. "In situ handheld three-dimensional bioprinting for cartilage regeneration". In: *Journal of tissue engineering and regenerative medicine* 12.3 (2018), pp. 611–621.

[61] Ming Zhao et al. "Functionalizing multi-component bioink with platelet-rich plasma for customized in-situ bilayer bioprinting for wound healing". In: *Materials Today Bio* 16 (2022), p. 100334.

[62] Joseph P Vacanti and Robert Langer. "Tissue engineering: the design and fabrication of living replacement devices for surgical reconstruction and transplantation". In: *The lancet* 354 (1999), S32–S34.

[63] Michael D Buschmann et al. "Mechanical compression modulates matrix biosynthesis in chondrocyte/agarose culture". In: *Journal of cell science* 108.4 (1995), pp. 1497–1508.

[64] Douglas E Coplen et al. "Cultured bladder cells and their response to mechanical strain". In: *Muscle, Matrix, and Bladder Function* (1995), pp. 207–214.

[65] Harald C Ott et al. "Perfusion-decellularized matrix: using nature's platform to engineer a bioartificial heart". In: *Nature medicine* 14.2 (2008), pp. 213–221.

[66] Milica Radisic et al. "Optical mapping of impulse propagation in engineered cardiac tissue". In: *Tissue Engineering Part A* 15.4 (2009), pp. 851–860.

[67] Giulia M Di Gravina et al. "Computer-aided engineering and additive manufacturing for bioreactors in tissue engineering: State of the art and perspectives". In: *Biophysics Reviews* 4.3 (2023).

[68] Stefano Gabetti et al. "An automated 3D-printed perfusion bioreactor combinable with pulsed electromagnetic field stimulators for bone tissue investigations". In: *Scientific Reports* 12.1 (2022), p. 13859.

[69] Wonjae Lee et al. "3D-printed microfluidic device for the detection of pathogenic bacteria using size-based separation in helical channel with trapezoid cross-section". In: *Scientific reports* 5.1 (2015), p. 7717.

[70] G Talò et al. "Industrialization of a perfusion bioreactor: Prime example of a non-straightforward process". In: *Journal of Tissue Engineering and Regenerative Medicine* 12.2 (2018), pp. 405–415.

[71] Martina Sladkova and Giuseppe Maria De Peppo. "Bioreactor systems for human bone tissue engineering". In: *Processes* 2.2 (2014), pp. 494–525.

[72] Dylan Jack Richards et al. "3D printing for tissue engineering". In: *Israel Journal of Chemistry* 53.9-10 (2013), pp. 805–814.

[73] Adam J Janvier, Elizabeth Canty-Laird, and James R Henstock. "A universal multi-platform 3D printed bioreactor chamber for tendon tissue engineering". In: *Journal of Tissue Engineering* 11 (2020), p. 2041731420942462.

[74] Brittany L Banik and Justin L Brown. “3D-printed bioreactor enhances potential for tendon tissue engineering”. In: *Regenerative Engineering and Translational Medicine* 6 (2020), pp. 419–428.

[75] Kathryn W Aguilar-Agon et al. “Mechanical loading stimulates hypertrophy in tissue-engineered skeletal muscle: Molecular and phenotypic responses”. In: *Journal of Cellular Physiology* 234.12 (2019), pp. 23547–23558.

[76] Philipp Heher et al. “A novel bioreactor for the generation of highly aligned 3D skeletal muscle-like constructs through orientation of fibrin via application of static strain”. In: *Acta biomaterialia* 24 (2015), pp. 251–265.

[77] Herman H Vandenburgh, Somporn Swasdison, and Patricia Karlisch. “Computer-aided mechanogenesis of skeletal muscle organs from single cells in vitro”. In: *The FASEB journal* 5.13 (1991), pp. 2860–2867.

[78] Gabriele Candiani et al. “Cyclic mechanical stimulation favors myosin heavy chain accumulation in engineered skeletal muscle constructs”. In: *Journal of Applied Biomaterials and Biomechanics* 8.2 (2010), pp. 68–75.

[79] S Mantero et al. “A new electro-mechanical bioreactor for soft tissue engineering”. In: *Journal of Applied Biomaterials and Biomechanics* 5.2 (2007), pp. 107–116.

[80] Du Geon Moon et al. “Cyclic mechanical preconditioning improves engineered muscle contraction”. In: *Tissue Engineering Part A* 14.4 (2008), pp. 473–482.

[81] Keiji Seki et al. “Aligning collagen fibers by cyclic mechanical stretch for efficiently muscle cell actuator”. In: *2016 IEEE International Conference on Robotics and Biomimetics (ROBIO)*. IEEE. 2016, pp. 1197–1202.

[82] Courtney A Powell et al. “Mechanical stimulation improves tissue-engineered human skeletal muscle”. In: *American Journal of Physiology-Cell Physiology* 283.5 (2002), pp. C1557–C1565.

[83] Zongzhe Xuan et al. “Stable hydrogel adhesion to polydimethylsiloxane enables cyclic mechanical stimulation of 3D-bioprinted smooth muscle constructs”. In: *Biotechnology and Bioengineering* 120.11 (2023), pp. 3396–3408.

[84] Jean-Louis Milan, Josep A Planell, and Damien Lacroix. "Simulation of bone tissue formation within a porous scaffold under dynamic compression". In: *Biomechanics and modeling in mechanobiology* 9 (2010), pp. 583–596.

[85] Damien P Byrne et al. "Simulation of tissue differentiation in a scaffold as a function of porosity, Young's modulus and dissolution rate: application of mechanobiological models in tissue engineering". In: *Biomaterials* 28.36 (2007), pp. 5544–5554.

[86] Joao S Soares and Michael S Sacks. "A triphasic constrained mixture model of engineered tissue formation under in vitro dynamic mechanical conditioning". In: *Biomechanics and modeling in mechanobiology* 15 (2016), pp. 293–316.

[87] Andrea Pavesi et al. "Controlled electromechanical cell stimulation on-a-chip". In: *Scientific Reports* 5.1 (2015), p. 11800.

[88] Yingning He et al. "A simplified yet enhanced and versatile microfluidic platform for cyclic cell stretching on an elastic polymer". In: *Biofabrication* 12.4 (2020), p. 045032.

[89] Charis Czichy et al. "CyMAD bioreactor: A cyclic magnetic actuation device for magnetically mediated mechanical stimulation of 3D bioprinted hydrogel scaffolds". In: *Journal of the mechanical behavior of biomedical materials* 131 (2022), p. 105253.

[90] Valerio Luca Mainardi et al. "Culture of 3D bioprinted bone constructs requires an increased fluid dynamic stimulation". In: *Acta Biomaterialia* 153 (2022), pp. 374–385.

[91] Yeong-Jin Choi et al. "3D cell printing of functional skeletal muscle constructs using skeletal muscle-derived bioink". In: *Advanced healthcare materials* 5.20 (2016), pp. 2636–2645.

[92] Hyun-Wook Kang et al. "A 3D bioprinting system to produce human-scale tissue constructs with structural integrity". In: *Nature biotechnology* 34.3 (2016), pp. 312–319.

[93] Ji Hyun Kim et al. "3D bioprinted human skeletal muscle constructs for muscle function restoration". In: *Scientific reports* 8.1 (2018), p. 12307.

[94] Nathan D Bade et al. "Curvature and Rho activation differentially control the alignment of cells and stress fibers". In: *Science advances* 3.9 (2017), e1700150.

[95] Monika Rumpler et al. “The effect of geometry on three-dimensional tissue growth”. In: *Journal of the Royal Society Interface* 5.27 (2008), pp. 1173–1180.

[96] Cécile M Bidan et al. “How linear tension converts to curvature: geometric control of bone tissue growth”. In: *PloS one* 7.5 (2012), e36336.

[97] Cécile M Bidan et al. “Geometry as a factor for tissue growth: towards shape optimization of tissue engineering scaffolds”. In: *Advanced healthcare materials* 2.1 (2013), pp. 186–194.

[98] J Knychala et al. “Pore geometry regulates early stage human bone marrow cell tissue formation and organisation”. In: *Annals of biomedical engineering* 41 (2013), pp. 917–930.

[99] Yann Guyot et al. “A computational model for cell/ECM growth on 3D surfaces using the level set method: a bone tissue engineering case study”. In: *Biomechanics and modeling in mechanobiology* 13 (2014), pp. 1361–1371.

[100] Yann Guyot et al. “Coupling curvature-dependent and shear stress-stimulated neotissue growth in dynamic bioreactor cultures: a 3D computational model of a complete scaffold”. In: *Biomechanics and modeling in mechanobiology* 15 (2016), pp. 169–180.

[101] Maike Werner et al. “Mesoscale substrate curvature overrules nanoscale contact guidance to direct bone marrow stromal cell migration”. In: *Journal of The Royal Society Interface* 15.145 (2018), p. 20180162.

[102] Sebastien JP Callens et al. “Substrate curvature as a cue to guide spatiotemporal cell and tissue organization”. In: *Biomaterials* 232 (2020), p. 119739.

[103] Yen-Chih Huang et al. “Rapid formation of functional muscle in vitro using fibrin gels”. In: *Journal of applied physiology* 98.2 (2005), pp. 706–713.

[104] Sebastien JP Callens et al. “Emergent collective organization of bone cells in complex curvature fields”. In: *Nature Communications* 14.1 (2023), p. 855.

[105] Zohreh Izadifar et al. “Analyzing biological performance of 3D-printed, cell-impregnated hybrid constructs for cartilage tissue engineering”. In: *Tissue Engineering Part C: Methods* 22.3 (2016), pp. 173–188.

[106] Adam W Feinberg et al. “Muscular thin films for building actuators and powering devices”. In: *Science* 317.5843 (2007), pp. 1366–1370.

[107] Yo Tanaka et al. “An actuated pump on-chip powered by cultured cardiomyocytes”. In: *Lab on a Chip* 6.3 (2006), pp. 362–368.

[108] Yo Tanaka et al. “Demonstration of a PDMS-based bio-microactuator using cultured cardiomyocytes to drive polymer micropillars”. In: *Lab on a Chip* 6.2 (2006), pp. 230–235.

[109] Yoshitake Akiyama, Yuji Furukawa, and Keisuke Morishima. “Controllable bio-microactuator powered by muscle cells”. In: *2006 International Conference of the IEEE Engineering in Medicine and Biology Society*. IEEE. 2006, pp. 6565–6568.

[110] Hugh Herr and Robert G Dennis. “A swimming robot actuated by living muscle tissue”. In: *Journal of neuroengineering and rehabilitation* 1 (2004), pp. 1–9.

[111] Giada Loi et al. “Design, development, and benchmarking of a bioreactor integrated with 3D bioprinting: Application to skeletal muscle regeneration”. In: *Bioprinting* 42 (2024), e00352.

[112] Flaminio CP Sales et al. “Mechanical characterization of PDMS with different mixing ratios”. In: *Procedia Structural Integrity* 37 (2022), pp. 383–388.

[113] Li Rao, Yuqin Liu, and Haihan Zhou. “Significantly improved cell affinity of polydimethylsiloxane enabled by a surface-modified strategy with chemical coupling”. In: *Journal of Materials Science: Materials in Medicine* 33.10 (2022), p. 66.

[114] Chaenyung Cha et al. “Tailoring hydrogel adhesion to polydimethylsiloxane substrates using polysaccharide glue”. In: *Angewandte Chemie International Edition* 52.27 (2013), pp. 6949–6952.

[115] Fahima Akther et al. “Surface modification techniques for endothelial cell seeding in PDMS microfluidic devices”. In: *Biosensors* 10.11 (2020), p. 182.

[116] Forough Ataollahi et al. “Endothelial cell responses in terms of adhesion, proliferation, and morphology to stiffness of polydimethylsiloxane elastomer substrates”. In: *Journal of biomedical materials research Part A* 103.7 (2015), pp. 2203–2213.

[117] Andrews Souza et al. “Characterization of shear strain on PDMS: Numerical and experimental approaches”. In: *Applied Sciences* 10.9 (2020), p. 3322.

[118] Sara Ragazzini et al. “Mechanosensor YAP cooperates with TGF-β1 signaling to promote myofibroblast activation and matrix stiffening in a 3D model of human cardiac fibrosis”. In: *Acta Biomaterialia* 152 (2022), pp. 300–312.

[119] Gayathri Subramanian et al. “Creating homogenous strain distribution within 3D cell-encapsulated constructs using a simple and cost-effective uniaxial tensile bioreactor: Design and validation study”. In: *Biotechnology and Bioengineering* 114.8 (2017), pp. 1878–1887.

[120] Anthony Ratcliffe and Laura E Niklason. “Bioreactors and bioprocessing for tissue engineering”. In: *Annals of the New York Academy of Sciences* 961.1 (2002), pp. 210–215.

[121] Gail K Naughton. “From lab bench to market: critical issues in tissue engineering”. In: *Annals of the New York Academy of Sciences* 961.1 (2002), pp. 372–385.

[122] Kamal Izdihar et al. “Structural, mechanical, and dielectric properties of polydimethylsiloxane and silicone elastomer for the fabrication of clinical-grade kidney phantom”. In: *Applied Sciences* 11.3 (2021), p. 1172.

[123] Angelina Müller, Matthias C Wapler, and Ulrike Wallrabe. “A quick and accurate method to determine the Poisson’s ratio and the coefficient of thermal expansion of PDMS”. In: *Soft Matter* 15.4 (2019), pp. 779–784.

[124] Zhehao Wang et al. “Influence of laser energy density and printing angle on the electrical properties of PA12 made by SLS”. In: *IEEE Transactions on Dielectrics and Electrical Insulation* 28.3 (2021), pp. 906–914.

[125] Nicolas Lammens, Ives De Baere, and Wim Van Paepegem. “On the orthotropic elasto-plastic material response of additively manufactured polyamide 12”. In: *7th bi-annual international conference of Polymers & moulds innovations (PMI 2016)*. 2016.

[126] Tiago Czelusniak and Fred Lacerda Amorim. “Influence of energy density on polyamide 12 processed by SLS: from physical and mechanical properties to microstructural and crystallization evolution”. In: *Rapid Prototyping Journal* 27.6 (2021), pp. 1189–1205.

[127] Lirong Meng, Jiang He, and Caofeng Pan. “Research Progress on Hydrogel–Elastomer Adhesion”. In: *Materials* 15.7 (2022), p. 2548.

[128] Hongbin Zhang et al. “Fabrication of robust hydrogel coatings on polydimethylsiloxane substrates using micropillar anchor structures with chemical surface modification”. In: *ACS applied materials & interfaces* 6.12 (2014), pp. 9126–9133.

[129] Kevin Tian et al. “Adhesion between hydrophobic elastomer and hydrogel through hydrophilic modification and interfacial segregation”. In: *ACS applied materials & interfaces* 10.49 (2018), pp. 43252–43261.

[130] Giada Loi et al. “Characterization of a bioink combining extracellular matrix-like hydrogel with osteosarcoma cells: preliminary results”. In: *Gels* 9.2 (2023), p. 129.

[131] Kuen Yong Lee and David J Mooney. “Alginate: properties and biomedical applications”. In: *Progress in polymer science* 37.1 (2012), pp. 106–126.

[132] Valentina Fantini et al. “Bioink composition and printing parameters for 3D modeling neural tissue”. In: *Cells* 8.8 (2019), p. 830.

[133] Elia Bari et al. “Silk Fibroin Bioink for 3D Printing in Tissue Regeneration: Controlled Release of MSC extracellular Vesicles”. In: *Pharmaceutics* 15.2 (2023), p. 383.

[134] Jordan M Cloyd et al. “Material properties in unconfined compression of human nucleus pulposus, injectable hyaluronic acid-based hydrogels and tissue engineering scaffolds”. In: *European spine journal* 16 (2007), pp. 1892–1898.

[135] Rie Kjær Christensen et al. “3D printed hydrogel multiassay platforms for robust generation of engineered contractile tissues”. In: *Biomacromolecules* 21.2 (2019), pp. 356–365.

[136] Daniel AW Oortgiesen et al. “A three-dimensional cell culture model to study the mechano-biological behavior in periodontal ligament regeneration”. In: *Tissue Engineering Part C: Methods* 18.2 (2012), pp. 81–89.

[137] Marius Gensler et al. “3D printing of bioreactors in tissue engineering: A generalised approach”. In: *PLoS One* 15.11 (2020), e0242615.

[138] Sari Katz et al. “Studying the physical and chemical properties of polydimethylsiloxane matrix reinforced by nanostructured TiO2 supported on mesoporous silica”. In: *Polymers* 15.1 (2022), p. 81.

[139] Jirasuta Chungprempree, Jitima Preechawong, and Manit Nithitanakul. "Developing an effective and durable film for marine fouling prevention from PDMS/SiO2 and PDMS/PU with SiO2 composites". In: *Polymers* 14.20 (2022), p. 4252.

[140] Flaminio Sales et al. "Composite material of PDMS with interchangeable transmittance: Study of optical, mechanical properties and wettability". In: *Journal of Composites Science* 5.4 (2021), p. 110.

[141] Zhenhua Tang et al. "Graphene-based polymer bilayers with superior light-driven properties for remote construction of 3D structures". In: *Advanced Science* 4.5 (2017), p. 1600437.

[142] Ian D Johnston et al. "Mechanical characterization of bulk Sylgard 184 for microfluidics and microengineering". In: *Journal of Micromechanics and Microengineering* 24.3 (2014), p. 035017.

[143] Onobu Akogwu et al. "Large strain deformation and cracking of nanoscale gold films on PDMS substrate". In: *Materials Science and Engineering: B* 170.1-3 (2010), pp. 32–40.

[144] SM Giannitelli et al. "Combined additive manufacturing approaches in tissue engineering". In: *Acta biomaterialia* 24 (2015), pp. 1–11.

[145] Michele Conti and Michele Marino. *Bioprinting: From Multidisciplinary Design to Emerging Opportunities*. Academic Press, 2022.

[146] Andrea Schwab et al. "Printability and shape fidelity of bioinks in 3D bioprinting". In: *Chemical reviews* 120.19 (2020), pp. 11028–11055.

[147] Naomi Paxton et al. "Proposal to assess printability of bioinks for extrusion-based bioprinting and evaluation of rheological properties governing bioprintability". In: *Biofabrication* 9.4 (2017), p. 044107.

[148] Dario Carbonaro et al. "A low-cost scalable 3D-printed sample-holder for agitation-based decellularization of biological tissues". In: *Medical Engineering & Physics* 85 (2020), pp. 7–15.

[149] Carlos Ezio Garciamendez-Mijares et al. "Development of an affordable extrusion 3D bioprinter equipped with a temperature-controlled printhead". In: *Int J Bioprint* (2023).

[150] Eva Mueller et al. "Coaxial extrusion bioprinting of hydrazone crosslinked POEGMA hydrogels: Optimizing needle geometry to achieve improved print quality". In: *Bioprinting* 35 (2023), e00307.

[151] Franca Scocozza et al. “Prediction of the mechanical response of a 3D (bio) printed hybrid scaffold for improving bone tissue regeneration by structural finite element analysis”. In: *Journal of the Mechanical Behavior of Biomedical Materials* 142 (2023), p. 105822.

[152] Aidin Hajikhani et al. “Experimental characterization and computational modeling of hydrogel cross-linking for bioprinting applications”. In: *The International journal of artificial organs* 42.10 (2019), pp. 548–557.

[153] Gokhan Bahcecioglu et al. “Breast cancer models: Engineering the tumor microenvironment”. In: *Acta biomaterialia* 106 (2020), pp. 1–21.

[154] Xinxiu Wu et al. “Heat-triggered poly (siloxane-urethane) s based on disulfide bonds for self-healing application”. In: *Journal of Applied Polymer Science* 135.31 (2018), p. 46532.

[155] Amanda Zimmerling et al. “3D printing PCL/nHA bone scaffolds: Exploring the influence of material synthesis techniques”. In: *Biomaterials Research* 25.1 (2021), pp. 1–12.

[156] Giulia M Di Gravina et al. “Design and development of a hepatic lyodECM powder as a biomimetic component for 3D-printable hybrid hydrogels”. In: *Biomedical Materials* (2023).

[157] Shinako Bansai et al. “Effect of cyclic stretch on tissue maturation in myoblast-laden hydrogel fibers”. In: *Micromachines* 10.6 (2019), p. 399.

[158] Piyush Bajaj et al. “Patterning the differentiation of C2C12 skeletal myoblasts”. In: *Integrative Biology* 3.9 (2011), pp. 897–909.

[159] Ivan Martin, David Wendt, and Michael Heberer. “The role of bioreactors in tissue engineering”. In: *TRENDS in Biotechnology* 22.2 (2004), pp. 80–86.

[160] Lorenzo Fassina et al. “Effects of electromagnetic stimulation on calcified matrix production by SAOS-2 cells over a polyurethane porous scaffold”. In: *Tissue engineering* 12.7 (2006), pp. 1985–1999.

Pubblications

Articles in peer-reviewed journals

Giada **Loi**, Franca Scocozza, Laura Benedetti, Ferdinando Auricchio, Stefania Marconi, Elena Delgrosso, Gabriella Cusella, Gabriele Ceccarelli, Michele Conti. Design, development, and benchmarking of a bioreactor integrated with 3D bioprinting: Application to skeletal muscle regeneration. *Bioprinting*, 2024).

Giulia Maria Di Gravina, **Giada Loi**, Ferdinando Auricchio, Michele Conti. Computer-aided engineering and additive manufacturing for bioreactors in tissue engineering: State of the art and perspectives. *Biophysics Reviews*, 2023.

Giada Loi, Franca Scocozza, Flaminia Aliberti, Lorenza Rinvenuto, Gianluca Cidonio, Nicola Marchesi, Laura Benedetti, Gabriele Ceccarelli, Michele Conti. 3D Co-Printing and Substrate Geometry Influence the Differentiation of C2C12 Skeletal Myoblasts. *Gels*, 2023.

Elena Delgrosso, Franca Scocozza, Laura Cansolino, Federica Riva, Michele Conti, **Giada Loi**, Ferdinando Auricchio, Ian Postuma, Silva Bortolussi, Lorenzo Cobianchi, Cinzia Ferrari. 3D bioprinted osteosarcoma model for experimental boron neutron capture therapy (BNCT) applications: Preliminary assessment. *Journal of Biomedical Materials Research Part B: Applied Biomaterials*,2023.

Giada Loi, Gaia Stucchi, Franca Scocozza, Laura Cansolino, Francesca Cadamuro, Elena Delgrosso, Federica Riva, Cinzia Ferrari, Laura Russo, Michele Conti. Characterization of a bioink combining extracellular matrix-like hydrogel with osteosarcoma cells: preliminary results. *Gels*,129, 2023.

Francesca Usai, **Giada Loi**, Franca Scocozza, Massimo Bellato, Ignazio Castagli-

uolo, Michele Conti, Lorenzo Pasotti. Design and biofabrication of bacterial living materials with robust and multiplexed biosensing capabilities. *Materials Today Bio*, 100526, 2022.

Published abstracts

Flaminia Aliberti, Lorenza Rinvenuto, **Giada Loi**, Laura Benedetti, Franca Scocozza, Flavio L. Ronzoni, Maurilio Sanpaolesi, Gabriella Cusella, and Gabriele Ceccarelli. Comparative analysis of different hydrogels for the bioprinting of 3D in vitro skeletal muscle models. *Biomedical Science and Engineering*,4(s1):146, 2021.

Book chapters

Michele Conti, **Giada Loi**, Stefania Marconi, Franca Scocozza. *Material testing and mechanical modeling in bioprinting. Biofabrication: an integrated bioengineering approach for the automated fabrication of biological structures for clinical and research applications*, Patron editore, 95-116, 2021.

Awards

2st place during GNB school competition at XLI Annual GNB School 2021 "Biomedical Engineering for Sustainable Development".

Acknowledgements